Technische Universität München
Institut für Energietechnik

Lehrstuhl für Thermodynamik

Thermoacoustic Stability Analysis from Open Loop Transfer Functions based on LES

Dipl.-Ing. Univ. Roland Kaess

Vollständiger Abdruck der von der Fakultät für Maschinenwesen der Technischen Universität München zur Erlangung des akademischen Grades eines

DOKTOR – INGENIEURS

genehmigten Dissertation.

Vorsitzender:
Univ.-Prof. Dr.-Ing. habil. Boris Lohmann
Prüfer der Dissertation:
Univ.-Prof. Wolfgang H. Polifke, Ph. D.
Univ.-Prof. Dr.-Ing., Dr.-Ing. habil., Dr. h.c. Rudolf Schilling

Die Dissertation wurde am 15.04.2010 bei der Technischen Universität München eingereicht und durch die Fakultät für Maschinenwesen am 23.06.2010 angenommen.

Preface

The present thesis is the result of my work at the Lehrstuhl für Thermodynamik at the Technische Universität München from September 2005 until February 2009. During this period of time I was a guest at Cerfacs in Toulouse twice, once in 2006 for three months and once 2008 for two months.
In this context, I would like to thank Professor Wolfgang Polifke, Ph.D, for giving me the opportunity to work for him and for supervising this thesis. He always offered a helping hand when difficulties arose and discussions with him were always constructive and fruitful. It was also his idea to apply for the CTR Summer Program 2008, where parts of this work were done, and which was a great experience.
I also want to express my thanks to the team of Cerfacs, especially Thierry Poinsot and Bénédicte Cuenot, for giving me the chance to work at the institute and making me feel welcome. Each stay at Cerfacs was highly productive and provided my work with valuable input.
Numerous people have contributed to this thesis, some of whom deserve a special mention here. At the Lehrstuhl für Thermodynamik I would like to thank, in random order, Andreas Huber, Elke Wanke, Thomas Komarek, Jan Kopitz, Peter Bollweg and Stephan Föller. Among the people I met at Cerfacs I would like to mention Alexis Giauque, Guilhem Lacaze, Gabriel Staffelbach and Jens-Dominik Müller.
Many thanks also to Professor Dr.-Ing. habil. Lohmann for acting as chairman and Professor Dr.-Ing .habil., Dr. h.c. Schilling for acting as examiner.
Above all, I want to thank my family and friends for supporting me throughout the writing of this thesis.
Funding for this work was provided by the Deutsche Forschungsgemeinschaft, Marie Curie Actions and the Center for Turbulence Research and is gratefully acknowledged.

München, October 2010 Roland Kaess

Contents

Nomenclature

Small Latin Letters

a	arbitrary factors
b	arbitrary factors
c	sonic velocity [m/s]
$\vec{c}$	cross-correlation vector
$\vec{f}$	volume force vector[m/s^2]
f	frequency [1/s]
f	random function
$\mathfrak{f}$	characteristic wave [m/s]
g	random function
$\mathfrak{g}$	characteristic wave [m/s]
$\vec{h}$	unit impulse vector
k	wave number [1/m]
l	length [m]
l_{i}	Kolmogorov length [m]
p	pressure[kg /s^2/m^2]
$\vec{r}$	response vector
r_{i}	element of response vector
s	flame speed [m/s]
$\vec{s}$	signal vector
s_{i}	element of signal vector
t	time [s]
$\vec{u}$	velocity vector [m/s]
u_{i}	velocity in i-direction [m/s]
$x(s)$	Laplace transformed signal

$x(\omega)$	Fourier transformed signal
$y(s)$	Laplace transformed signal
$y(\omega)$	Fourier transformed signal
$\vec{x}$	coordinate vector [m]
x_i	coordinate in direction i [m]
$\vec{w}$	vector of the conservative variables [non uniform]
z	random complex number

Capital Latin Letters

C_ij	element of the cross stress tensor [kg/m/s^2]
D_ij	element of the deformation tensor
E	energy
$\mathscr{E}$	efficiency function
$F(s)$	Laplace transformed arbitrary function
$F(\omega)$	Fourier transformed arbitrary function
$G(s)$	Laplace transformed arbitrary function
$G(\omega)$	Fourier transformed arbitrary function
$\mathscr{L}$	characteristics [non uniform]
M_k	molar weight of species k [kg/kmol]
R_ij	element of the Reynolds stress tensor [kg/m/s^2]
S	Surface [m^2]
$\mathscr{S}_\mathrm{i}$	source term
$\vec{\mathscr{S}}$	vector of sources [non uniform]
S_ij	traceless symmetric part of the square of the velocity gradient tensor
$\mathfrak{S}_\mathrm{ij}$	element of the scattering matrix
T	Temperature [K]
T_ij	element of the Leonard stress tensor [kg/m/s^2]
$\vec{V}$	vector of mass linked volume forces [m/s^2]
$\mathfrak{T}_\mathrm{ij}$	element of the transfer matrix
V	volume [m^3]
X_k	molar fraction of species k
Y_k	mass fraction of species k

Greek Letters

α	interpolation factor
ν	kinematic viscosity [m^2/s]
η	dynamic viscosity [kg/m/s]
ϵ	viscous energy dissipation [m^2/s^3]
ρ	density [kg/m^3]
λ	wavelength [m]
λ	air-fuel ratio
ϕ	equivalence ratio
ρ	density [kg/m^3]
τ_{ij}	shear stress tensor [kg/m/s^2]
ω	angular frequency [1/s]
Ξ	wrinkling factor
Γ	auto-correlation matrix

Indices

0	reference value
el	element
cgr	center of gravity
tri	triangle
tot	total

Superscripts

$'$	acoustic perturbation
$\grave{}$	quantity not resolved by filter

$\tilde{}$	turbulent perturbation
^{0}	imposed
*	Eigenfrequency
$\bar{}$	mean value
$\hat{}$	in frequency domain

Abbreviations

CFD	Computational Fluid Dynamics
CNN	CFD-Network-Nyquist
DNS	Direct Numerical Simulation
FFT	Flame Transfer Function
FTF	Fast Fourier Transformation
LES	Large Eddy Simulation
NSCBC	Navier-Stokes Characteristic Boundary Condition
OLG	Open Loop Gain
OLTF	Open Loop Transfer Function
PLTF	Part Loop Transfer Function
RANS	Reynolds Averaged Navier Stokes

1 Introduction

Thermo-acoustic instabilities are of concern in a wide field of applications mostly linked to combustion. Striking examples can be found in rocket engines [9, 10]. The introduction of lean premix combustion systems in gas turbines has moved the topic into the focus of research again (e.g., [37]). Not only large scale systems but even small devices such as car heating units can be affected by this problem. Consequences of thermo-acoustic instabilities can vary from spurious noise emissions over violation of performance specifications and environmental requirements to structural failure of the device. Therefore, the prediction of thermo-acoustic instabilities in an early stage of the design process is essential. It can prevent the occurrence of such undesired effects and, by this, avoid expensive and time-consuming troubleshooting and redesign processes. Likely, with increasing demand for lean premix combustion systems also in more critical configurations (as might be the case for aircraft gas turbines in the future), more powerful methods for the prediction of thermo-acoustic instabilities are required and desired.

G. Moore predicted in 1965: "*The complexity for minimum component costs has increased at a rate of roughly a factor of two per year [...]. Certainly over the short term this rate can be expected to continue, if not to increase. Over the longer term, the rate of increase is a bit more uncertain, although there is no reason to believe it will not remain nearly constant for at least 10 years*". [58] This statement, known as Moore's law, has proved to be true for the last 40 years. Figure 1.1 illustrates this effect. This increasing power makes new methods for computational evaluation affordable. These also offer new possibilities for the prediction of such instabilities. In this context, Large Eddy Simulations (LES) have become a recent focus of research. LES still require huge cluster resources when the simulation is applied to real geometries. But within a few years, the increasing computational power will make LES

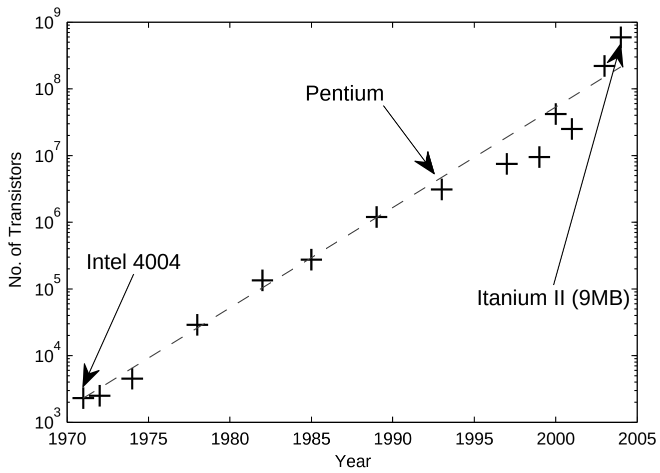

Figure 1.1: Visualisation of Moore's law with a selection of microprocessors. Data from www.intel.com, "Moore's Law 40th Anniversary" press kit.

common for engineering purposes.
The prediction of thermo-acoustic instabilities comprises a wide field of physical effects i.e. acoustics, turbulence, combustion and their mutual interactions. All these effects cover an extremely wide range of local and temporal scales. Figure 1.2 illustrates this. As a consequence, the simulation

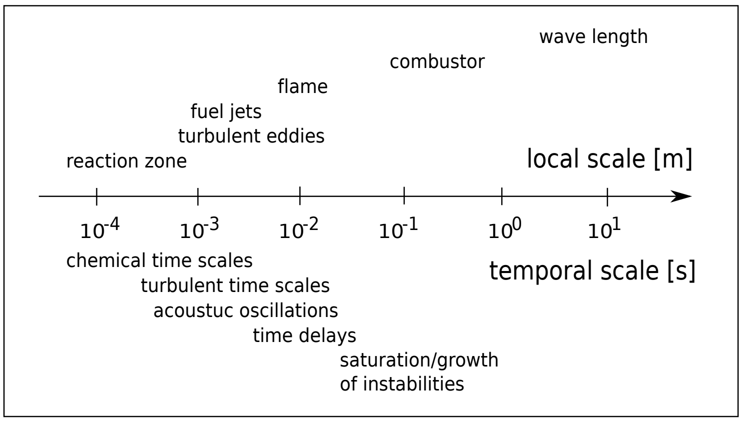

Figure 1.2: Visualisation of the different local and temporal scales involved in thermo-acoustic problems.

of a thermo-acoustic problem in one single simulation is computationally expensive, because the smallest scales of the most critical effect dictate the

resolution for all other scales and effects.
Concepts of “divide and conquer” have been widely used to keep the computational effort reasonable. They use simple, quick codes for the calculation of the acoustics and often combine these with parametric models for the dynamics of the flame. The complex interactions are strongly simplified here. LES is capable of simulating turbulence-acoustic interaction as well as more detailed combustion processes, which are both important for thermo-acoustic instabilities. Yet these interactions are usually localized and large parts of thermo-acoustic systems can still be described by simple methods such as 1D acoustic equations. Therefore, the application of LES is promising for those parts of the system that involve complex interactions. Additionally, it is still desirable to find a way to combine LES with more simple methods in order to gain speed and flexibility.
Polifke and Kopitz have developed such an approach, and some validation has been done on a Rijke tube and a duct system [46]. The present work can be seen in continuation of and addition to the thesis of Jan Kopitz [44].
Starting from Kopitz’ work, a more powerful interface between LES and the Network model is implemented and validated. This interface consists of a new, non-reflecting boundary condition for LES. Then, the approach is applied for the first time to a test case involving laminar combustion. A second test case involving turbulent combustion then demonstrates the limit of the approach. The thesis starts with a repetition of the basic physical and numerical concepts used and gives an overview over methods used in fluid mechanics and a more detailed insight into the theory of the prediction of thermo-acoustic instabilities. In the subsequent chapters, the tools which were implemented into the LES solver AVBP are presented. The two different cases, a laminar and a turbulent premix burner, are used to demonstrate the capabilities and the limits of the method. These limits are discussed and their theoretical background is examined.

2 Basic Equations

This chapter gives a brief overview over the basic concepts in fluid mechanics, involving acoustics and combustion. Numerical methods that are of importance for the simulation of acoustics and turbulent flow are presented. A short subsection treats system identification.

2.1 Basic Equations of Fluid Mechanics

In this thesis, different approaches for the description of fluid mechanics and acoustics are used. They range from computationally high demanding transient simulations to low order models in the frequency domain. All these models can be derived from the same set of equations, which are then simplified to different degrees. The most basic equations and their simplifications are presented in the following.
Historically, two conceptually different approaches have been developed for the description of fluid motion. While the so called Euler description uses a fixed control volume and monitors the fluid passing through, the Lagrangian description tracks a particle of the fluid on its way through space. In CFD, where the spatial discretization is usually done by the computational grid, the Euler description is more common and therefore will be used in this section. The relevant equations can be found in most books on fluid mechanics. For this section, mostly Noll [63], Ehrenfried [13] and the handbook of the code employed, AVBP [2], are used.

2.1.1 The Conservation of Mass

The conservation of mass can be derived by considering the mass-fluxes entering and leaving an infinitely small volume element. In the absence of a source of mass, the equation of the conservation of mass can be written as follows:

$$\frac{\partial \rho}{\partial t} + \frac{\partial \left(\rho u_{\mathrm{i}}\right)}{\partial x_{\mathrm{i}}} = 0. \tag{2.1}$$

In the context of reactive flows a formulation of the conservation of mass for n species is desirable. In this case a species source term or sink term $\mathscr{S}_{\mathrm{k}}$ is likely to be present due to the reaction. In contrast to the total mass balance, a diffusion term has to be included here, since species fractions may be spatially non-uniform. Defining the mass fraction of the species k:

$$Y_{\mathrm{k}} = \frac{\rho_{\mathrm{k}}}{\sum\limits_{\mathrm{i=1}}^{\mathrm{n}} \rho_{\mathrm{k}}}, \tag{2.2}$$

$$\frac{\partial \left(\rho Y_{\mathrm{k}}\right)}{\partial t} + \frac{\partial \left(\rho u_{\mathrm{j}} Y_{\mathrm{k}}\right)}{\partial x_{\mathrm{j}}} = \frac{\partial}{\partial x_{\mathrm{j}}} \left[\rho D_{\mathrm{k}} \frac{M_{\mathrm{k}}}{M} \frac{\partial X_{\mathrm{k}}}{\partial x_{\mathrm{j}}} - Y_{\mathrm{k}} V_{\mathrm{i}}^{\mathrm{c}}\right] + \mathscr{S}_{\mathrm{i}}, \tag{2.3}$$

where the first term on the right hand side accounts for diffusion, with X_{k} being the molar fraction of species k, M_{k} the molar weight of species k and D_{k} being the diffusion coefficient for species k. The term $V_{\mathrm{i}}^{\mathrm{c}}$ is defined as

$$V_{\mathrm{i}}^{\mathrm{c}} = \sum_{k=1}^{n} D_k \frac{M_{\mathrm{k}}}{M} \frac{\partial X_{\mathrm{k}}}{\partial x_{\mathrm{i}}} \tag{2.4}$$

and ensures global mass conservation after introduction of the diffusion law [2].

2.1.2 The Compressible Navier-Stokes Equations

The Navier-Stokes equations are named after the French mathematician and physician Claude Louis Marie Henri Navier (1785-1836) and the Irish mathematician and physician Sir George Gabriel Stokes (1819-1903). The equations can be derived from a balance of momenta at a fluid element. Furthermore, a non-negligible friction and a Newton type fluid with the viscosity μ as well as volume forces V_{i} are assumed. A shear stress tensor τ_{ij} can be defined to simplify the equation:

$$\frac{\partial\left(\rho u_{\mathrm{i}}\right)}{\partial t}+\frac{\partial\left(\rho u_{\mathrm{j}} u_{\mathrm{i}}\right)}{\partial x_{\mathrm{j}}}=-\frac{\partial p}{\partial x_{\mathrm{i}}}+\frac{\partial}{\partial x_{\mathrm{j}}}\left[\eta\left(\frac{\partial u_{\mathrm{i}}}{\partial x_{\mathrm{j}}}+\frac{\partial u_{\mathrm{j}}}{\partial x_{\mathrm{i}}}-\frac{2}{3}\delta_{\mathrm{ij}}\frac{\partial u_{\mathrm{k}}}{\partial x_{\mathrm{k}}}\right)\right]+\rho V_{\mathrm{i}}, \tag{2.5}$$

$$\frac{\partial\left(\rho u_{\mathrm{i}}\right)}{\partial t}+\frac{\partial\left(\rho u_{\mathrm{j}} u_{\mathrm{i}}\right)}{\partial x_{\mathrm{j}}}=-\frac{\partial p}{\partial x_{\mathrm{i}}}+\frac{\partial}{\partial x_{\mathrm{j}}}\tau_{\mathrm{ij}}+\rho V_{\mathrm{i}}. \tag{2.6}$$

2.1.3 The Conservation of Energy

In the case of reactive flow, a balance of the internal energy of the fluid has to be established, because substantial changes in the distribution of the energy take place. The total energy of a fluid is the combination of internal energy (e_{int}) and kinetic energies ($u^2/2$), $E = e_{\mathrm{int}} + u^2/2$. The specific internal energy per unit volume can be expressed as [6]

$$e_{\mathrm{int}} = h-\frac{p}{\rho}=\int_{T_0}^{T} c_p dT-\frac{p}{\rho}. \tag{2.7}$$

Assuming a source of chemical energy and radiation energy $\mathscr{S}_{\mathrm{T}}$ the equation of energy becomes [2]:

$$\frac{\partial\left(\rho E\right)}{\partial t}+\frac{\partial\left(\rho u_{\mathrm{j}} E\right)}{\partial x_{\mathrm{j}}}=-\frac{\partial}{\partial x_{\mathrm{j}}}\left[u_{\mathrm{i}}\left(p\delta_{\mathrm{ij}}-\tau_{\mathrm{ij}}\right)+q_{\mathrm{j}}\right]+\mathscr{S}_{\mathrm{T}}, \tag{2.8}$$

where

$$q_{\mathrm{j}} = -\lambda\frac{\partial T}{\partial x_{\mathrm{i}}}-\rho\sum_{k=1}^{N}\left(D_{\mathrm{k}}\frac{M_{\mathrm{k}}}{M}\frac{\partial X_{\mathrm{k}}}{\partial x_{\mathrm{i}}}-Y_{\mathrm{k}}V_{\mathrm{i}}^{\mathrm{c}}\right)h_{\mathrm{s,k}} \tag{2.9}$$

expresses the heat conduction. The second term evolves due to species diffusion and is not further explained here. Non-reactive flows at low Mach numbers often have a negligible change in internal energy and therefore the equation for the conservation of energy can be neglected in these cases.

2.1.4 The Navier-Stokes System of Equations

The equations for the conservation of mass, momentum and energy all follow the same general form of the transport equation [2]:

$$\frac{\partial \vec{w}}{\partial t} + \nabla \vec{F} = \vec{\mathscr{S}}, \tag{2.10}$$

where w denotes the conservative variables ($\vec{w} = \left(\rho u_1, \rho u_2, \rho u_3, \rho E, \rho\right)^T$), $\vec{F}$ the fluxes and $\vec{\mathscr{S}}$ the source terms.
Some authors [69] name this set of transport equations the Navier-Stokes system of equations or just the Navier-Stokes equations, which may lead to confusion with 2.1.2.

2.1.5 The Euler Equations

The Navier-Stokes equations are the basis for the Computational Fluid Dynamics (CFD) part of this work. When it comes to purely acoustic equations, further simplifications of these equations can be performed. These simplified equations will play an important role in the low order modeling described in 2.7. The first step for this are the Euler equations.
The term Euler equation can, similarly to Navier-Stokes equation, either denote only the equation of conservation of momentum or the entire system of equations describing the behavior of a fluid. The Euler equations are a simplification of the Navier-Stokes equations assuming a non-viscous flow and absence of volume forces. Therefore the viscous terms in equation 2.6 and the shear terms in 2.8 can be eliminated and the equations of the conservation of mass, momentum and energy reduce to:

$$\frac{\partial \rho}{\partial t} + \frac{\partial \left(\rho u_{\mathrm{i}}\right)}{\partial x_{\mathrm{i}}} = 0, \tag{2.11}$$

$$\frac{\partial \left(\rho u_{\mathrm{i}}\right)}{\partial t} + \frac{\partial \left(\rho u_{\mathrm{j}} u_{\mathrm{i}}\right)}{\partial x_{\mathrm{j}}} = -\frac{\partial p}{\partial x_{\mathrm{i}}}, \tag{2.12}$$

$$\frac{\partial \left(\rho E\right)}{\partial t} + \frac{\partial \left(\rho u_{\mathrm{j}} E\right)}{\partial x_{\mathrm{j}}} = -\frac{\partial}{\partial x_{\mathrm{j}}}\left(u_{\mathrm{i}} P + q_{\mathrm{j}}\right) + \mathscr{S}_{\mathrm{T}}. \tag{2.13}$$

2.2 Basic Equations of Acoustics

The Euler equations still include full flow information, e.g. transient flow and locally non-constant flow. When it comes to acoustics, such mean flow effects are often of low interest and can be simplified or neglected.

2.2.1 The Acoustic Wave Equation

The acoustic wave equation can be derived from the Euler equation (for mass and momentum) and an equation of state coupling pressure and density ($p = p(\rho)$) [13]. This is done by dividing the quantities into a mean value (e.g. $\bar{p}$) and a perturbation (e.g.. p'). We do not consider turbulent effects here. Hence:

$$p = \bar{p} + p', \tag{2.14}$$

$$\rho = \bar{\rho} + \rho'. \tag{2.15}$$

And assuming no mean flow $\bar{u}_\mathrm{i} = 0$:

$$u_\mathrm{i} = \bar{u}_\mathrm{i} + u'_\mathrm{i} = u'_\mathrm{i}. \tag{2.16}$$

Neglecting higher order perturbation terms (e.g. $p' u'_\mathrm{i}$) one obtains for the linearized conservation of mass and momentum (linearized Euler):

$$\frac{\partial \rho'}{\partial t} + \bar{\rho}\frac{\partial u'_\mathrm{i}}{\partial x_\mathrm{i}} = 0, \tag{2.17}$$

$$\bar{\rho}\frac{\partial u'_\mathrm{i}}{\partial t} = -\frac{\partial p'}{\partial x_\mathrm{i}}. \tag{2.18}$$

Using now a relation between pressure and density, i.e. an equation of state, and expanding it using a Taylor series

$$p(\rho) = p(\rho_0) + (\rho - \rho_0)\frac{dp}{d\rho}(\rho_0) + \dots, \tag{2.19}$$

we get a relation between p' and ρ':

$$p' = \rho'\frac{dp}{d\rho}. \tag{2.20}$$

The term $\frac{dp}{d\rho}$ is defined as $\frac{dp}{d\rho} = c^2$ with c being the speed of sound. In the case of an ideal gas one obtains $c = \sqrt{RT}$. So the last equation can be rewritten:

$$p' = \rho' c^2. \tag{2.21}$$

Now if one performs a time derivative of the linearized conservation of mass (2.17) and calculates the divergence of the linearized Euler equation (2.18),

$$\frac{\partial^2 \rho'}{\partial t^2} + \bar{\rho} \frac{1}{\partial x_\mathrm{i}} \frac{\partial u'_\mathrm{i}}{\partial t} = 0, \tag{2.22}$$

$$\bar{\rho} \frac{1}{\partial x_\mathrm{i}} \frac{\partial u'_\mathrm{i}}{\partial t} = -\frac{1}{\partial x_\mathrm{i}} \frac{\partial p'}{\partial x_\mathrm{i}}, \tag{2.23}$$

and finally subtracts the two equations and uses equation 2.21, one obtains the wave equation:

$$\frac{1}{c^2} \frac{\partial^2 p'}{\partial t^2} - \frac{\partial^2 p'}{\partial x_\mathrm{i}^2} = 0. \tag{2.24}$$

In the presence of mean flow, this equation is no longer valid. Nevertheless, for a uniform mean flow the equation can be applied by using it for a moving coordinate system (x_m and t_m) and transferring it into a stationary one (x_s and t_s):

$$x_\mathrm{s} = x_\mathrm{m} + \bar{u} t, \tag{2.25}$$

$$x_\mathrm{m} = x_\mathrm{s} - \bar{u} t, \tag{2.26}$$

$$t_\mathrm{s} = t_\mathrm{m}. \tag{2.27}$$

This implies for the derivatives:

$$\frac{\partial}{\partial x_\mathrm{m}} = \frac{\partial}{\partial x_\mathrm{s}}, \tag{2.28}$$

$$\frac{\partial}{\partial t_\mathrm{m}} = \frac{\partial}{\partial t_\mathrm{s}} + \bar{u} \frac{\partial}{\partial x_\mathrm{s}}. \tag{2.29}$$

Inserting this into the wave equation results in the convective wave equation for uniform flow (in the stationary coordinate system):

$$\frac{1}{c^2} \left(\frac{\partial}{\partial t} + \bar{u} \frac{\partial}{\partial x} \right)^2 p' - \frac{\partial^2 p'}{\partial x_\mathrm{i}^2} = 0. \tag{2.30}$$

2.2.2 The Helmholtz Equation

The Helmholtz equation corresponds to the wave equation in frequency domain. Assuming a harmonic pressure signal at an angular frequency $\omega = 2\pi f$ of the form

$$p' = \hat{p}' e^{i\omega t}, \tag{2.31}$$

the time derivatives of the pressure are:

$$\frac{\partial p'}{\partial t} = i\omega \hat{p} e^{i\omega t}, \tag{2.32}$$

$$\frac{\partial^2 p'}{\partial t^2} = -\omega^2 \hat{p} e^{i\omega t}. \tag{2.33}$$

Introducing this into equation 2.24 and defining a wave number $k = \omega / c_0$ one obtains the Helmholtz equation:

$$k^2 p' + \frac{\partial^2 p'}{\partial x_\mathrm{i}^2} = 0. \tag{2.34}$$

2.2.3 Characteristic Waves

Characteristic waves are of interest, because they represent a simple solution for the wave equation in one dimension. Therefore, they are frequently used in low order modeling, e.g. in the models presented in section 2.7. For 1D cases, such as ducts and other elongated systems, equation 2.24 becomes

$$\frac{1}{c_0^2} \frac{\partial^2 p'}{\partial t^2} - \frac{\partial^2 p'}{\partial x^2} = 0, \tag{2.35}$$

with x being the longitudinal axis. The solution of this equation can be expressed as a superposition of two waves ($\mathfrak{f}$ and $\mathfrak{g}$) travelling in positive and negative x-direction, respectively:

$$p' = \rho c \left(\mathfrak{f}(t - x/c_0) + \mathfrak{g}(t + x/c_0) \right). \tag{2.36}$$

In the frequency domain, these waves can be expressed using an exponential approach:

$$\mathfrak{f} = \hat{\mathfrak{f}}_0 e^{i(\omega t - kx)}, \tag{2.37}$$

$$\mathfrak{g} = \hat{\mathfrak{g}}_0 e^{i(\omega t + kx)}. \tag{2.38}$$

$\mathfrak{f}$ and $\mathfrak{g}$ are sometimes referred to as characteristic waves or Rieman Invariants. [72]. The wave number k is defined as follows:

$$k = \frac{\omega}{c}. \tag{2.39}$$

If mean flow is present, the conventional wave equation is no longer valid. Still, similarly to the wave equation, for uniform mean flow, the solution can be transformed. This again is done using a moving reference system (x_m and t_m) and transferring it into a stationary one (x_s and t_s):

$$x_\mathrm{s} = x_\mathrm{m} + \bar{u}t, \tag{2.40}$$

$$x_\mathrm{m} = x_\mathrm{s} - \bar{u}t, \tag{2.41}$$

$$t_\mathrm{s} = t_\mathrm{m}. \tag{2.42}$$

Time is not affected by the choice of the coordinate system. The pressure also does not depend on the choice of the coordinate system:

$$p'_\mathrm{s}(x_\mathrm{s}, t) = p'_\mathrm{m}(x_\mathrm{m}, t) = p'_\mathrm{m}(x_\mathrm{s} - \bar{u}t, t). \tag{2.43}$$

Using the relation between p, $\mathfrak{f}$ and $\mathfrak{g}$, equation 2.36, one obtains:

$$p'(x_\mathrm{s}, t) = \rho c \left(\mathfrak{f}(t - \frac{x_\mathrm{s}}{c_0 + \bar{u}} + \mathfrak{g}(t + \frac{x_\mathrm{s}}{c_0 - \bar{u}} \right). \tag{2.44}$$

The wave numbers k are then defined differently for the upstream (k^-) and downstream (k^+) traveling wave:

$$k^+ = \frac{\omega}{c + \bar{u}}, \tag{2.45}$$

$$k^- = \frac{\omega}{c - \bar{u}}. \tag{2.46}$$

Inserting this into equations 2.37 and 2.38, one obtains a valid solution for the 1D wave equation in uniform flow.

2.3 Turbulence

Turbulence is an important aspect in technical problems. In the context of thermo-acoustics, turbulence-flame interaction is of particular interest. Turbulence also is one of the major challenges when it comes to the numerical

simulation of fluid dynamics as will be demonstrated in section 2.4. Therefore, basic properties of turbulent flows are presented in this section.
In turbulent flow the inertial forces dominate over viscous forces. Therefore, in contrast to the laminar structure of flow dominated by viscous effects, turbulent flow is characterized by a fluctuation of the local properties of the flow [72]. Hence, the flow quantities (e.g. u) can be divided into a mean ($\bar{u}$) and a fluctuating ($\tilde{u}$) part:

$$u = \bar{u} + \tilde{u}. \tag{2.47}$$

The ratio of inertial and viscous forces can be described using the Reynolds number,

$$\mathrm{Re} = \frac{u \cdot l}{\nu}, \tag{2.48}$$

where l and u denote characteristic length and velocity and ν the kinematic viscosity. If the Reynolds number exceeds a certain critical Reynolds number $\mathrm{Re}_{\mathrm{crit}}$, which depends on the flow configuration and usually is e.g., in the case of duct flow, $\mathrm{Re}_{\mathrm{crit}} = 2000$, the flow becomes turbulent. Turbulent structures have a large spectrum of sizes. The largest structures have a size imposed by external factors (l_{e}), mostly the geometry, while the size of the smallest turbulent structures is determined by internal fluid properties (l_{i}). The energy is transferred from larger to smaller structures until viscous effects become predominant and the energy dissipates from the smallest structures. Richardson described this phenomenon already in 1922 as "*big whirls have little whirls that feed on their velocity, and little whirls have lesser whirls and so on to viscosity*" [86].
The mean rate of dissipation of energy per unit of mass and time can be estimated by

$$\epsilon = \frac{1}{2}\nu \sum \left(\frac{\partial u_{\mathrm{i}}}{\partial x_{\mathrm{i}}} + \frac{\partial u_{\mathrm{j}}}{\partial x_{\mathrm{j}}} \right)^2 . \tag{2.49}$$

According to Kolmogorov [39–41], the largest scales are independent of the Reynolds number. Therefore, they are not affected by viscous phenomena. In contrast, smaller scales are dominated by the viscous effects and turbulence becomes locally isotropic. The smallest scale, also denoted Kolmogorov Scale, can be estimated with

$$l_{\mathrm{i}} = \left(\frac{\nu^3}{\epsilon}\right)^{\frac{1}{4}}. \tag{2.50}$$

The different scales can be considered as different frequencies in the wave number spectrum. Assuming a constant rate of dissipation and production, it is possible to derive a relation for the energy contained in every scale (k):

$$E(k) = C\epsilon^{\frac{2}{3}} k^{-\frac{5}{3}}. \tag{2.51}$$

This is Kolmogorov's famous law for the $-\frac{5}{3}$ decay for the turbulent kinetic energy. The typical spectrum of turbulent kinetic energy is represented in figure 2.1

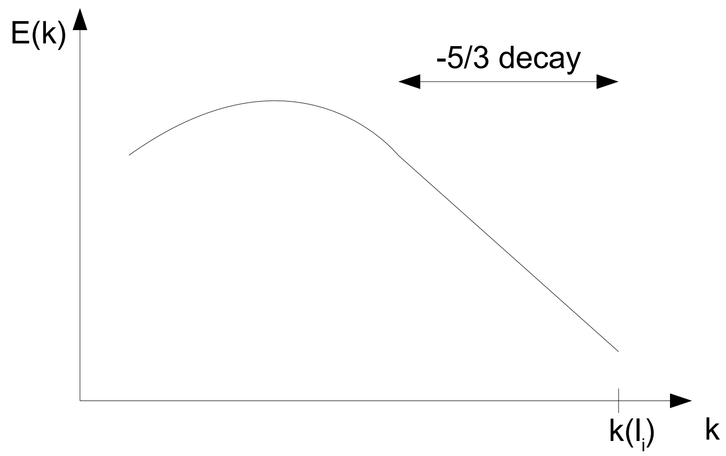

Figure 2.1: Representation of the turbulent energy Spectrum.

2.4 Modelling strategies for Fluid Mechanics

The analytical solution of the Navier-Stokes set of equations 2.10 is only possible for a few simple cases. If a solution for these equations is desired in more

complex geometries, a numerical approximation has to be performed. For representing the flow on a numerical grid, a certain degree of resolution has to be achieved. This degree, corresponding to the fineness of the grid used for the computation, depends on the smallest structures, which occur in the flow. If no further modeling is done, the finest structures in the flow have the size of the Kolmogorov Scale l_i (see equation 2.50).
Three main different approaches for the modeling of turbulent flows can be distinguished. They differ in their level of modeling and in their demand for computational power. Reynolds Averaged Navier-Stokes Method (RANS) has the highest level of modeling and therefore the lowest demand for computational power. An intermediate level of modeling and computational demand is needed for Large Eddy Simulation (LES). Lastly, Direct Numerical Simulation (DNS) requires no modeling of turbulent effects and, therefore, has the highest computational demand. The level of modeling and the level of resolution are represented in figure 2.2. The latter two methods are described in the following subsections.

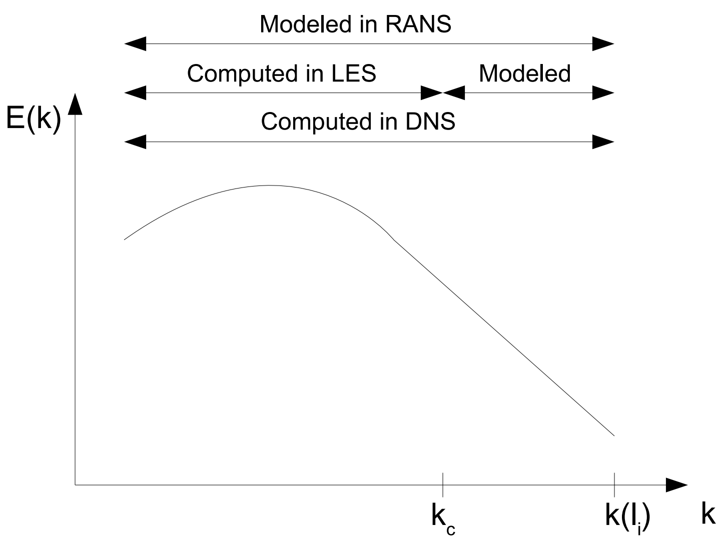

Figure 2.2: Representation of the modeling and resolution of the different kinds of numerical simulations over the turbulent energy spectrum. k_c denotes the cutoff frequency of the LES calculation. Figure as in [72].

2.4.1 Direct Numerical Simulation (DNS)

DNS is the straightforward simulation of the Navier-Stokes equations and is therefore briefly explained here, as first class of numerical simulation. DNS does not use any kind of modeling for the turbulence. Therefore it can be applied if the grid used for the simulation is fine enough to resolve all fluid motion scales. As the smallest scale l_i correlates to viscosity and velocity gradient with equation (2.50),

$$l_\mathrm{i} = \left(\frac{\nu^3}{\epsilon}\right)^{\frac{1}{4}}, \tag{2.52}$$

a dependency of the Reynolds number can be established:

$$\frac{l}{l_\mathrm{i}} = l\left(\frac{\nu^3}{\epsilon}\right)^{-\frac{1}{4}} \approx \mathrm{Re}^{\frac{3}{4}}. \tag{2.53}$$

So the number of grid points required for a DNS in three dimensions scales with $\left(\frac{1}{l_\mathrm{i}}\right)^3 = \mathrm{Re}^{\frac{9}{4}}$. Assuming now a linear dependency (which is the case for explicit solvers) between time step and grid spacing, the computational effort for a given problem in time and space correlates with Re^3. Hence, direct numerical simulation is only feasible for small Reynolds numbers. However, the increasing power available in computing makes DNS possible for larger problems.

2.4.2 Large Eddy Simulation (LES)

In LES, as the name implies, the large scales of turbulence are simulated, while the smaller scales have to be modeled. Therefore, the grid can be coarser compared to DNS which saves computational power. On the other hand, resolving the large eddies is an essential difference compared to Reynolds Averaged Navier-Stokes calculation (RANS): In RANS all turbulent scales are modeled. For the treatment of thermo-acoustic problems, LES has the big advantage that by resolving turbulent scales, it permits the explicit calculation of interactions between turbulence and flame. Hence, LES can be seen as a promising

compromise between DNS and RANS both in resolution and computational effort.
In order to only resolve the large scales, the flow field has to be filtered by the simulation in the sense of a low pass filter. Usual filters are box, Gauss or Fourier cutoff functions. Hence, we know that LES commits an error by filtering the Navier-Stokes equation. Therefore, it is possible to account for this error. This is done by introducing a so called “sub grid model”, which aims to take into account the effect of the scales that fall below the size of the grid. Computationally, LES is a compromise between resolution and computational demand.

Equations

A filtering operation consists of applying a filter kernel G to a quantity ϕ:

$$\langle\phi\rangle = G \star \phi = \int_{-\infty}^{\infty}\int_{-\infty}^{\infty} \phi(\xi, t')G(x-\xi, t-t')\,dt'\,d^3\xi. \tag{2.54}$$

Applying the filtering (denoted by $\langle\rangle$) to the Navier-Stokes equations (2.10) results in:

$$\frac{\partial\left(\rho\langle u_\mathrm{i}\rangle\right)}{\partial t} + \frac{\partial\left(\rho\langle u_\mathrm{j} u_\mathrm{i}\rangle\right)}{\partial x_\mathrm{j}} = -\frac{\partial\langle p\rangle}{\partial x_\mathrm{j}} + \frac{\partial}{\partial x_\mathrm{j}}\langle\tau_\mathrm{ij}\rangle. \tag{2.55}$$

The second term on the left hand side cannot be resolved directly. If one assumes that the term $\langle u_\mathrm{j} u_\mathrm{i}\rangle$ must be expressed by filtered quantities $\langle u_\mathrm{i}\rangle\langle u_\mathrm{j}\rangle$, it is possible to use the Leonard decomposition by expanding $\langle u_\mathrm{j} u_\mathrm{i}\rangle$. Using $u = \langle u\rangle + \grave{u}$ leads to following expression (where $\grave{u}$ here denotes the part not resolved by the filter) [91]:

$$\langle u_\mathrm{i} u_\mathrm{j}\rangle - \langle u_\mathrm{i}\rangle\langle u_\mathrm{j}\rangle = \underbrace{\langle\langle u_\mathrm{i}\rangle\langle u_\mathrm{j}\rangle\rangle - \langle u_\mathrm{i}\rangle\langle u_\mathrm{j}\rangle}_{L_\mathrm{ij}} + \underbrace{\langle\grave{u}_\mathrm{i}\langle u_\mathrm{j}\rangle\rangle + \langle\langle u_\mathrm{i}\rangle\grave{u}_\mathrm{j}\rangle}_{C_\mathrm{ij}} + \underbrace{\langle\grave{u}_\mathrm{i}\grave{u}_\mathrm{j}\rangle}_{R_\mathrm{ij}}. \tag{2.56}$$

This term can be considered as a subgrid scale viscous term $\tau^\star_\mathrm{ij}$:

$$\tau^\star_\mathrm{ij} = \langle u_\mathrm{i} u_\mathrm{j}\rangle - \langle u_\mathrm{i}\rangle\langle u_\mathrm{j}\rangle = L_\mathrm{ij} + C_\mathrm{ij} + R_\mathrm{ij}. \tag{2.57}$$

Where according to [6]

- R_{ij} denotes the Reynolds Stress Tensor which describes the interaction between small scales transferring energy from small to large scales ("backscatter"),
- C_{ij} denotes the Cross Stress Tensor which describes the interaction between large and small scales,
- L_{ij} denotes the Leonard Stress Tensor which describes the interaction between resolved scales transferring energy to the small scales ("outscatter").

This term $\tau^{\star}_{\mathrm{ij}}$ has to be modeled in order to close equation 2.55 which then takes the form

$$\frac{\partial\left(\rho\langle u_{\mathrm{i}}\rangle\right)}{\partial t}+\frac{\partial\left(\rho\langle u_{\mathrm{j}}\rangle\langle u_{\mathrm{i}}\rangle\right)}{\partial x_{\mathrm{j}}}=-\frac{\partial\langle p\rangle}{\partial x_{\mathrm{j}}}+\frac{\partial}{\partial x_{\mathrm{j}}}\left[\langle\tau_{\mathrm{ij}}\rangle+\tau^{\star}_{\mathrm{ij}}\right]. \tag{2.58}$$

Different approaches have been developed for approximating $\tau^{\star}_{\mathrm{ij}}$. An overview is given e.g. in [6] or [91]. In the following, two models are described which are both implemented in the LES solver used in the context of this thesis, AVBP.

The Smagorinsky Model

One of the most commonly used models for the unresolved terms was developed by Smagorinsky [100] in 1963. Smagorinsky introduces a subgrid scale viscosity, which depends on the filtered deformation tensor $\langle D_{\mathrm{ij}}\rangle$,

$$\nu_{\mathrm{sgs}}=\left(C_{\mathrm{s}}\bar{\delta}\right)^2\left(2\langle D_{\mathrm{ij}}\rangle\langle D_{\mathrm{ij}}\rangle\right)^{1/2}, \tag{2.59}$$

with

$$\langle D_{\mathrm{ij}}\rangle=\frac{1}{2}\left(\frac{\partial\langle u_{\mathrm{i}}\rangle}{\partial x_{\mathrm{j}}}+\frac{\partial\langle u_{\mathrm{j}}\rangle}{\partial x_{\mathrm{i}}}\right) \tag{2.60}$$

This expression can be calculated directly from the flow field. The Smagorinsky constant C_{k} can be estimated to be $C_{\mathrm{s}}=0.18$ [59]

The WALE Model

This is the subgrid scale model used in the simulations presented in this thesis. It has been chosen because the Smagorinsky Model exhibits some disadvantages:

- The near wall properties are not correct: in real flow turbulent fluctuations are damped, while the Smagorinsky model proposes an eddy viscosity which is non-zero.
- The energy dissipation in eddies also is not properly accounted for in the Smagorinsky model. [59].

Nicoud and Ducros have proposed a formulation to overcome these problems [59]. It regards not only on the irrotational strain rate, but also on the rotational one. It is based on the "*traceless symmetric part of the square of the velocity gradient tensor*" [59],

$$S_{\mathrm{ij}} = \frac{1}{2}\left(\langle g_{\mathrm{ij}}\rangle^2 + \langle g_{\mathrm{ji}}\rangle^2\right) - \frac{1}{3}\delta_{\mathrm{ij}}\langle g_{\mathrm{kk}}\rangle^2. \tag{2.61}$$

Defining

$$\langle\Omega_{\mathrm{ij}}\rangle = \frac{1}{2}\left(\frac{\partial\langle u_{\mathrm{i}}\rangle}{\partial x_{\mathrm{j}}} - \frac{\partial\langle u_{\mathrm{j}}\rangle}{\partial x_{\mathrm{i}}}\right), \tag{2.62}$$

the tensor can be rewritten:

$$S_{\mathrm{ij}} = \langle D_{\mathrm{ik}}\rangle\langle D_{\mathrm{kj}}\rangle + \langle\Omega_{\mathrm{ik}}\rangle\langle\Omega_{\mathrm{kj}}\rangle - \frac{1}{3}\delta_{\mathrm{ij}}(\langle D_{\mathrm{mn}}\rangle\langle D_{\mathrm{mn}}\rangle - \langle\Omega_{\mathrm{mn}}\rangle\langle\Omega_{\mathrm{mn}}\rangle) \tag{2.63}$$

The desired near wall behavior now imposes the exponents and the form of the denominator of the final formulation of the turbulent viscosity: [59]

$$\nu_{\mathrm{sgs}} = \left(C_{\mathrm{s}}\bar{\delta}\right)^2 \frac{(S_{\mathrm{ij}}S_{\mathrm{ij}})^{3/2}}{(\langle D_{\mathrm{ij}}\rangle\langle D_{\mathrm{ij}}\rangle)^{5/2}(S_{\mathrm{ij}}S_{\mathrm{ij}})^{5/4}}. \tag{2.64}$$

A separate section (section 4.2) is dedicated to boundary conditions used for the LES simulations in this thesis.

2.5 Combustion

In the field of thermo-acoustics, the simulation of heat release and hence of combustion is an important task. The basic phenomena occurring during combustion processes are described in this section as is the numerical treatment in simulations.
Combustion is an exothermic chemical reaction between a fuel and an oxidant resulting in the production of heat or light or both. Turns [107] e.g. defines combustion as a "*rapid oxidation generating heat or both light and heat...*". About 90% of the energy used worldwide is provided by combustion processes [111].
In a combustion process, the reactants, which are chemically on a high energy level, react and form products, which are on a chemically lower and therefore more stable level of energy. The difference of energy is released in the form of radiation, which corresponds to the "heat and light" mentioned above. The energy available q_{c} through the chemical reaction can be quantified by the standard enthalpy of formation ΔH_{f}:

$$q_{\mathrm{c}} = \Delta H_{\mathrm{f,educt}} - \Delta H_{\mathrm{f,prod}}. \tag{2.65}$$

Knowing the rate of generation of species k, $\mathscr{S}_{\mathrm{k}}$, the energy source term, $\mathscr{S}_{\mathrm{T}}$, can be written as [2]

$$\mathscr{S}_{\mathrm{T}} = -\sum_{k=1}^{n} \mathscr{S}_{\mathrm{k}} \Delta H_{\mathrm{f,k}}. \tag{2.66}$$

The standard enthalpy of formation quantifies the energy contained in the chemical bond with reference to a standard level for the elements.
The chemical reaction in the case of an alkane hydrocarbon fuel $C_{\mathrm{n}} H_{\mathrm{2n+2}}$ has the form

$$C_{\mathrm{n}} H_{\mathrm{2n+2}} + (3n+1)/2 O_2 \rightarrow nCO_2 + (n+1) H_2 O. \tag{2.67}$$

The amount of $2n+1$ oxygen molecules is the minimum amount of oxygen required for complete combustion and named stoichometric amount. An excess or lack of oxygen can be characterized by the equivalence ratio ϕ or the air excess ratio $\lambda = \frac{1}{\phi}$. The equivalence ratio is defined

$$\phi = \frac{m_{\mathrm{stoic}}}{m}, \tag{2.68}$$

where m denotes the amount of fuel available and m_{stoic} the stoichometric amount of fuel. This energy and the heat capacity of the products permits the adiabatic flame temperature to be defined as follows:

$$T_{\mathrm{adiab}} = \frac{q_{\mathrm{c}} \cdot Y_{\mathrm{fuel}}}{c_{\mathrm{p}}} + T_0. \tag{2.69}$$

For simplicity reasons, c_{p} is assumed not to be temperature dependent here. For temperature dependent c_{p}, the adiabatic flame temperature can be determined from the following equation:

$$h(T_{\mathrm{adiab}}) - h(T_0) = q \cdot Y_{\mathrm{fuel}}. \tag{2.70}$$

AVBP e.g. uses tabled values for the enthalpy permitting the solution of this equation.
The reaction rate $\dot{\omega}$ of the reaction process is often modeled using an Arrhenius type temperature and species dependency,

$$\dot{\omega} = AY_{\mathrm{F}} Y_{\mathrm{O}} \exp\left(\frac{T_{\mathrm{a}}}{T}\right), \tag{2.71}$$

where A and T_{a} are model constants and Y_{F} and Y_{O} fuel and oxidizer mass fractions, respectively. Depending on the state of the flow and on the mixture of the reactants, different regimes of combustion can be distinguished. The flow can be either laminar or turbulent. Hence, laminar and turbulent combustion can be defined. The reactants can either be separate (non-premixed), partially premixed[1] or perfectly premixed. If non-gaseous fuels are used, additional phenomena like droplet formation and evaporation have to be considered. This work focuses on gaseous fuel and therefore droplet formation and evaporation is not discussed further. The reader is referred to standard work like [107, 112].

2.5.1 Non-Premixed Combustion

In the case of non-premixed combustion the reactants mix during the combustion process in the combustion zone. Depending on the flow, turbulent

[1]According to the statistical properties of the partially premixed combustion a further distinction is possible. See e.g.. [12] for further information

and laminar non-premixed combustion can be distinguished. The latter is often referred to as laminar diffusion flames. In non-premixed combustion the mixing of the reactants is a crucial element when the global kinetics of the system have to be described. Therefore, the flame and its position are particularly sensitive to influences of the flow field which brings fuel and oxygen together. Due to the importance of the mixing process often an infinitely fast chemistry is assumed when modeling laminar diffusion flames. This assumption implies that fuel and oxygen react immediately when mixing occurs. In this way, the combustion problem is reduced basically to the mixing problem.

2.5.2 Premixed Combustion

Here, a flame front propagates through the mixture of fresh (meaning unburnt) reactants. The surface of the flame front and the flame speed determine the overall reaction rate. For hydrocarbon fuels, the flame front has a thickness δ_L^0 of the order of 0.1 mm and a flame speed s_L^0 of the order of 0.5 m/s. In the presence of turbulence, the flame front can be deformed or wrinkled by the eddies leading to a bigger surface of the flame front and higher combustion rates. Therefore, a turbulent flame speed s_T can be defined as the velocity that has to be imposed at the inlet of a turbulent domain (of volume V) of constant cross section A in order to keep the flame stationary:

$$A\rho_1 Y_F^1 s_t = -\int_V \dot{\omega}_F dV; \tag{2.72}$$

Y_F^1 and ρ_1 denote the fuel mass fraction and the density of the unburnt mixture. The ratio between laminar and turbulent flame speed corresponds to the area gain of the flame front caused by the wrinkling,

$$\frac{s_t}{s_l} = \frac{S_T}{S}. \tag{2.73}$$

Hence, it is possible to describe the influence of turbulence defining a wrinkling factor Ξ as

$$\Xi = \frac{A_T}{A}. \tag{2.74}$$

Increasing turbulence will increase the wrinkling and therefore increase the turbulent burning velocity. However, one has to keep in mind that with increasing turbulent velocity fluctuation quenching effects may dominate the behavior.

2.6 Numerical Simulation of Combustion

The simulation of combustion is challenging because of the coupling between combustion and turbulence and the occurrence of extreme gradients due to the typically thin reaction zone. The type of modeling of the reaction mechanism depends essentially on the type of simulation and the treatment of turbulence. RANS approaches solve the mean quantities of the flow field; therefore RANS combustion models will only provide a mean reaction zone and turbulence influences have to be included explicitly into the modeling. In contrast, DNS resolves the fully turbulent flow field and therefore the influences on the reaction. The grid is fine enough, so that the thin reaction zone with its steep gradients can be resolved. The major drawback is the high computational requirement, which restricts the application of DNS. Again, LES presents the intermediate solution, where large scale transient effects and large scale turbulence are resolved. The effects of small scale turbulence have to be accounted for separately. A second problem of combustion modeling in LES is the thin reaction zone, which usually can not be represented sufficiently on the grid.

2.6.1 Thickened Flame Model

The thickened flame model by Colin et al. [7] is an approach based on a global reaction scheme to model the species transformation during the reaction. The main idea of the model is to increase the diffusion transport in a way such that the reaction zone thickens up and, hence, can be represented on the numerical grid. In a second step, the reaction rate is reduced in order to compensate the effects of the diffusion. Butler et al. [64] have proposed an approach to artificially thicken the flame front in this way. The flame speed s_L^0 and the flame thickness δ_L^0 can be expressed as

$$s_L^0 = \sqrt{D_{th} B}, \tag{2.75}$$

$$\delta_L^0 \propto \frac{D_{th}}{s_L^0} = \sqrt{\frac{D_{th}}{B}}, \tag{2.76}$$

where D_{th} represents the thermal diffusivity and B the pre-exponential factor. If the thermal diffusivity is increased by a factor F and at the same time the pre-exponential factor is reduced by the same factor, the laminar flame speed is preserved and the thickness is increased by this factor F. This procedure affects the ratio between turbulent and chemical time scale, the Damköhler number Da, and, hence, the reaction of the flame to turbulence:

$$Da_{\text{thickened}} = \frac{Da}{F}. \tag{2.77}$$

This implies that the flame is more insensitive to small scale turbulent motions. The reaction on eddies which are smaller than the thickened flame thickness vanishes and the reaction on eddies bigger than the thickened flame thickness may be modified. An efficiency function $\mathscr{E}$ is introduced in order to compensate for this effect [1, 7]. This function is based on the wrinkling factor of unthickened (^{0}) and thickened (^{1}) flame:

$$\mathscr{E} = \frac{\Xi(\delta_l^0)}{\Xi(\delta_l^1)} = \frac{1 + \alpha\Gamma(\Delta_e/\delta_l^0, u'_{\Delta_t}/s_l^0)}{1 + \alpha\Gamma(\Delta_e/\delta_l^1, u'_{\Delta_t}/s_l^0)}, \tag{2.78}$$

where the term Γ denotes the ratio between effective strain rate $a_{T,S}$ and the subgrid scale turbulent velocity per filter cutoff length $u^t_{\Delta_e}/\Delta_e$. This term is fitted using the approximation

$$\Gamma\left(\frac{\Delta_e}{\delta_l^1}, \frac{u'_{\Delta_e}}{s_l^0}\right) \approx 0.75 \exp\left[-\frac{1.2}{(u'_{\Delta_e}/s_l^0)^{0.3}}\right]\left(\frac{\Delta_e}{\delta^1}\right)^{2/3}. \tag{2.79}$$

α denotes a model constant, which can be estimated by

$$\alpha = \beta \frac{2\ln(2)}{3c_{ms}(\text{Re}^{1/2} - 1)}, \tag{2.80}$$

where β is a constant in the order of unity and $c_{ms} = 0.28$. [7].

2.7 Network Models for Quasi 1-D Acoustics

Acoustics are a problem of fluid mechanics. Therefore, the tools presented for the simulation of fluid mechanics can in principle be applied to acoustics. As long as they include compressible effects, which is the case in the framework of this thesis, the acoustic phenomena should be reproduced correctly. Nevertheless, in confined geometries, as typical in thermo-acoustic phenomena, typical acoustic length scales are considerably larger than those of classical fluid mechanics: While the acoustic wavelength is usually of the order of magnitude of the size of the domain, e.g. eddies are considerably smaller. For pure acoustics, the influence of the classical fluid mechanic effects is often not taken into account, especially for low Reynolds and Mach numbers. Hence, the numerical simulation of the full equations of fluid mechanics for pure acoustic phenomena is not necessary. Additionally, the numerical schemes used in this context are often dissipative for better convergence, acoustics in contrast requires non-dissipative schemes.
Field methods for acoustics based on the wave equation or other simplifications of the basic equations of fluid dynamics are a common way for the computation of acoustics. Simulation environments like the commercial package Comsol®, or codes like Piano by Deutsches Zentrum für Luft- und Raumfahrt and AVSP by Cerfacs are examples of such approaches. These methods still need additional modeling if flame interaction or acoustic losses have to be taken into account.
Often, the acoustic phenomena can be reduced to 1-D phenomena. In that case, even simpler low order models can be used, so called network models. These are described in the following subsections including the equations for specific elements. For this work the network-tool TaX, based on Matlab Simulink, is mostly used.

2.7.1 Set-Up

The basic idea of network models is to reduce the acoustic system to a network of elements. These elements represent typical effects on acoustic waves as they occur e.g. in ducts or area changes. So, the system is represented as an assembly of simple elements, which all have a certain influence on the acoustic waves and which are connected via nodes. The elements connect two (or sometimes more) of these nodes and affect the acoustic quantities $\hat{p}'/\rho c$ and $\hat{u}'$ or $\hat{\mathfrak{f}}$ and $\hat{\mathfrak{g}}$ at the nodes in a certain way. They represent (mostly) four-ports because they connect two ingoing and two outgoing waves. This connection is realized using a transfer matrix, which quantifies the change in the acoustic quantities at the corresponding nodes of the network [5, 49, 73],

$$\begin{pmatrix} \hat{\mathfrak{f}}_\mathrm{j} \\ \hat{\mathfrak{g}}_\mathrm{j} \end{pmatrix} = \begin{pmatrix} \mathfrak{T}_{11} & \mathfrak{T}_{12} \\ \mathfrak{T}_{21} & \mathfrak{T}_{22} \end{pmatrix} \begin{pmatrix} \hat{\mathfrak{f}}_\mathrm{i} \\ \hat{\mathfrak{g}}_\mathrm{i} \end{pmatrix}. \tag{2.81}$$

This can be transformed into an equation of the following form:

$$\begin{pmatrix} A_{11} & A_{12} & A_{13} & A_{14} \\ A_{21} & A_{22} & A_{23} & A_{24} \end{pmatrix} \begin{pmatrix} \hat{\mathfrak{f}}_\mathrm{i} \\ \hat{\mathfrak{g}}_\mathrm{i} \\ \hat{\mathfrak{f}}_\mathrm{j} \\ \hat{\mathfrak{g}}_\mathrm{j} \end{pmatrix} = 0. \tag{2.82}$$

The transfer matrix can be equivalently transformed into a scattering matrix (see e.g. Appendix of [27]). In the scattering notation, waves leaving the element, $\mathfrak{f}_\mathrm{j}$ and $\mathfrak{g}_\mathrm{i}$, are expressed as functions of waves entering the element, $\mathfrak{f}_\mathrm{i}$ and $\mathfrak{g}_\mathrm{j}$. Therefore, in this notation, transmission and reflection properties can be conveniently seen:

$$\begin{pmatrix} \hat{\mathfrak{f}}_\mathrm{j} \\ \hat{\mathfrak{g}}_\mathrm{i} \end{pmatrix} = \begin{pmatrix} \mathfrak{S}_{11} & \mathfrak{S}_{12} \\ \mathfrak{S}_{21} & \mathfrak{S}_{22} \end{pmatrix} \begin{pmatrix} \hat{\mathfrak{f}}_\mathrm{i} \\ \hat{\mathfrak{g}}_\mathrm{j} \end{pmatrix}. \tag{2.83}$$

Boundary conditions at the ends of the network close the system. In this way, a linear algebraic system of equations can be set up,

$$\begin{pmatrix} A_{11} & A_{12} & 0 & 0 & \cdots & 0 & 0 \\ A_{21} & A_{22} & A_{23} & A_{24} & \cdots & 0 & 0 \\ A_{31} & A_{32} & A_{33} & A_{34} & \cdots & 0 & 0 \\ 0 & 0 & A_{43} & A_{44} & \cdots & 0 & 0 \\ \vdots & \vdots & \vdots & \vdots & \ddots & \vdots & \vdots \\ 0 & 0 & 0 & 0 & \cdots & A_{\mathrm{n,n-1}} & A_{\mathrm{n,n}} \end{pmatrix} \begin{pmatrix} \hat{\mathfrak{f}}_1 \\ \hat{\mathfrak{g}}_1 \\ \hat{\mathfrak{f}}_2 \\ \hat{\mathfrak{g}}_2 \\ \vdots \\ \hat{\mathfrak{f}}_\mathrm{n} \\ \hat{\mathfrak{g}}_\mathrm{n} \end{pmatrix} = 0. \tag{2.84}$$

2.7.2 Examples of Elements

Transfer Matrix of a Duct The transfer matrix of a simple duct with mean flow can be described by the phase shift of the characteristic waves. A wave $\mathfrak{f}$ traveling downstream and a wave $\mathfrak{g}$ traveling upstream in a mean flow of velocity $\bar{u}$ in a duct of length l with constant cross section and constant temperature are affected in the following way:

$$\begin{pmatrix} e^{-ik^+l} & 0 & -1 & 0 \\ 0 & e^{ik^-l} & 0 & -1 \end{pmatrix} \begin{pmatrix} \hat{\mathfrak{f}}_\mathrm{i} \\ \hat{\mathfrak{g}}_\mathrm{i} \\ \hat{\mathfrak{f}}_\mathrm{j} \\ \hat{\mathfrak{g}}_\mathrm{j} \end{pmatrix} = 0. \tag{2.85}$$

The wave-numbers are $k^+ = \omega/(c+\bar{u})$ and $k^- = \omega/(c-\bar{u})$ [44].

Transfer Matrix of a compact Area change We consider an area change from a cross section S_i upstream to S_j downstream of the element. The element is considered to be compact, i.e. much shorter than the wave length of the acoustic waves. Two equations, the Bernoulli and the mass conservation are used: according to [108] the unsteady Bernoulli equation can be written:

$$\frac{\partial}{\partial x_\mathrm{i}}\left(\frac{\partial \phi}{\partial t} + \frac{u^2}{2} + \frac{\gamma}{\gamma-1}\frac{p}{\rho}\right) = 0. \tag{2.86}$$

This equation is integrated over the length of the element from x_i to x_j. In a compact element density can be assumed to be constant. Hence, the term for the velocity potential ϕ can be written:

$$\frac{\partial}{\partial t}\int_{x_i}^{x_j} \frac{\partial \phi}{\partial \xi} d\xi = \frac{\partial}{\partial t}\int_{x_i}^{x_j} u\, d\xi \approx \frac{\partial}{\partial t} u_\mathrm{i} \int_{x_i}^{x_j} \frac{A_\mathrm{i}}{A(\xi)} d\xi. \tag{2.87}$$

Defining now an extended length

$$l_\mathrm{ext} = \int_{x_i}^{x_j} \frac{A_\mathrm{i}}{A(\xi)} d\xi, \tag{2.88}$$

the expression for the velocity for harmonic perturbations becomes :

$$\frac{\partial}{\partial t} u_\mathrm{i} \int_{x_i}^{x_j} \frac{A_\mathrm{i}}{A(\xi)} d\xi = i\omega l_\mathrm{ext} u'_\mathrm{i} \tag{2.89}$$

For the spatial integration, the second and the third term in equation 2.86 can be evaluated at the borders x_i and x_j. Combined with the last equation, one obtains:

$$i\omega l_\mathrm{ext} u_\mathrm{i}' + \frac{u(x_\mathrm{j})^2}{2} + \frac{p(x_\mathrm{j})}{\rho} - \frac{u(x_\mathrm{i})^2}{2} - \frac{p(x_\mathrm{i})}{\rho} = 0. \tag{2.90}$$

A loss coefficient ζ is introduced to account for acoustic losses and the equation is linearized. Dropping terms of first order in Mach number $\mathcal{O}(\mathrm{M})$ and second order in Helmholtz number $\mathcal{O}(\mathrm{k}l)^2$ and dividing by c results in:

$$\frac{p'(x_\mathrm{j})}{\rho c} = \frac{p'(x_\mathrm{i})}{\rho c} - ikl_\mathrm{ext} u_\mathrm{i}' - \zeta \mathrm{M} u_\mathrm{i}'. \tag{2.91}$$

The mass conservation for the element of volume V, inlet area A_i and outlet area A_j is:

$$\frac{d}{dt}\int_{x_i}^{x_j} \rho(\xi) A(\xi)\, d\xi + \rho(x_\mathrm{i}) u(x_\mathrm{i}) A_\mathrm{i} - \rho(x_\mathrm{j}) u(x_\mathrm{j}) A_\mathrm{j} = 0. \tag{2.92}$$

Introducing $A_{red} = \int_{x_\mathrm{i}}^{x_\mathrm{j}} \frac{A(\xi)}{A_\mathrm{j}}$, linearization and the assumption that ρ' is constant leads to:

$$ikl_\mathrm{red} A_\mathrm{j} \frac{p'(x_\mathrm{j})}{\rho c} + u'(x_\mathrm{j}) + \mathrm{M}\frac{p'(x_\mathrm{j})}{\rho c} A_\mathrm{j} - u'(x_\mathrm{i}) + \mathrm{M}\frac{p'(x_\mathrm{i})}{\rho c} A_\mathrm{i} = \mathcal{O}(\mathrm{k}l)^2. \tag{2.93}$$

Neglecting terms of $\mathcal{O}(\mathrm{M})$ and $\mathcal{O}(\mathrm{k}l)^2$ results in:

$$u_\mathrm{j}' A_\mathrm{j} = u_\mathrm{i}' A_\mathrm{i} + ikl_\mathrm{red} A_\mathrm{j} \frac{p_\mathrm{j}'}{\rho c}. \tag{2.94}$$

Equations 2.91 and 2.94 form the transfer matrix for the area change. It is written here in p'-u' notation but can be equivalentely transferred into $\mathfrak{f}$-$\mathfrak{g}$ notation:

$$\begin{pmatrix} 1 & -ikl_\mathrm{eff} - \zeta\mathrm{M} & -1 & 0 \\ ikl_\mathrm{red} & \frac{A_\mathrm{i}}{A_\mathrm{j}} & 0 & -1 \end{pmatrix} \begin{pmatrix} \hat{u}_\mathrm{i}' \\ \hat{p}_\mathrm{i}/(\rho c) \\ \hat{u}_\mathrm{j}' \\ \hat{p}_\mathrm{j}/(\rho c) \end{pmatrix} = 0. \tag{2.95}$$

The quantity l_eff has been introduced, because an end correction $l_\mathrm{ec,i/j}$ is usually necessary. This end correction accounts for the additional “virtual” length which originates from the piston-like movement of the gas in the volume:

$$l_\mathrm{eff} = l_\mathrm{ext} + l_\mathrm{ec,i} + l_\mathrm{ec,j}. \tag{2.96}$$

Transfer Matrix of a Flame The dynamic response of a flame to a flow perturbation is often characterized using a so called Flame Transfer Function (FTF) $F(\omega)$. This complex function relates the relative heat release fluctuation to the relative velocity fluctuation:

$$F(\omega) = \frac{\dot{Q}'/\bar{\dot{Q}}}{u'/\bar{u}}. \tag{2.97}$$

In this way, the response of the flame to acoustic velocity fluctuations can be expressed. The transfer matrix of a flame can be derived using the linearized Rankine Huguenot equations (see e.g. [44]). The basic equations are

$$p'_\mathrm{i} - p'_\mathrm{j} - \bar{\rho}_\mathrm{i}\bar{u}_\mathrm{i}^2\left(\frac{T_\mathrm{j}}{T_\mathrm{i}} - 1\right)\left(\frac{u'_\mathrm{i}}{\bar{u}_\mathrm{i}} + \frac{\dot{Q}'}{\bar{\dot{Q}}}\right) = 0, \tag{2.98}$$

$$u'_\mathrm{i} - u'_\mathrm{j} + \left(\frac{T_\mathrm{j}}{T_\mathrm{i}} - 1\right)\bar{u}_\mathrm{i}\left(\frac{\dot{Q}'}{\bar{\dot{Q}}} - \frac{p'_\mathrm{i}}{\bar{p}_\mathrm{i}}\right) = 0, \tag{2.99}$$

where i denotes the cold and j the hot side. Using the FTF the heat release fluctuation can be expressed by a velocity fluctuation. For flexibility reasons the velocity fluctuations used for the FTF will be taken from a different location k. Therefore, this element will be a 6-port instead of a 4-port. Using

$$\bar{u} = Mc, \tag{2.100}$$

$$c^2 = \kappa\frac{p}{\rho}, \tag{2.101}$$

$$n = \frac{T_\mathrm{j}}{T_\mathrm{i}} - 1, \tag{2.102}$$

the transfer matrix is written as

$$\begin{pmatrix} 1 - nM_\mathrm{i} & 1 + nM_\mathrm{i} & -\frac{\rho_\mathrm{j}c_\mathrm{j}}{\rho_\mathrm{i}c_\mathrm{i}} & -\frac{\rho_\mathrm{j}c_\mathrm{j}}{\rho_\mathrm{i}c_\mathrm{i}} & -nM_\mathrm{i}\frac{M_\mathrm{i}c_\mathrm{i}}{M_\mathrm{k}c_\mathrm{k}}F(\omega) & nM_\mathrm{i}\frac{M_\mathrm{i}c_\mathrm{i}}{M_\mathrm{k}c_\mathrm{k}}F(\omega) \\ 1 - nM_\mathrm{i}\kappa & -1 - nM_\mathrm{i}\kappa & -1 & +1 & n\frac{M_\mathrm{i}c_\mathrm{i}}{M_\mathrm{k}c_\mathrm{k}}F(\omega) & -n\frac{M_\mathrm{i}c_\mathrm{i}}{M_\mathrm{k}c_\mathrm{k}}F(\omega) \end{pmatrix} \begin{pmatrix} \hat{\mathfrak{f}}_\mathrm{i} \\ \hat{\mathfrak{g}}_\mathrm{i} \\ \hat{\mathfrak{f}}_\mathrm{j} \\ \hat{\mathfrak{g}}_\mathrm{j} \\ \hat{\mathfrak{f}}_\mathrm{k} \\ \hat{\mathfrak{g}}_\mathrm{k} \end{pmatrix} = 0. \tag{2.103}$$

Stokes Layer Dominated Duct In thin ducts, the viscous sublayer can have significant influence on the acoustic behavior, as it leads to acoustic losses. For single ducts, a variety of models has been proposed. Early theories have been developed by Helmholtz [25] and Kirchhoff who accounted for thermal effects [38, 106]. Here, a Kirchhoff model is used, as proposed by Noiray for this application (e.g. [60]) inspired by Melling [55] in a simplified version for short lengths l,

$$\begin{pmatrix} e^{-i(k^{+}+\zeta_{\mathrm{s}})l} & 0 & -1 & 0 \\ 0 & e^{-i(k^{-}+\zeta_{\mathrm{s}})l} & 0 & -1 \end{pmatrix} \begin{pmatrix} \hat{\mathfrak{f}}_{\mathrm{i}} \\ \hat{\mathfrak{g}}_{\mathrm{i}} \\ \hat{\mathfrak{f}}_{\mathrm{j}} \\ \hat{\mathfrak{g}}_{\mathrm{j}} \end{pmatrix} = 0. \tag{2.104}$$

The damping coefficient ζ_{s} takes the viscous losses into account:

$$\zeta_{\mathrm{s}} = (1+i)\frac{\sqrt{2\omega\nu}}{2r_{\mathrm{h}}c}\left(1+\frac{\gamma-1}{Pr^{0.5}}\right). \tag{2.105}$$

More sophisticated models have been developed by various authors. Tijdeman [106] gives an overview.

Boundary Conditions The boundary conditions for network models are formed by a 2-port. Introducing a reflection coefficient $\hat{\mathscr{R}}$ defined as the ratio between the complex amplitudes of the wave entering the domain and the one leaving the domain, an inlet can be expressed by

$$\begin{pmatrix} -1 & \hat{\mathscr{R}} \end{pmatrix} \begin{pmatrix} \hat{\mathfrak{f}}_{\mathrm{i}} \\ \hat{\mathfrak{g}}_{\mathrm{i}} \end{pmatrix} = 0 \tag{2.106}$$

and an outlet by

$$\begin{pmatrix} \hat{\mathscr{R}} & -1 \end{pmatrix} \begin{pmatrix} \hat{\mathfrak{f}}_{\mathrm{i}} \\ \hat{\mathfrak{g}}_{\mathrm{i}} \end{pmatrix} = 0. \tag{2.107}$$

Unknown Elements The analytical derivation of the transfer behavior of elements is not always possible. Nevertheless, identification of such elements from experiments or numerical simulations often is possible and has been performed by various authors [16, 27]. Common methods in this context are the determination of flame transfer functions or transfer matrices. For the latter, usually an excitation is imposed on the experimental or numerical set-up for the element subsequently on both sides, and the system response is recorded. In general, the system is considered as a black box whose response or responses to one or more input signals are detected. Section 2.8 gives a brief introduction to correlation based methods of system identification, which then can be used to calculate the system behavior.

2.8 System Identification

In the context of this work, system identification is applied to identify the complex ratio $F(\omega)$ between acoustic signal and response in the frequency domain. These techniques are well known in the field of communication technology [80]. A method based on the Unit Impulse Response (UIR) and the Wiener-Hopf equation is applied here. In contrast to the Fourier transformation method, this method provides data not only at discrete points in the frequency spectrum, but continuously from the lower frequency limit $(1/(N\cdot\Delta t))$ to the higher frequency limit$(1/\Delta t)$ by an approximating function. Examples of the usage of this method can be found in [16, 22, 23, 28, 47, 48, 80]. The basic problem in this method is the identification of the UIR vector. The UIR vector h of a length L relates a time discrete signal,

$$\vec{s} = [s_1, s_2, ..., s_\mathrm{N}], \tag{2.108}$$

and a time discrete response,

$$\vec{r} = [r_1, r_2, ..., r_\mathrm{N}], \tag{2.109}$$

both over N time steps in the following way [80]:

$$r_\mathrm{i} = \sum_{\mathrm{k}=0}^{\infty} h_\mathrm{k} s_\mathrm{i\text{-}k} \quad \text{for } i = L, ..., N, \tag{2.110}$$

for $N \to \infty$; and approximately $(\tilde{\ })$

$$\tilde{r}_\mathrm{i} = \sum_{\mathrm{k}=0}^{\mathrm{L}} \tilde{h}_\mathrm{k} s_\mathrm{i\text{-}k} \quad \text{for } i = L, ..., N, \tag{2.111}$$

for finite N and L. For the calculation of the UIR vector, the Wiener-Hopf equation is used:

$$\Gamma \vec{h} = \vec{c}, \tag{2.112}$$

where Γ is the auto-correlation matrix and $\vec{c}$ the cross-correlation vector. Using now the definitions of auto-correlation and cross-correlation for finite N and $M = N - L + 1$ in this context,

$$\tilde{c}_{\mathrm{i}} = \frac{1}{M} \sum_{\mathrm{l=L}}^{N} s_{\mathrm{l\text{-}i}} r_{\mathrm{l}} \quad \text{for } i = 0, \ldots, L, \tag{2.113}$$

$$\tilde{\Gamma}_{\mathrm{ij}} = \frac{1}{M} \sum_{\mathrm{l=L}}^{\mathrm{N}} s_{\mathrm{l\text{-}i}} s_{\mathrm{l\text{-}j}} \quad \text{for } i, j = 0, \ldots, L, \tag{2.114}$$

the UIR-vector can be calculated using the inverted Wiener-Hopf equation,

$$\vec{\tilde{h}} = \tilde{\Gamma}^{-1} \vec{\tilde{c}}, \tag{2.115}$$

using standard mathematical methods. The last step is now the calculation of the transfer function $F(\omega)$,

$$F(\omega) = \frac{\hat{r}(\omega)}{\hat{s}(\omega)}, \tag{2.116}$$

where $\hat{r}$ is the response and $\hat{s}$ is the signal in frequency domain. This is done using z-transformation,

$$\mathscr{Z}(\tilde{h}) = \sum_{\mathrm{k=0}}^{\mathrm{L}} \tilde{h}(k) z^{-k}, \tag{2.117}$$

and with $z = e^{i\omega\Delta t}$ the approximate transfer function can be calculated:

$$\tilde{F}(\omega) = \mathscr{Z}(\tilde{h}) = \sum_{\mathrm{k=0}}^{\mathrm{L}} \tilde{h}(i) z^{-i\omega\Delta t k}. \tag{2.118}$$

In contrast to FFT methods, this method can compensate noise to some extent, because correlation is used. In this case, though, it is required that noise and signal are uncorrelated.

3 Thermo-Acoustic Stability

Thermo-acoustic instabilities evolve due to a self amplifying interaction between flow field and heat release. One of the earliest observations of a thermo-acoustic instability is the Rijke tube, described by P. L. Rijke in 1859 [88]. Rijke did observe the phenomenon, however, he could not offer the right explanation. In 1878 Lord Rayleigh explained this phenomenon [85] and from this explanation the Rayleigh criterion can be formulated: A thermo-acoustic system may be unstable if more heat is released in the moment of higher pressure. This can be formulated for $\dot{Q}'(t)$ being the acoustically originated heat release fluctuation and $p'(t)$ being the acoustic pressure fluctuation:

$$\int_{t_0}^{t_0+2\pi/\omega} \dot{Q}'(t)p'(t)dt > 0. \tag{3.1}$$

In a more general formulation, the left hand side of equation 3.1 must not only be greater than 0 but greater than the acoustic losses in the system. The equation implies that a fluctuation of the heat release $\dot{Q}'$ depending on the fluctuations of the flow field is a requirement for the occurrence of thermo-acoustic instabilities [3]. These fluctuations of the heat release can be caused by the flow field via different mechanisms [44]:

- Direct influence on the flame or heat transfer [11, 85],
- Fluctuations of the fuel supply [37, 52, 98],
- Entropy waves [78],
- Periodic vortex shedding [71],
- Shock waves [54].

The heat release fluctuation then causes a fluctuation in thermal expansion which again produces an acoustic wave, which then can once again cause heat release fluctuations and create a self excited instability. From equation 3.1 it can be deduced how important the phase between pressure fluctuation and heat release fluctuation is for thermo-acoustic effects. Therefore, methods for the prediction of thermo-acoustic instabilities rely essentially on the correct prediction of the time relations between those two fluctuations. The underlying mechanism for the flow-field heat-release coupling is the key to the prediction of thermo-acoustic instability. Pankiewitz [66] illustrates the common instability mechanisms as shown in figure 3.1

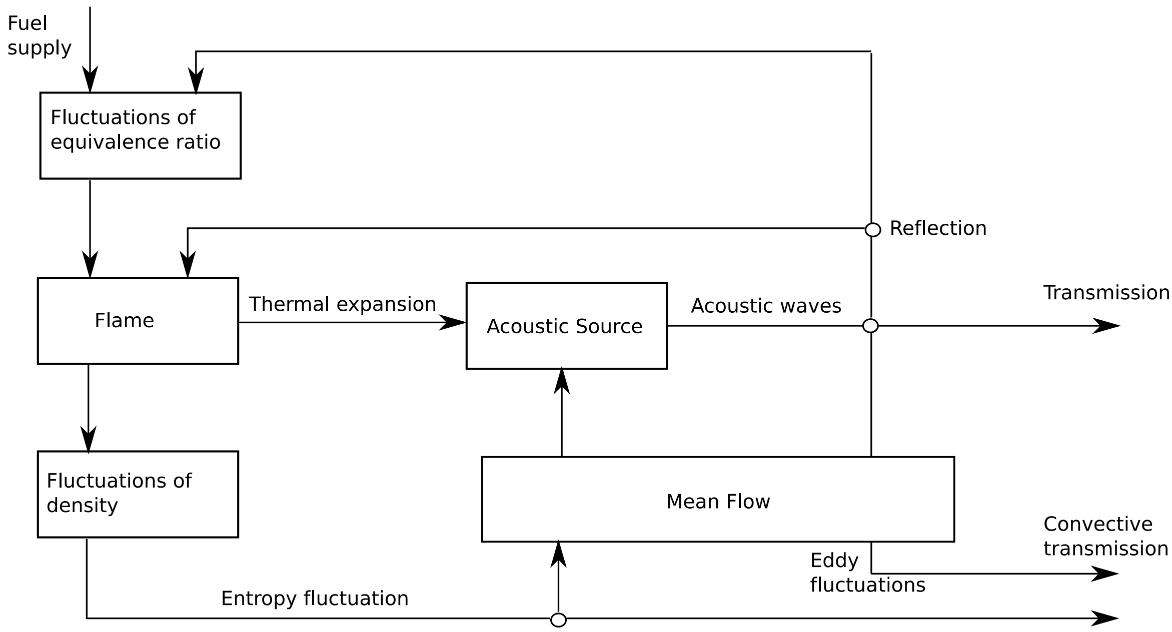

Figure 3.1: Main mechanisms leading to thermo-acoustic instability, from [66].

3.1 Established Methods for Thermo-Acoustic Stability Analysis

In the field of the prediction of thermo-acoustic stability, several different methods of modeling and different ways of evaluation of stability can be distinguished. Figure 3.2 shows possible combinations of methods for modeling and prediction.

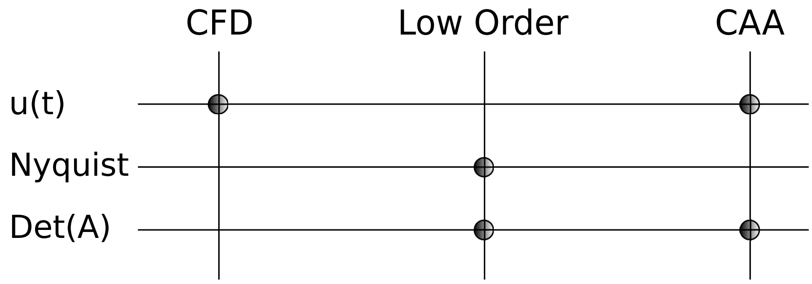

Figure 3.2: Matrix of different methods of modeling (columns) and different methods for the determination of the stability (lines). Dots show the possibility of combination of methods for modeling and prediction.

In the following, the different methods of prediction (rows in figure 3.2) are discussed.

3.1.1 Transient Calculation

In the time domain, a common approach is to model the system, impose an initial perturbation (if required), and run the simulation until the growth of a mode can be observed [24, 68, 101, 114]. The modeling can be done using either CAA or CFD methods. The big advantage of this method is the possibility of using it with methods of a low level of modeling, e.g. CFD. This results in a good reproduction of different interactions, e.g. between turbulence and acoustics. Major disadvantages arise from the high computational effort for one transient solver run especially in the case of CFD. Additionally, special solver requirements for the calculation of acoustics can be present concerning numerical damping and stability as well as boundary conditions. Primarily unstable modes or modes with low damping can be found using this method, and only the most unstable mode will be dominant. Therefore, this method permits stability to be evaluated, but does not offer a comprehensive overview over the eigenfrequencies.
The range of frequencies covered by transient calculation depends on the time step for the high frequency limit and the simulated physical time for the low frequency limit.

3.1.2 Nyquist Methods

Nyquist Methods (or Open Loop Gain Methods) work in the frequency domain and are a graphical tool to evaluate stability which only requires information from real (and not imaginary) frequencies. They are well known from control theory and serve to determine both stable and unstable eigenmodes. Due to their crucial importance for this work, they are described in detail in the next section (section 3.2).

3.1.3 Determination of Eigenvalues

This method is widely used with low order acoustic models, e.g. network models, or with CAA applications. The determination of eigenvalues usually requires a formulation in the frequency domain and has been used frequently to determine the eigenfrequencies and eigenmodes of thermo-acoustic systems [66]. It will be demonstrated here using network models. Let us consider a system matrix:

$$\begin{pmatrix} A_{11} & A_{12} & 0 & 0 & \cdots & 0 & 0 \\ A_{21} & A_{22} & A_{23} & A_{24} & \cdots & 0 & 0 \\ A_{31} & A_{32} & A_{33} & A_{34} & \cdots & 0 & 0 \\ 0 & 0 & A_{43} & A_{44} & \cdots & 0 & 0 \\ \vdots & \vdots & \vdots & \vdots & \ddots & \vdots & \vdots \\ 0 & 0 & 0 & 0 & \cdots & A_{n,n-1} & A_{n,n} \end{pmatrix} \begin{pmatrix} \hat{\mathfrak{f}}_1 \\ \hat{\mathfrak{g}}_1 \\ \hat{\mathfrak{f}}_2 \\ \hat{\mathfrak{g}}_2 \\ \vdots \\ \hat{\mathfrak{f}}_n \\ \hat{\mathfrak{g}}_n \end{pmatrix} = 0. \tag{3.2}$$

This is a linear system of equations. Consequently, if the system has full rank, there is only one solution. In the case of a homogeneous system of equations, this solution is 0 for all unknowns. However, the coefficients A_{ij} of this system depend on the frequency. Hence, it is possible that for certain frequencies the system does not have full rank. In this case, the determinant of the system matrix is 0 and the system has one (or more) degrees of freedom. One (or more) unknowns can now be arbitrarily set, i.e. the amplitude of the oscillation can be chosen.

The corresponding frequency is an eigenfrequency and the solution an eigenmode. The eigenfrequency is in general complex, $\omega \in \mathbb{C}$. Hence, in order to obtain the eigenfrequencies, one can try to find the roots of the determinant of the system matrix. Obviously, this can only be done if all coefficients are known as a function of the complex frequency. But this is not necessarily the case for experimentally or numerically determined coefficients. Another drawback of this method is the low speed of the iterative algorithms often used for finding the roots and the uncertainty as to whether the algorithm has succeeded in finding all roots. The numerical effort for the determination of eigenvalues depends on the size of the system matrix and in this context on the complexity of the modeling approach used. Low order models are much quicker in this context than e.g. acoustic FE calculations.

3.2 Stability Analysis using the Open Loop Gain

3.2.1 Basic Concepts in Control Theory

Control theory is a wide and complex subject and discussing it in detail would go beyond the scope of this thesis. This section shall give a brief overview over some important aspects of control theory. For further details the interested reader is referred to works such as [31] or [20] which also serve as the basis for this section. In control theory a system can be described by transfer functions which model the change of the quantity which is subject to the control. These transfer functions are usually defined in the Laplace transformed form of the signal in the time domain,

$$F(s) = \mathfrak{L}(f(t)) = \int_{-\infty}^{\infty} e^{-st} f(t) dt, \tag{3.3}$$

where $s = \sigma + i\omega$. Some important properties of the Laplace transformation are:

$$a \cdot f(t) + b \cdot g(t) \rightarrow a \cdot F(s) + b \cdot G(s), \tag{3.4}$$

$$(f * g)(t) \rightarrow F(s) \cdot G(s), \tag{3.5}$$

$$f'(t) \rightarrow s \cdot F(s), \tag{3.6}$$

where $*$ denotes a convolution. A simple system for control theory representing a closed loop is shown in fig 3.3.

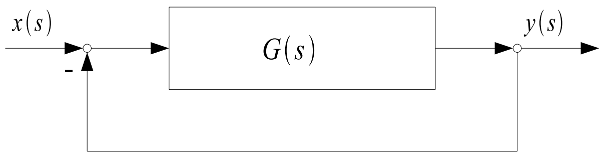

Figure 3.3: Sketch of a closed control loop.

The Closed Loop Transfer Function (CLTF), $H(s)$, of this system can be calculated easily and has the form

$$H(s) = \frac{y(s)}{x(s)} = \frac{G(s)}{1 + G(s)}. \tag{3.7}$$

This system becomes unstable, i.e. infinite, when $1 + G(s) = 0$ or $G(s) = -1$. In classical control theory, for typical systems the behavior $(G(s))$ can be described by polynomial functions in the Laplace domain, i.e. P, D, I elements. For these systems, criteria like the Routh Hurwitz criterion impose conditions for the coefficients of the polynomials, which allow the system to be examined for stability. Finding the roots of the CLTF for more complex systems may prove to be nontrivial. Therefore, different methods have been developed, e.g. methods relying on Bode plots and Nyquist curves. The latter are an important subject of this thesis and therefore shall be explained here in more detail. The Nyquist stability criterion refers to the open loop transfer function (OLTF). This means that the stability of the closed loop is evaluated by regarding the open loop. The corresponding open loop for figure 3.3 is represented in figure 3.4.

The OLTF, $F(s)$, of this system is then defined:

$$F(s) = \frac{y(s)}{x(s)} = G(s). \tag{3.8}$$

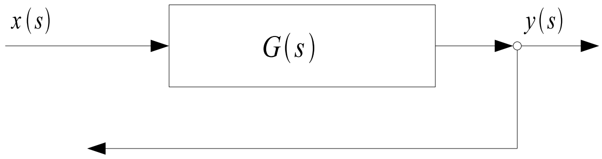

Figure 3.4: Sketch of an open control loop.

By comparing the CLTF and the OLTF, the point $F(s) = -1$ can be identified as the location of the roots of the closed loop. The Nyquist stability criterion refers to this point. The frequency response locus ($F(s)$) is plotted in the complex plane for real frequencies and the location of the point -1 is compared to this curve. Depending on the properties of $F(s)$ different formulations of the Nyquist criterion can be applied:

1. The specialized Nyquist criterion:
   Provided that

   - all roots of the OLTF $F(s)$ have a negative real part and
   - $\lim\limits_{\omega\to\infty} F(i\omega) = 0$,

   the system is considered asymptotically stable if the response locus does not encircle the critical point -1 [20].

2. The general Nyquist criterion:
   The following restrictions have to be considered:

   - The OLTF does not exhibit roots on the imaginary axis ($s = i\omega$)
   - $\lim\limits_{\omega\to\infty} F(i\omega) = 0$

   Defining now P as the number of unstable roots of the OLTF, N as the number of unstable roots of the CLTP and U as the number of encirclements of the critical point -1, the system is stable if $U = P$ [20].

3.2.2 Application to Thermo-Acoustic Cases

Historically, Baade [3] described an evaluation of the thermo-acoustic stability based on phase and amplitude curves of the impedances of the system, i.e. a

Bode Diagram. Deuker [11] also proposed the use of such a Nyquist-like criterion on a Bode diagram for thermo-acoustic cases and network models. However, these stability criteria are both too simplified because they only consider the gain at phase 0° (which corresponds to 180° in this case due to the minus convention in the feedback). Baade compares the phase angle of 0° with the location of the acoustic eigenfrequencies of the chamber. Deuker considers the gain at the frequency of the 0° phase. If the gain is equal or greater than 1, the oscillation is considered unstable. This corresponds to the "Barkhausen"-Stability criterion, which "*is simple, intuitive, and wrong*" [53]. The explanation for this is given in subsection 3.2.3.
Polifke et al. [79] have proposed the introduction of a so called diagnostic two port, or diagnostic dummy, as an additional element for the effective implementation of an open control loop into network models (see figures 3.5 and 3.6). They also introduced the generalized Nyquist criterion (see 3.2.3). Analogously to [31] or [56], they discuss the Nyquist criterion with respect to a conformal mapping and also consider Bode rules.

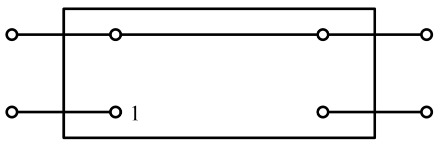

Figure 3.5: The diagnostic two port.

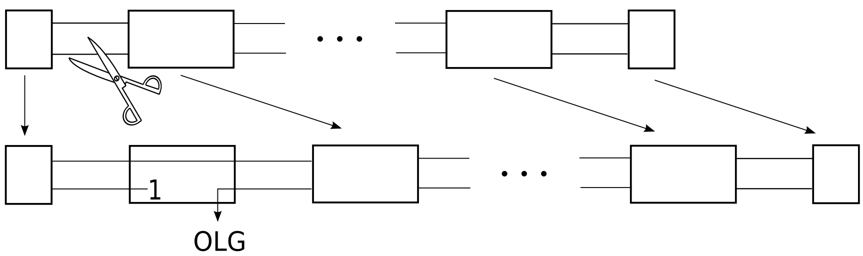

Figure 3.6: A network model opened using the diagnostic two port.

Sattelmayer and Polifke [93] performed a stability analysis for a combustion chamber and discovered substantial shortcomings and mispredictions when the Nyquist criterion is wrongly applied in the form of the "Barkhausen" stability criterion. Later [94], they validated the generalized Nyquist criterion.

They also introduced a method to determine the growth rates from polynomial interpolation. Kopitz and Polifke [46] proposed a simplified method to determine the growth rate from the scaled minimum distance of the Open Loop Gain Curve and the critical point. For more details on this, please refer to the next section (3.2.3). A summary of this is given by Kopitz [44, 46].

It would be straightforward to apply the conventional Nyquist criterion to thermo-acoustic cases, but there are some particularities of such systems which require modifications on the criterion. These are described in the following section:.
As described in section 2.7 previously, most thermo-acoustic systems can be described in terms of low order network models (see fig 3.7).

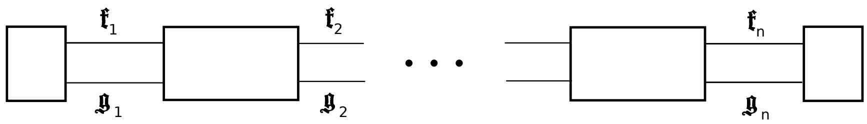

Figure 3.7: Sketch of a network model.

The result of this description is an equation of the form

$$\begin{pmatrix} A_{1,1}(\omega) & \cdots & A_{1,2n}(\omega) \\ \vdots & \ddots & \vdots \\ A_{2n,1}(\omega) & \cdots & A_{2n,2n}(\omega) \end{pmatrix} \cdot \begin{pmatrix} \hat{\mathfrak{f}}_1 \\ \vdots \\ \hat{\mathfrak{g}}_n \end{pmatrix} = 0. \tag{3.9}$$

This concept corresponds to a classical closed control loop as shown in figure 3.8 for a Fourier transformed signal. The application of a Fourier transformation instead of a Laplace transformation does not have any influence because of the similar properties of both transformations.

The transfer behavior can be expressed by

$$\frac{y(\omega)}{x(\omega)} = \frac{G(\omega)}{G(\omega)+1}. \tag{3.10}$$

Traditional concepts intend to find the eigenvalues of equation 3.9 in order to determine the eigenfrequencies. This iterative procedure, however, is only

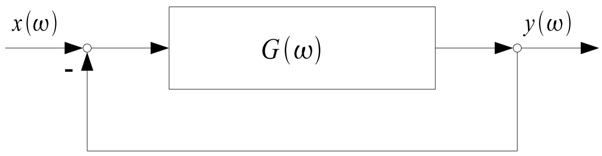

Figure 3.8: Sketch of a closed control loop in the frequency domain.

possible if all components of the matrix can be described in the complex wave plane. This is the case for most analytical descriptions, but in the case of experimentally determined transfer functions the response is only known for real frequencies. The Open Loop Gain (OLG) method is a tool adapted from control theory which only requires real frequency input to perform a stability analysis. This method is also named the Nyquist method here due to its similarities to the classical Nyquist criterion. As the name already implies, the feedback loop is opened for this method. This is demonstrated in figure 3.9. On one of the open ends generated this way, a unity amplitude is applied, while on the other end the complex frequency response is recorded.

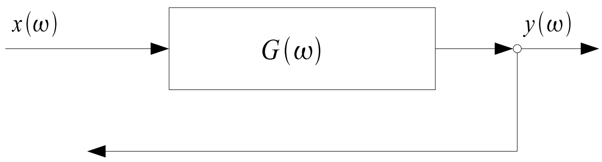

Figure 3.9: Sketch of an open control loop.

By opening the feedback of the system for the OLTF, the originally homogeneous system now becomes an inhomogeneous system with two additional degrees of freedom which can be solved for each frequency. But, compared to classical systems known from control theory, there are major differences.
First, typical acoustic systems can not be described by polynomials, but rather by trigonometric functions or complex exponential functions. Thus, these systems have an infinite amount of poles. Hence, the criteria above are not applicable, because the location of an infinite amount of roots would be required.
Additionally, one of the basic requirements for the application of the Nyquist criterion, $\lim_{\omega \to \infty} F(i\omega) = 0$, is not fulfilled for most acoustic systems.
Therefore, in the following section, a different "derivation" of the Nyquist criterion is presented.

3.2.3 Generalized Nyquist Criterion

3.2.3.1 Mathematical Justification

As mentioned in the paragraph above, different requirements for the Nyquist criterion are not fulfilled by acoustic systems. Therefore, the application of the Nyquist criterion is not possible in its original form. Polifke et al. [79] as well as Sattelmayer and Polifke [93, 94] have proposed a different formulation of the Nyquist criterion for the thermo-acoustic case.

As described in [31, 56] and applied by Polifke et al. [79] the open loop gain is considered a conformal mapping of the complex frequency domain. A mapping $f : U \rightarrow \mathbb{C}$ for U being an open subset of the complex plane $\mathbb{C}$ is defined conformal if and only if $f' \neq 0$ on U. Conformal mapping locally preserves the angle and therefore the handedness. The mapping performed by the OLTF projects all roots of equation 3.10 on the point -1. Calculating the OLTF-curve (Nyquist curve) for real frequencies means projecting the positive real axis on the Nyquist curve.

- Hence, if a root is located on the upper half plane (and therefore is stable) which is to the left of the real axis (looking in the positive direction) it must also be to the left of the OLTF curve (looking in the direction of the increasing frequency) and vice versa.

This is shown in figure 3.10. Limitations to this generalized Nyquist criterion are discussed in subsection 5.

3.2.3.2 Prediction of Eigenfrequencies and Growth Rates

The classical Nyquist criterion does not involve the prediction of the eigenfrequency or the growth rate, it only permits stability to be determined. In order to determine the eigenfrequencies from an open loop curve, Sattelmayer and Polifke [93,94] propose to seek the minimum of the distance between the open loop curve and the critical point -1 and define the frequency of this point as the eigenfrequency. This is done in analogy to the frequency domain, where

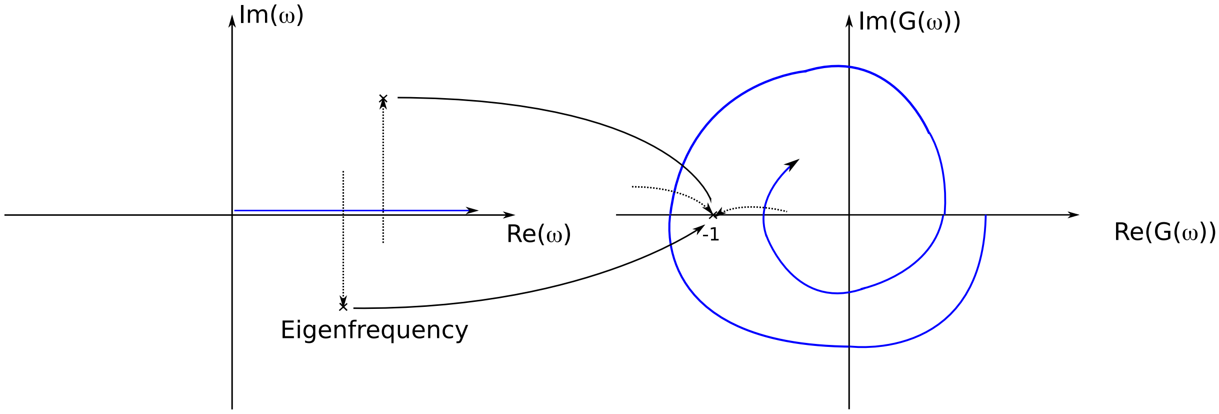

Figure 3.10: Visualisation of the mapping of the Open Loop.

the distance between the real axis and the eigenfrequency is minimal just at the frequency corresponding to the real part of the eigenfrequency. If the distance between the real axis and the eigenfrequency is large, i.e. the growth rate has a large magnitude, this minimum of the distance is less pronounced and therefore much more sensitive to errors (see figure 3.11). Sources of such errors are discussed in section 5. Hence, the prediction of eigenfrequencies with the Nyquist method is losing precision for highly stable or highly unstable eigenfrequencies.

For the determination of the growth rate, Sattelmayer and Polifke propose a polynomial fit of the OLTF. If this fit is accurate in the real direction it is also accurate in the complex direction. This follows from the identity theorem [84]. Therefore, it is possible to use the polynomial approximation for finding the complex eigenfrequency. Two major assumptions have been made for this approach:

- The open loop mapping is conformal in the vicinity of the corresponding frequency and the corresponding eigenfrequency.
- The mapping is distance conserving, ($\partial f / \partial z = const$).

The first item permits location of the roots to be concluded from the Nyquist curve. The second item is necessary for the assumption that the (real) eigenfrequency which is at the shortest distance from the root on the complex fre-

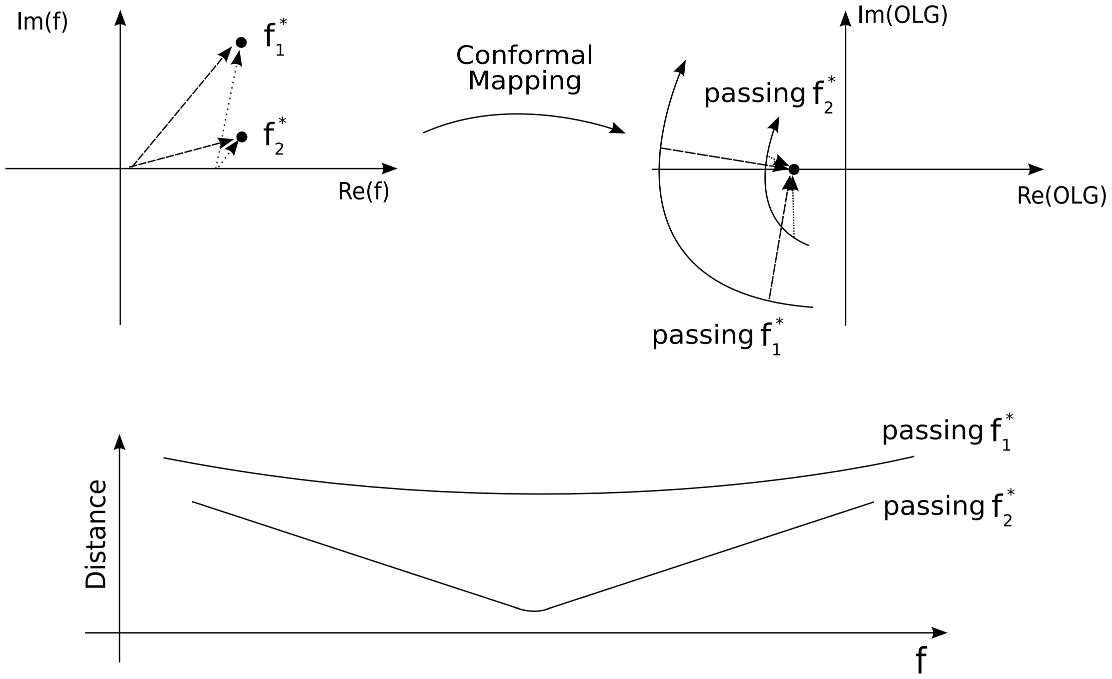

Figure 3.11: Influence of the growth-rate of the eigenfrequencies, f_1^* for high growth rate, f_2^* for low growth rate (above). Schematic evolution of the distance for the two distances (below).

quency plane also is at the shortest distance on the open loop curve. A conformal mapping is not necessarily distance conserving. This can for example be seen on Mercator-projected (conformal) geographic maps where the east-west distances are massively stretched close to the geographic poles (see figure 3.12). Hence, the minimal distance between the open loop curve and the criti-

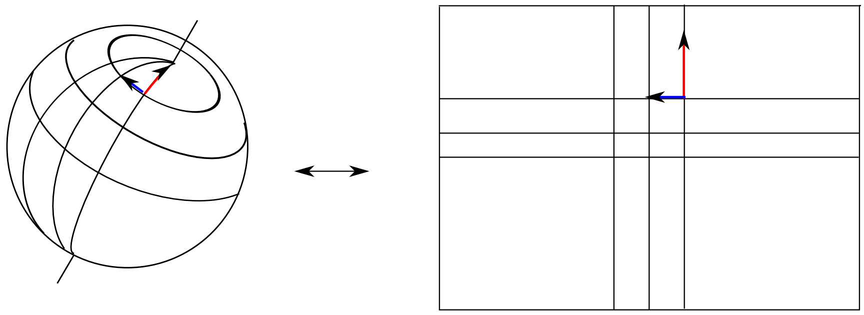

Figure 3.12: Distance stretching for two distances (red, blue) on a Mercator mapping.

cal point -1 can only be an initial guess for the location of the eigenfrequency. This initial guess should be reasonably close to the real eigenfrequency as long as there are no rapid changes in the derivative of the mapping function. Therefore, the curvature and the speed of the rotation should be moderate.
As already described in Jacobs [31], Polifke and Sattelmayer [93, 94] propose an iterative search for the eigenfrequency using the polynomial approximation. This search could be used for the exact (in the sense of the approximation) determination of both growth rate and eigenfrequency. Kopitz and Polifke [46], as mentioned above, propose a simplification and predict the growth rate from the scaled minimum distance of the Open Loop Gain Curve and the critical point.

3.3 CNN Method

The main components of the this method are CFD, Network models and Nyquist. Therefore, it has been named "*CNN*" approach. [44] It represents a hybrid approach which is not covered directly by the aforementioned methods. It consists of a combination of different elements from those methods.

The CNN method has been proposed and investigated by Kopitz [44, 46] for simple geometries and will be further studied in this work. References [44,46,74,75,77] represent most of the information available for this approach. A summary is provided in this section. Figure 3.13 illustrates where this approach is located compared to the aforementioned techniques.

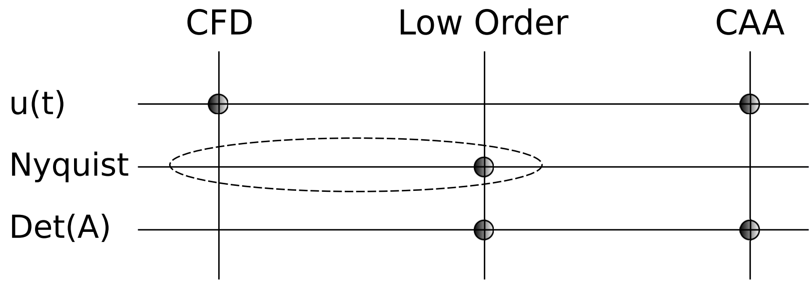

Figure 3.13: Matrix of different methods of modeling (horizontal) and different methods for the determination of the stability (vertical). Dots show the possibility of combination of method for modeling and prediction. The dashed ellipse highlights the location of the CNN method.

3.3.1 Motivation

An overview over established models for the prediction of thermo-acoustic stability has been given in section 3.1. Two substantially different methods can be identified there. Transient calculation on the one hand and modeling in the frequency domain followed by analysis either by finding the eigenvalues or applying Nyquist methods on the other hand. The most important advantage of the former method is surely the fact that all important effects are simulated in one single calculation and therefore most interactions are regarded. Apart from the huge amount of computational power required to simulate a possibly long time for the evolution of the mode, only rather unstable modes can be detected and only the most unstable mode can develop [24, 68, 101, 114]. Additionally, changes in the set-up or operating conditions require a new, computationally expensive calculation. Possibly a time consuming re-meshing is also required.

The latter methods have the advantage that they often rely on simple models, which allow quick evaluations. Their disadvantage is mostly the substancial simplification. For example, heat release has to be included using simplified models or experimental data. Moreover, effects of acoustically non-compact heat release are analytically hard to describe and mean flow effects in turbulent flow nearly impossible to estimate when CFD is not used. Due to the separation of acoustic calculation and mean flow calculation, interactions between these effects can not be represented properly. Therefore, especially network models can only give a strongly simplified image of the configuration, when complex geometries and flow configurations are involved.
Combinations of CFD and low order modeling have already been described by several authors (e.g. [21–23, 113]). Mostly, they use CFD to obtain unknown quantities for the low order modeling, often flame transfer functions. Also the acoustic transfer behavior of geometrically complex systems can be obtained using CFD. In both cases methods of system identification are used (see section 2.8). For pure flame transfer functions, often a single input - single output identification is sufficient, while for acoustic transfer properties, multiple input - multiple output identification is required. Still, the big advantage of transient CFD, the good reproduction of interactions, is hardly exploited and CFD results are mostly reduced to parameters for a semi-analytical model, e.g. for the heat release fluctuation in the case of flame transfer functions.
Kopitz and Polifke [44,46,74,75,77] have developed a different approach which should overcome the disadvantages of CFD and low order modeling, while preserving the advantages of the single methods. The approach is capable of taking advantage of the interactions taking place in the CFD domain while using a single input - single output identification. At the same time it still permits quick changes in the configuration without an expensive new CFD calculation. The next section provides a description of this approach.

3.3.2 Description

The basic concept of the approach is to divide the system into two domains. One is calculated using LES and the other using network models. In order to use the advantages of the LES, the parts of the system that involve complex interactions like flames, swirl generators or high turbulence should be included in the LES domain. Simple parts, for which accurate low order descriptions are known, like air or fuel supply systems, should be included in the network domain. Figure 3.14 shows such a configuration. It should be mentioned here that LES is performed in the time domain, while the network models work in the frequency domain.

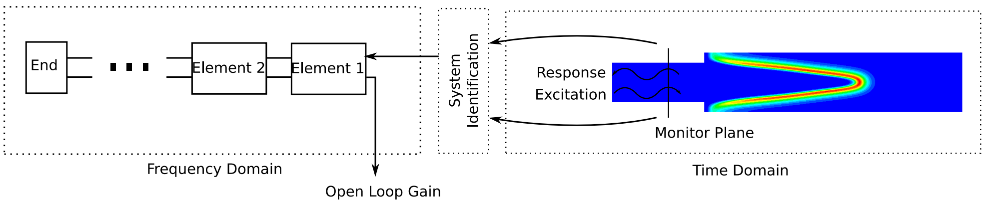

Figure 3.14: The hybrid approach illustrated for the example of a small burner

The LES domain includes not only one part but necessarily also one physical termination of the system. The boundary condition at the interface to the network model is formed by a non-reflecting boundary condition. This boundary condition also provides the possibility of imposing an acoustic excitation (see chapter 4.2). A transient calculation of the LES domain is performed, imposing an excitation (of a wave, e.g. $\mathfrak{f}$) using either various frequencies or white noise, on the interface and recording the response (e.g. $\mathfrak{g}$). Using now tools from system identification, e.g. a Fast Fourier Transformation or a correlation based identification (see section 2.8), a frequency dependent complex reflection coefficient representing the acoustic properties of the system can be determined. The LES domain is reduced to a black box whose response to an acoustic excitation of different frequencies is recorded. The response of the LES domain is called Part Loop Transfer Function (PLTF) in this work. The PLTF corresponds to a frequency dependent complex reflection coefficient. This reflection coefficient is used in the network model to account for the LES domain. The stability of the system is now evaluated using open loop gain methods which are described in section 3.2. This is necessary, because no analytical model is present in the network model to describe the LES domain, but only data for real frequencies representing the answer of the "black box", i.e. the LES domain. To summarize, some major advantages for this method are expected:

- Parameter studies can be easily carried out using the same LES results, as long as the variations are part of the network domain. The low computational requirements of the network model permit nearly immediate results for variations.
- Complex interactions simulated in the LES are represented adequately in the network model.
- The system identification is reduced to a single input - single output system, minimizing identification problems

3.3.3 Application

Two validation cases have been calculated by Kopitz, a Rijke tube and a duct system [44,46]. In both cases, the CNN method was able to predict the system's stability properties with good accuracy. This means that the method has been validated in a cold case and a hot case, but without combustion. Both cases are laminar. Consequently, in this thesis, the complexity of the cases is increased: first a laminar premix burner is examined and later a turbulent premix burner. In general, the new method is intended for any case that requires parameter studies and involves acoustic elements that cannot be modeled easily in low order approaches.

4 Adaption of the CFD Solver AVBP

AVBP is a solver for the compressible Navier-Stokes equations. Either DNS or LES methods can be applied. AVBP provides the possibility of solving flow including multiple species and permits the simulation of combustion as well as further features like two phase flow. AVBP was developed by Cerfacs in Toulouse. Numerous citations are available for AVBP; for a general overview, Cerfacs recommends [95].
Since AVBP simulates compressible flow, it captures acoustics within the flow. This property is used for the CNN method. Nevertheless, different modifications have been incorporated into AVBP in order to provide an optimized interface between the CFD domain, i.e. AVBP and the low order modeling. This interface requires two items:

- a possibility to extract 1D acoustic data,
- a non-reflecting termination.

The first item is straightforward to understand, since the acoustic data from the LES have to be transferred into the network model. The second item is required, because at the interface the acoustic waves should be unaffected by the end of the LES domain as they enter the network domain then. This as well as the incorporation of these features into the solver are described in the following sections.

4.1 Acoustic Data Extraction for Planar Waves

4.1.1 Motivation

The approach presented in this thesis uses LES to simulate the impact of certain effects on planar wave fronts. LES operates in the time domain, while the second part of the approach, the network model, uses the frequency domain [44]. Therefore, it is necessary to effectively transfer data from planar wave fronts from the time domain into the frequency domain. For this transfer, depending on the desired frequency range, a certain amount of data at a certain sampling frequency is required. The Nyquist-Shannon theorem,

$$f_{\text{sample}} > 2(f_{\max} - f_{\min}), \tag{4.1}$$

and the condition for the lowest frequency,

$$f_{\min} = 1/t_{\text{sample}}, \tag{4.2}$$

where $t_{\text{sample}} = n/f_{\text{sample}}$ for n data points in time, determines this amount. A single solution file of an LES has several hundred megabytes for a grid of around 10 million cells. Keeping these facts in mind, it is obvious that extracting the acoustic information from full solution files at a reasonable sampling rate will require a huge amount of disk space. Additionally, for the extraction of data from planar wave fronts at certain points of the domain, not the entire solution field is required, but only data from a plane parallel to the wave front. Therefore, surface average values at the single planes ($\bar{u}'$ and $\bar{p}'$) are sufficient to describe the wave front:

$$\bar{u}' = \frac{1}{S}\int_S (u - \bar{u})\, dS \tag{4.3}$$

$$\bar{p}' = \frac{1}{S}\int_S \left(p - \bar{p}\right) dS. \tag{4.4}$$

This does not affect the detection of the acoustic quantities, since for waves traveling in a direction perpendicular to the boundary condition, the wave fronts are planar and parallel to the planes. In the case of turbulent compressible flow, the extraction of the acoustic information might be difficult due to the turbulent fluctuations $(\tilde{\ })$ in the flow which are superposed to the acoustic fluctuations $(')$. This can be expressed by

$$p = \bar{p} + p' + \tilde{p} \;\rightarrow p - \bar{p} = p' + \tilde{p}, \tag{4.5}$$

$$u = \bar{u} + u' + \tilde{u} \;\rightarrow u - \bar{u} = u' + \tilde{u}. \tag{4.6}$$

The definition of the planes has the advantage that turbulent fluctuations vanish for the most part, because they are randomly distributed over the cross section and cancel out in the averaging process. In the case of strong compressible effects, the averaging process may not be sufficient for eliminating the effect of turbulence. Kopitz et al. [45] have proposed a method to overcome this problem: "Characteristics Based Filtering" (CBF). In a first step, the CBF method proposes to define a multitude of monitor planes in the flow, whose orientation is parallel to the impinging wave front. The monitor planes are situated within a distance of the actual point for the identification of the acoustic quantities. In a second step, the different propagation speeds of turbulence $(\bar{u})$ and acoustics $(\bar{c})$ are utilized in order to separate the two phenomena. The average values of the planes are stored over a certain period of time and at each instant of time the values of all monitor planes are summed up and averaged ($\langle u'\rangle$ and $\langle p'\rangle$), whereby the speed of the propagation of the acoustic wave $(c \pm u)$ is taken into account: a "time-lagged-average" is generated. This is done by adding up the values from the time instances, at which the acoustic wave is in the same phase at the different planes:

$$\langle p'\rangle = \frac{1}{n}\sum_{1}^{n} \bar{p}'\left(x - \Delta x_{\mathrm{n}}, t - \frac{\Delta x_{\mathrm{n}}}{c \pm u}\right), \tag{4.7}$$

$$\langle u'\rangle = \frac{1}{n}\sum_{1}^{n} \bar{u}'\left(x - \Delta x_{\mathrm{n}}, t - \frac{\Delta x_{\mathrm{n}}}{c \pm u}\right). \tag{4.8}$$

The speed of sound has to be known for this procedure. The idea behind this procedure is that the acoustic quantities are retained, while the turbulent quantities are averaged out because they are uncorrelated. The method is similar to the Multi Microphone Method used e.g. by Fischer et al. [15] or Paschereit et al. [67] in experiments.

To conclude, there is a demand for a tool which permits arbitrary monitor planes to be defined in the domain and data to be extracted from those planes during the solver run independently from the generation of the usual solution files.

4.1.2 Definition of Monitor Planes

The requirement of arbitrary monitor planes demands a possibility to define planes that is independent from the grid structure, like internal boundaries and existing cell faces. The mesh is assumed to be constant during the simulation. This implies that no moving mesh approaches can be used with the tool described here. In a preprocessing step, planes are defined and in a linear interpolation, the tool calculates the nodes of the mesh which contribute to the data on the plane as well as the corresponding interpolation factors. The algorithm for the calculations is presented here briefly, the text corresponds to parts of an internal report for Cerfacs [32].
The planes can be calculated for most common 3D elements. Anyway, to simplify the calculation the tool internally decomposes any element into tetrahedron elements, which permit a completely linear calculation. For linear func-

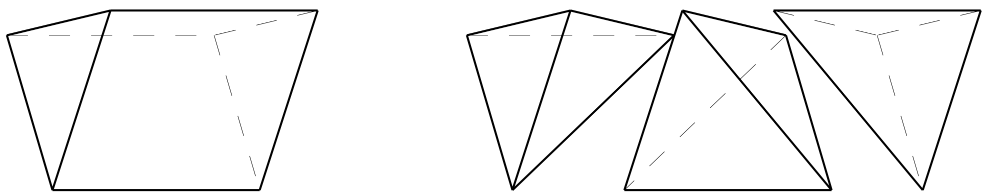

Figure 4.1: Decomposition of a prism element into tetrahedron elements.

tions $f(x) = ax + b$, which are now defined on every tetrahedron element ($_{\mathrm{el}}$) by the values of its nodes, one can calculate for a plane through the element:

$$\int_{S_{\mathrm{el}}} f(x)dS = \int_{S_{\mathrm{el}}} (ax+b)\,dS = a\int_{S_{\mathrm{el}}} xdS + \int_{S_{\mathrm{el}}} bdS \tag{4.9}$$

which means:

$$\int_{S_{el}} f(x)\, dS = A f\left(x_{cgr}\right) \tag{4.10}$$

with ($_{cgr}$) meaning center of gravity.
So the problem basically reduces to an equation similar to the calculation of the center of gravity of the plane surface through each element.

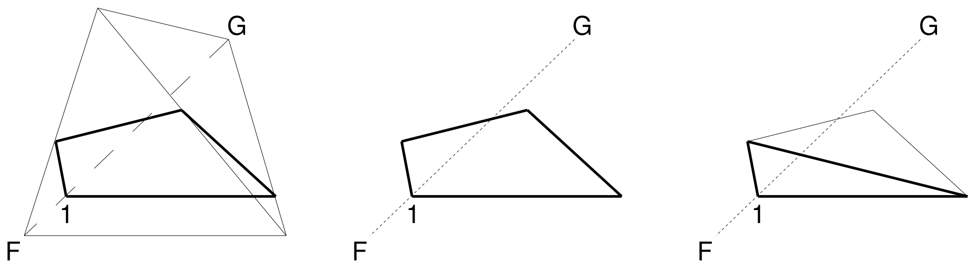

Figure 4.2: Decomposition of the intersection and calculation of the contribution.

$$\int_{S_{el}} (ax+b)\, dS = S\left(ax_{cgr}+b\right) \tag{4.11}$$

This is done by decomposing each surface of intersection of the plane with an element into triangles ($_{tri}$). And for a triangle (with vertices 123) the calculation is easy, as

$$x_{cgr} = \sum_{i=1,2,3} \frac{1}{3} x_i. \tag{4.12}$$

So the integral reduces to

$$\int_{S_{tri}} (ax+b)\, dS = S_{tri} \sum_{i=1,2,3} \frac{1}{3}(ax_i+b) = S_{tri} \sum_{i=1,2,3} \frac{1}{3} f(x_i). \tag{4.13}$$

The contribution of each vertex of the triangle i is therefore

$$S_{tri} = \frac{1}{3} f(x_i). \tag{4.14}$$

A vertex (1) of the triangle is generally situated between two nodes (F,G) of the mesh. Using the properties of the linear field, we know that

$$f(x_1) = \frac{|x_G - x_1|}{|x_G - x_F|} f(x_F) + \frac{|x_1 - x_F|}{|x_G - x_F|} f(x_G). \tag{4.15}$$

So finally the contribution α of one node (F) to the plane can be calculated by summing up all contributions to the triangles,

$$\alpha = \sum_{el} \sum_{tri} \frac{|x_G - x_1|}{|x_G - x_F|} \frac{1}{3} A_{\text{tri}}. \tag{4.16}$$

4.1.3 Plane Data Acquisition

The list of nodes and contributions is read by AVBP. The list is partitioned and sent to the slave processes. These calculate the integrals over the planes simply by taking the desired values at the n nodes given by the list, multiplying them with the corresponding factor and summing them up. The slaves join their data via Message Passing Interface (MPI) and build up the total plane integral in this manner:

$$\int_{S_{\text{tot}}} f(x)\,dS = \sum_{i=1\ldots n} \alpha_i f_i. \tag{4.17}$$

In this way, the data of the planes is available independent of the complete solution and can both be written to a file or used internally.

4.2 Time Domain Impedance Boundary Condition

4.2.1 Motivation

In CFD- simulations involving acoustics, the boundary conditions have to fulfill a double role. They have to present adequate properties for both the mean flow and the acoustic field [33]. This is not necessarily the case for standard boundary conditions - a simple example may illustrate this: a fixed pressure outlet boundary condition presents an acoustically fully reflecting boundary condition [90], which may not be correct.
In the surroundings of LES and DNS, non-reflecting boundary conditions are of importance to permit the fluctuations generated by the flow field to leave the domain. This is of special importance for low dissipative numerical

schemes, where acoustics are not damped by the numerical treatment. Otherwise, slow convergence or undesired interactions between flow, combustion and acoustics may be the consequence [70].
For the explicit simulation of acoustical phenomena within the numerical simulation of the flow field, complex impedances may have to be incorporated into the boundary conditions in order to have a well described and physically consistent setup for the acoustic field [65].
With respect to non-reflecting boundary conditions, two different formulations for non-reflecting boundary conditions can be distinguished [83]: global and local methods. While global methods transform the governing equations, local ones achieve their properties by locally regarding the flow field at the boundary condition [83]. In terms of local formulations sponge layers or perfectly matched layer approaches intend to absorb acoustic perturbations in a layer located at the boundary. A brief overview over sponge layer, perfectly matched layer and related methods is given in [26] or [8]. A different formulation for non-reflecting boundary conditions can be made in terms of the perturbations or characteristics [83]. The method has been developed for the linearized Euler equations, see e.g. [90], and adapted for DNS and LES purposes. [70, 83]. The method is referred to as Navier Stokes Characteristic Boundary Conditions (NSCBCs). This kind of boundary condition is the standard for the LES solver AVBP [2]. Modifications on this approach have been performed by Prosser and Schlüter [83]. A drawback of this type of boundary condition is the fact that for practical simulations the boundary condition cannot be set to 100% non-reflecting because it loses the ability to control the mean pressure (outlet) or velocity (inlet) [82]. Therefore, a modified formulation has been proposed using both pressure and velocity information to overcome this limitation [82, 109]. Based on this and the characteristics based filtering [45], a time domain impedance boundary condition has been formulated [33]. This approach will be discussed in the following subsections. These subsections are strongly based on Huber et al. and Kaess et al. [29, 33].

4.2.2 Navier-Stokes Characteristic Boundary Conditions

The bases for the boundary condition presented here are the Navier-Stokes Characteristic Boundary Conditions (NSCBCs). In this section only outlet boundary conditions will be discussed; similar considerations can be made for inlet boundary conditions. In the form applied in this context the boundary conditions were developed by Poinsot and Lele [70]. Thompson [105] has demonstrated a way to obtain the set of characteristic waves $\mathscr{L}_i$ from the primitive variables. For such a set of variables Engquist and Majda [14] have proposed non-reflecting boundary conditions. These approaches have been used and combined with a linear relaxation term proposed by Rudy and Strikwerda [90] to form a well posed boundary condition. Determining the characteristics proves to be difficult for viscous systems [70]. Therefore Poinsot and Lele [70] suggest to use a locally inviscid system of equations, the "local associated one-dimensional inviscid" (LODI) approach. The viscous contribution is added later and the wave amplitudes are calculated using

$$\mathscr{L}_1 = (u_1 - c_1)\left(\frac{\partial p}{\partial x_1} - \rho c \frac{\partial u_1}{\partial x_1}\right), \tag{4.18}$$

$$\mathscr{L}_2 = u_1\left(c^2 \frac{\partial \rho}{\partial x_1} - \frac{\partial p}{\partial x_1}\right), \tag{4.19}$$

$$\mathscr{L}_3 = u_1 \frac{\partial u_2}{\partial x_1}, \tag{4.20}$$

$$\mathscr{L}_4 = u_1 \frac{\partial u_3}{\partial x_1}, \tag{4.21}$$

$$\mathscr{L}_5 = (u_1 + c_1)\left(\frac{\partial p}{\partial x_1} + \rho c \frac{\partial u_1}{\partial x_1}\right). \tag{4.22}$$

The first and the last equation correspond to acoustic waves, while the middle ones correspond to convective waves. Using the characteristic waves, the derivative of the pressure can, for example, be expressed as

$$\frac{\partial p}{\partial t} = -\frac{1}{2}\left(\mathscr{L}_5 + \mathscr{L}_1\right). \tag{4.23}$$

Hence, a conventional pressure outlet could be formulated as

$$\mathscr{L}_1 = -\mathscr{L}_5. \tag{4.24}$$

Using the characteristic properties $\mathscr{L}$, an for upstream traveling wave, a non reflecting outlet could be written easily using

$$\mathscr{L}_1 = 0. \tag{4.25}$$

This strictly non-reflecting outlet boundary condition is not well posed, because such a formulation does not have the ability to preserve the mean pressure. Therefore, Poinsot and Lele use the aforementioned relaxation term by Rudy and Strikwerda [90], which introduces a pressure dependency into the equation.

$$\mathscr{L}_1 = K\left(p - p_\infty\right) \tag{4.26}$$

Here, a coupling parameter K is used to connect the ingoing wave $\mathscr{L}_1$ with the pressure drift $p - p_\infty$. A coupling parameter of $K = 0$ would again lead to the perfectly non-reflecting, but ill posed boundary condition. A high K increases the pressure correction and at the same time the reflection and can lead to instability. The reflection coefficient $\mathscr{R} = \frac{\hat{\mathfrak{g}}}{\hat{\mathfrak{f}}}$ can be calculated to be [82]

$$\mathscr{R} = \frac{-1}{\frac{2i\omega}{K} + 1}. \tag{4.27}$$

For $K \to \infty$, the reflection coefficient becomes $\mathscr{R} = -1$, while for $K \to 0$ it tends towards $\mathscr{R} = 0$. So, K has to be chosen as a compromise between reflection and mean pressure control. [33] The reaction of this boundary condition to mean pressure fluctuations can be assessed by calculating a relaxation time, the characteristic time which is needed to correct the mean pressure drift. Combining equations 4.23 and 4.26 one obtains

$$\frac{\partial p}{\partial t} = -\frac{1}{2} K \Delta p \tag{4.28}$$

$$\Rightarrow \Delta p(t) \sim e^{-\frac{2}{K}t}. \tag{4.29}$$

This implies a time constant of

$$\tau = 2/K \tag{4.30}$$

for the mean pressure correction.

4.2.3 Plane Wave Masking

Polifke et al. have proposed a modified formulation which is non-reflecting while still providing mean pressure control [35, 82, 109]. The idea is based on the linear superposition of different effects in pressure and velocity fluctuations. The pressure p and the total velocity u are the combination of mean $\bar{(\,)}$, turbulent $\tilde{(\,)}$ and acoustic $(\,')$ contributions:

$$p = \bar{p} + \tilde{p} + p' \tag{4.31}$$

$$u = \bar{u} + \tilde{u} + u' \tag{4.32}$$

Distinguishing between those three contributions can prove to be difficult [45]. For acoustic contributions, there is a relationship between p' and u' and the characteristic waves. Let $\mathfrak{f}$ be a downstream travelling wave and $\mathfrak{g}$ be an upstream travelling wave, then

$$\mathfrak{f} = \frac{1}{2}\left(\frac{p'}{\rho c} + u'\right) \tag{4.33}$$

$$\mathfrak{g} = \frac{1}{2}\left(\frac{p'}{\rho c} - u'\right). \tag{4.34}$$

Comparing this to the characteristics $\mathscr{L}_1$ and $\mathscr{L}_5$, one can see that the relationship between the two wave formulations is the partial time derivative:

$$\mathscr{L}_1 \sim 2\rho c \frac{\partial \mathfrak{g}}{\partial t}. \tag{4.35}$$

Close to a non-reflecting boundary condition, $\mathfrak{g}$ becomes $\mathfrak{g} = 0$. Therefore, the acoustic pressure contribution p' can be calculated as

$$\begin{aligned} p' &= \rho c(\mathfrak{f} + \mathfrak{g}) \\ &= \rho c \mathfrak{f} \\ &= \rho c \frac{1}{2}\left(\frac{p'}{\rho c} + u'\right). \end{aligned} \tag{4.36}$$

This coupling of pressure and velocity permits acoustic and mean pressure fluctuations to be distinguished. The disadvantage is that both pressure and velocity information are needed. Hence, as the boundary condition should keep the mean pressure constant but not react on acoustic waves, the acoustic pressure has to be subtracted from the pressure difference term. In that case, only the pure mean pressure drift is corrected and the acoustic waves are masked. Due to the application of a cross section average for the acoustic values, only plane waves can be masked this way [33]:

$$\mathscr{L}_1 = K\left(p - \rho c \frac{1}{2}\left(\frac{p'}{\rho c} + u'\right) - p_\infty\right). \tag{4.37}$$

Polifke et al. and Kaess et al. have demonstrated the effectiveness of this approach [33, 35, 81, 109]. Theoretically, the reflection coefficient of this boundary condition to planar wave fronts is zero. Practically, it is very low, around 1% [33,35], independent of the coupling parameter K. The mean pressure correction is in fact affected by this modification. Assuming a non-acoustic pressure drift Δp, equation 4.37 yields

$$\mathscr{L}_1 = K\left(\Delta p - \rho c \frac{1}{2}\left(\frac{\Delta p}{\rho c} + 0\right)\right) = \frac{K}{2}\Delta p. \tag{4.38}$$

Therefore, the relaxation time for this case can be calculated using equations 4.23 and 4.26:

$$\frac{\partial p}{\partial t} = -\frac{1}{4}K\Delta p \tag{4.39}$$

$$\Rightarrow \Delta p(t) \sim e^{-\frac{4}{K}t}. \tag{4.40}$$

The time constant is $\tau = 4/K$ and has increased by a factor of two compared to the non-modified boundary. This implies that for a stable numerical set up, the coupling coefficient K for the modified formulation has to be doubled. Non-planar components of acoustic waves are not compensated by this modified boundary condition and are reflected according to the non-modified boundary term $\mathscr{L}_1$, equation 4.26. Therefore, K should not be set too high, although the reflection of the modified boundary condition to planar waves does not depend on K. Otherwise, non-planar components, which always are present in turbulent full 3D LES, might cause significant reflections. The author has observed an influence of the coupling coefficient K on high order modes. High Ks promote the occurrence of these modes.

4.2.4 Imposing External Excitation

The boundary condition for the context of this work has to provide the possibility of imposing an excitation and at the same time be non-reflecting. These at first glance contrary targets can be achieved with further modifications to the term presented in equation 4.37. The standard implementation of the Poinsot Lele boundary condition in AVBP offers the possibility of imposing a sinusoidal signal. The method presented here is similar, straightforward and works for random excitations. Imposing a signal means adding a signal to the wave $\mathscr{L}_1$ produced by the non-reflecting formulation, equation 4.37. If the signal is formulated in terms of $\mathfrak{f}$ and $\mathfrak{g}$, we denote $\mathfrak{g}^0$ as the desired excitation, which can be chosen arbitrarily. The assumption $\mathfrak{g} = 0$, which was valid for the purely non-reflecting boundary condition, is not valid here anymore. The $\mathfrak{g}$-term in equation 4.37 has to be considered in the boundary formulation as well as the relationship between $\mathscr{L}$ and $\mathfrak{g}$, equation 4.35. Then, the boundary term becomes:

$$\mathscr{L}_1 = K\left(p - \rho c\left(\frac{1}{2}\left(\frac{p'}{\rho c} + u'\right) + \mathfrak{g}^0\right) - p_\infty\right) + 2\rho c\frac{\partial \mathfrak{g}^0}{\partial t}. \tag{4.41}$$

Any signal $\mathfrak{g}^0$ can be imposed in this way, provided its derivative is known. For the implementation of the excitation done in this work, the excitation signal is given in the form of a discrete time series. This series contains the value of $\mathfrak{g}^0$ for each time step. The time derivative is then calculated using a simple numerical derivative between two time steps.

4.2.5 Time Domain Impedance Boundary Condition

This subsection describes an additional feature, which has been incorporated into the boundary formulation, but is not used in the framework of this thesis. Nevertheless, it is described here to complete the section on the boundary condition.

Up to now, the boundary condition has been non-reflecting and permits excitation. Now, the boundary condition shall present a user-defined impedance of equivalently reflection coefficient. Impedance ($\mathscr{Z}$) and reflection coefficient ($\mathscr{R}$) are defined as follows, both are frequency dependent ($\mathscr{R}(\omega)$, $\mathscr{Z}(\omega)$):

$$\hat{\mathscr{R}}(\omega) = \frac{\hat{\mathfrak{g}}(\omega)}{\hat{\mathfrak{f}}(\omega)}, \tag{4.42}$$

$$\hat{\mathscr{Z}}(\omega) = \frac{p'(\omega)}{u'(\omega)}. \tag{4.43}$$

They represent different mathematical formulations to express the reflection properties and can be converted mutually:

$$\mathscr{Z} = \rho c \frac{1+\mathscr{R}}{1-\mathscr{R}}. \tag{4.44}$$

Hence, for the boundary condition, a reflected signal can be present which fulfills

$$\mathfrak{g} = \mathscr{R}\mathfrak{f}. \tag{4.45}$$

For the wave masking procedure, subsection 4.2.3, the ingoing wave $\mathfrak{f}$ has been determined and therefore is available. In the previous section it was shown that arbitrary excitations can be imposed by the boundary condition. As a consequence, it is no problem to create a reflection, which is just an excitation calculated as a function of $\mathfrak{f}$. A fully reflecting boundary condition would simply record $\mathfrak{f}$ and impose this value as $\mathfrak{g}^0$. In a time domain impedance boundary condition the response of the boundary is not trivial to calculate. Mostly, a frequency dependent reflection coefficient has to be modeled but the boundary condition works in the time domain. This could be done by an inverse Fourier transformation, but this involves a convolution integral which is computationally expensive [29]. Many authors use analytical descriptions for the impedance or reflection coefficient which can be transformed analytically [18, 68, 87] but this is generally not possible. Therefore, the problem for the boundary condition is the effective calculation of the correct response signal $\mathfrak{g}^0$. This kind of problem is known from signal processing and radio technology. Z-transform has been used by Sullivan [102] to solve this issue. Application to acoustics has been done among others by Özyörük and Long [65], and recently by Huber et al. [29] and Kaess et al. [33]. Although the impedance and the reflection coefficient carry the same information and can be easily transformed vice versa, there is a difference in terms of signal processing. The formulation in terms of characteristics used for the reflection coefficient is likely to be causal. This implies that the reflected quantity only depends on the past of the incoming quantity. This is not necessarily the case for the formulation in terms of p' and u', which is used for the impedance, because both p' and u' carry information on both the incoming and the reflected waves [17]. Causality is a requirement for the formulation of the boundary conditions. When causality is assumed but is not present, instability will occur [19]. The approach for the creation of the artificial response follows the work of Huber et al. [29] and has been described in Kaess et al. [33]. The reflection coefficient, defined

$$\hat{\mathscr{R}}(\omega) = \frac{\hat{\mathfrak{g}}(\omega)}{\hat{\mathfrak{f}}(\omega)} \tag{4.46}$$

in the frequency domain, can be transformed into the time domain using inverse Fourier transformation. Assuming a causal system, this yields

$$\begin{aligned} \mathfrak{g}(t) &= \mathscr{R}(t) * \mathfrak{f}(t) \\ &= \int_0^\infty \mathscr{R}(\tau)\mathfrak{f}(t-\tau)d\tau, \end{aligned} \tag{4.47}$$

where $\mathscr{R}(t)$ denotes the inverse Fourier transform of $\mathscr{R}(\omega)$. As mentioned above, the evaluation of this integral is numerically expensive and therefore not suitable for an effective calculation. Following Sullivan [102] and Özyörük and Long [65] an inverse z-transform is applied instead. The transform is defined

$$\mathscr{Z}(x(i)) = X(z) = \sum_{i=-\infty}^{\infty} x(i)z^{-i} \tag{4.48}$$

and has beneficial properties concerning convolution integrals. The z-transform of a convolution is

$$\mathscr{Z}(\mathscr{R}(t) * \mathfrak{f}(t)) = R(z)\mathfrak{g}(z). \tag{4.49}$$

Another interesting property is the time-shift property:

$$\mathscr{Z}(x(i-k)) = z^{-k}X(z). \tag{4.50}$$

The discrete Fourier transform is a special case of the z-transform for $z = i\omega t$ [57]. This illustrates that an approximate representation of the reflection coefficient $\mathscr{R}$ in the z-domain is equivalent to an approximation in the frequency domain. For this approximation a function of the type

$$\mathscr{R}(z) = \frac{a_0 + a_1 z^{-1} + a_2 z^{-2} + \ldots + a_n z^{-n}}{1 - (b_1 z^{-1} + b_2 z^{-2} + \ldots + b_m z^{-m})} \tag{4.51}$$

is used. A sufficient amount of coefficients a and b has to be fitted to approximate the reflection coefficient in frequency domain. An inverse z-transformation then takes advantage of the time-shift property and results in

$$\mathfrak{g}(z) = \mathscr{R}\mathfrak{f}(z), \tag{4.52}$$

$$\begin{aligned}\mathfrak{g}(t) - b_1\mathfrak{g}(t-\Delta t) - \ldots - b_m\mathfrak{g}(t-m\Delta t) = \\ a_0\mathfrak{f}(t) + a_1\mathfrak{f}(t-\Delta t) + \ldots + a_n\mathfrak{f}(t-n\Delta t),\end{aligned} \tag{4.53}$$

$$\begin{aligned}\mathfrak{g}(t) = a_0\mathfrak{f}(t) + a_1\mathfrak{f}(t-\Delta t) + \ldots + a_n\mathfrak{f}(t-n\Delta t) + \\ b_1\mathfrak{g}(t-\Delta t) + \ldots + b_m\mathfrak{g}(t-m\Delta t).\end{aligned} \tag{4.54}$$

The response is calculated as a weighted sum over the ingoing and outgoing waves over a limited amount of previous time steps. This procedure only requires a small amount of computational power and therefore does not significantly slow down the calculation. The procedure works for a fixed time step. The amount of coefficients necessary to reproduce the reflection coefficient can be estimated by considering the fact that the ingoing signal history has to be included in the calculation as long as it contributes to the outgoing signal. Hence, if the reflection coefficient incorporates a characteristic time lag of t_{lag}, the amount of coefficients n will roughly be

$$n = \frac{t_{lag}}{\Delta t}, \tag{4.55}$$

where Δt is the time step of the computation. Still, the poles of this approximation function have to lie in the upper complex ω-plane to ensure causality and therefore numerical stability. An unconditionally stable filter is achieved for $m = 0$, because this approximation does not have poles. Different filters have been set up and tested in different configurations by Kaess et al. [33] using this implementation. The results are promising and demonstrate the potential of this approach.

5 Limitations

In the second test case, described in section 6.2, substantial difficulties arise in the application of the CNN method. Therefore, a section treating OLTF's that do not permit a reliable stability prediction is included here. It constitutes important experience and considerations gained during the calculation of the test cases. Unexpected behavior of Nyquist curves also has been reported by other users of such methods [96].

5.1 Requirements for the Location of the Cut

The application of the Nyquist method should open the unstable/stable acoustic feedback loop. It should thereby prevent the occurrence of the eigenmode in the simulation of the open system, while permitting its occurrence in the closed system to be predicted. In other words, the cut has to be located in a way that interrupts the feedback of the instability.
In contrast to simple control loops, general acoustic systems have multiple feedback lines. In terms of network models this means that feedback occurs at any element whose scattering matrix has elements $\neq 0$ on the reflecting positions ($\mathfrak{S}_{12}$ and $\mathfrak{S}_{21}$). This does not necessarily imply the occurrence of an eigenfrequency on this feedback line, but it should be kept in mind.
Network models are not necessarily linear (in the sense of their topography). As the name implies, they are rather a network than a chain of elements. Locating the cut inside the network may not provide the desired effect of the interruption of the feedback because of the existence of side branches, which might still provide closed loops. The location of a cut, i.e. a Nyquist-dummy, would likely modify the acoustic properties of the system, but not prevent the eigenfrequencies.
To summarize the requirements: the open system must not have feedback

lines or eigenmodes left, otherwise the Nyquist method will, at least in the corresponding frequencies, fail. Unfortunately, the shape of the eigenmodes is likely not to be known a priori. If the cut of the system does not intersect the feedback of the instability, the system of equations describing the opened thermo-acoustic configuration will be close to a singularity at the corresponding frequency. This implies that the matrix will be badly conditioned and mathematically hard to handle, and simplified models may deliver bad results. These items lead to highly fluctuating results close to the eigenfrequency, which may be seen in the Nyquist plots.

5.2 Indicators

As mentioned above, the condition that has to be fulfilled for conformal mapping is a non-zero derivative. According to Betz [4], the mapping properties can also be local. So, if the mapping is conformal in the vicinity of the eigenfrequency and between the real axis and the eigenfrequency, the generalized Nyquist criterion is valid. If the derivative of the mapping function is zero or tends towards infinity in the vicinity of a eigenfrequency, an interpretation from the Nyquist plot is impossible. The difficulty now is to draw conclusions concerning the properties of the mapping in the complex plane ($\omega \in \mathbb{C}$) from the information which is present only for real frequencies ($\omega \in \mathbb{R}$).
For this purpose we assume that the mapping function is, on a subset Ω of the complex plane $\mathbb{C}$, locally analytic, i.e. that

$$\lim_{z \to 0} \frac{f(z+\Delta z) - f(z)}{\Delta z} \quad \exists, \forall\ z \in \Omega. \tag{5.1}$$

In this case the limit is independent of the choice of z. Hence, the derivative of the mapping function along the the real frequency axis, $\frac{\partial f}{\partial z}$, is relatively easy to extract from the Nyquist curve and independent of the choice of z ($z \in \mathbb{R}$ or $z \in \mathbb{C}$):

$$\frac{\partial f}{\partial z} \approx \frac{f(z+\Delta z) - f(z)}{\Delta z}. \tag{5.2}$$

For constant frequency stepping in the Nyquist curve ($\Delta z = \omega_{\mathrm{n}+1} - \omega_{\mathrm{n}} = \mathrm{const}$), the derivative is therefore proportional to the distance between the image points of two frequencies. This is mostly the case, since the Nyquist curve is usually generated by a for-loop over frequency. Hence, observing the images, i.e. the location on the Nyquist curve of two adjacent frequencies, is equivalent to observing a numerical derivative:

$$\frac{\partial f}{\partial z} \sim f(z+\Delta z) - f(z). \tag{5.3}$$

The derivative of the mapping function carries some information about the properties of the mapping:

- The magnitude of the derivative corresponds to the scale of the mapping.
- The argument of the mapping function corresponds to the angle of rotation of the mapping.

It is now possible to draw a conclusion from the derivative of the Nyquist curve to the mapping properties in vicinity of the curve if there are no rapid changes in the derivative. If there are rapid changes, the interpretation of the curve presents severe problems. Using a Taylor expansion of the derivative $\frac{\partial f}{\partial z}$,

$$\frac{\partial f}{\partial z}(z) = \frac{\partial f}{\partial z}(z_0) + \frac{\partial^2 f}{\partial z^2}(z_0)(z-z_0) + R(z), \tag{5.4}$$

there is an estimation for $R(z)$ which represents the possible error:

$$R(z) = \frac{\partial^3 f}{\partial z^3}(\zeta)\frac{(z-z_0)}{2!}, \tag{5.5}$$

where ζ is between z and z_0. The fact that the mapping function is usually of the type e^x implies that $\left|\frac{\partial^3 f}{\partial z^3}\right|$ becomes large, when $\left|\frac{\partial f}{\partial z}\right|$ is large. Hence, a large magnitude of the mapping function means that the vicinity, i.e. the interval where a prediction of the mapping is meaningful, becomes small. Therefore, the interpretation of the Nyquist curve is error prone near frequencies, where

- a change of the sense of rotation of the Nyquist plot (The derivative might have changed sign),
- small or vanishing distance between the image of two adjacent frequencies on the Nyquist curve (the derivative tends to zero),

- huge distances between the image of two adjacent frequencies on the Nyquist curve (the derivative tends to infinity),
- extremely small loops in the Nyquist curve (often comes along with the aforementioned item)

occur. A different location of the "cut" may help here, or an alternative cut which provides valid information at the frequencies affected can be applied.

5.3 Example 1: Duct System with Area Change

This example illustrates the effect of increasingly decoupled systems, i.e., a system where parts can have independent eigenmodes in an increasing way. The system is a simple *duct - area change - duct* system, with two open ends. Two sections, section 1 before the area change and section 2 after the area change, are distinguished. Four different indices are defined for variables at certain positions of the system: i at the inlet, u at the upstream side of the area change, d at its downstream side and o at the outlet.The area ratio $\alpha = \frac{A_2}{A_1}$ is varied from moderate to extreme values: $\alpha = 1, 1/4, 1/8, 1/32$.
The reflection coefficient $\mathscr{R}$ of the area change for section two can be obtained using the scattering matrix. For an area ratio of $\alpha = 1/8$ the reflection coefficient is $\mathscr{R} \approx -0.7778$ for both frequencies of $2\omega_0$ and $4\omega_0$.
Now, the reflection coefficient at the open end at section 2 (right) is set to $\mathscr{R} = -1/0.7778$. Hence, for an area ratio of $\alpha = 1/8$, a neutral (zero growth rate) eigenmode of $2\omega_0$ and $4\omega_0$ can be expected in section 2. The open end in section 1 (left) is damping, the reflection coefficient is arbitrarily set to $\mathscr{R} = -0.9$. This configuration is examined twice: once with the cut positioned in section 1 and once with the cut positioned in section 2.
The total length of the duct is $L = 0.85$ m with the area change in the middle. No mean flow and no losses are present and $c = 343$ m/s. The $\lambda/2$-eigenmode of the entire duct and its harmonics have frequencies of $f^* = 204$ Hz, 408 Hz, ..., denoted $2\pi f^* = \omega^* = \omega_0, 2\omega_0, ...$ here.
By increasing the area ratio, section 1 will exhibit properties which should more and more move towards a $\lambda/4$-system, while section 2 should develop

towards a $\lambda/2$-system. This means that section 2 will have eigenfrequencies of $\omega^* = 2\omega_0, 4\omega_0, \ldots$, whereas section 1 will have $\omega^* = \omega_0, 3\omega_0, \ldots$.
Figure 5.1 illustrates the aforementioned items.

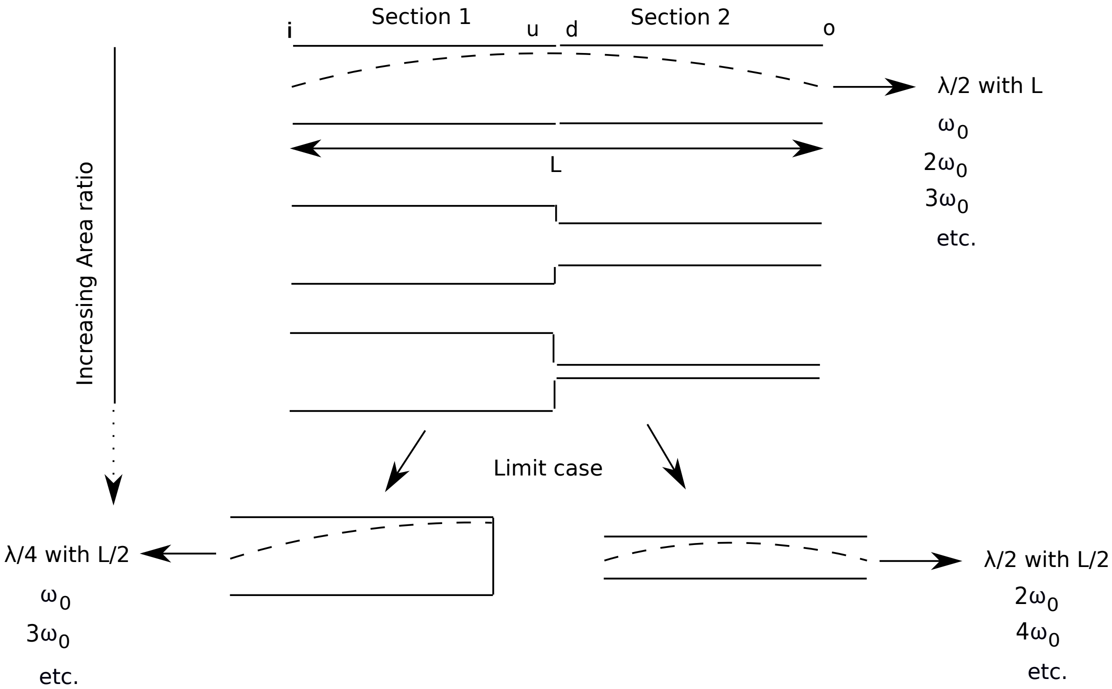

Figure 5.1: Illustration of the development of an area change with increasing area ratio.

For $\alpha = 1/8$, the following configuration appears at the eigenfrequency of section 2 in the equations for area change and open end at section 2. The duct of section 2 is not taken into account, which does not affect the validity of the following considerations (index 1 denotes section 1, index 2 section 2):

$$\mathfrak{f}_d = A\mathfrak{f}_u + B\mathfrak{g}_d \tag{5.6}$$

$$\mathfrak{f}_d = B\mathfrak{g}_d \tag{5.7}$$

From these equations follows that $\mathfrak{f}_u = 0$. But if the cut is applied in section one, $\mathfrak{f}_u \neq 0$, because it is forced by the Nyquist dummy. Hence, the system is ill posed when section two is in a neutral eigenfrequency. Close to the eigenfrequency, $\mathfrak{f}_d$ and $\mathfrak{g}_d$ take large values.
Figures 5.2, 5.3 show the mapping scale for the aforementioned configuration. They exhibit the properties that are expected from this simple model: Two

peaks, (one with $Re(\omega) = 2\omega_0$ and one with $Re(\omega) = 4\omega_0$) move towards the real axis. For $\alpha = 1/8$ the peaks are situated right on the real frequency axis, which is used for Nyquist methods. The corresponding Nyquist curve in figure 5.4 shows massively deformed loops. These loops correspond to to the eigenfrequencies of section 2 observed with the cut located in section 1. When the area ratio is increased further, the loops even change direction. For even larger area ratios the loops degenerate to little bumps in the curve (not shown).
More properties of the system can be shown using a simple model for section 2:

- The area change is modeled using the scattering notation:

$$\mathfrak{f}_d = A\mathfrak{f}_u + B\mathfrak{g}_d, \tag{5.8}$$

$$\mathfrak{g}_u = C\mathfrak{f}_u + D\mathfrak{g}_d. \tag{5.9}$$

- The open end and the duct at section 2 can be combined to one equation:

$$\mathfrak{f}_d = E \cdot e^{i\frac{\omega}{c}2\frac{L}{2}}\mathfrak{g}_d. \tag{5.10}$$

From these equations, the response $\mathfrak{g}_u/\mathfrak{f}_u$ of section 2 can be calculated to be:

$$\frac{\mathfrak{g}_u}{\mathfrak{f}_u} = C - \frac{AD}{B - E \cdot e^{i\frac{\omega}{c}2\frac{L}{2}}}. \tag{5.11}$$

The following items can be observed:

- For $E \cdot e^{i\frac{\omega}{c}2\frac{L}{2}} = B$, which here is the case for $\alpha = 1/8$ and $\omega^* = 2\omega_0, 4\omega_0, ...$, the response goes to infinity. This confirms the first considerations in this example.

- For small transmission coefficients A and D, the reflection coefficient C of the area change for section 1 dominates the response.

The effect of the decreasing transmission coefficients A and D can be seen as the decreasing radius of the smaller loop in figure 5.4 for the cut in section 2. For the cut in section 1, this effect is superposed by the singularity for $\alpha = 1/8$. In general the mapping scale, figures 5.2 and 5.3, exhibits peaks at the eigenfrequency of the section 2, when section 1 is cut and vice versa. Hence, a prediction of eigenfrequencies located in the section which is not cut by the Nyquist dummy may be impossible. This is especially the case, when parts of the system develop eigenmodes independently of the cut or if the system is strongly decoupled, e.g., as shown here, by area changes with a pronounced area ratio.

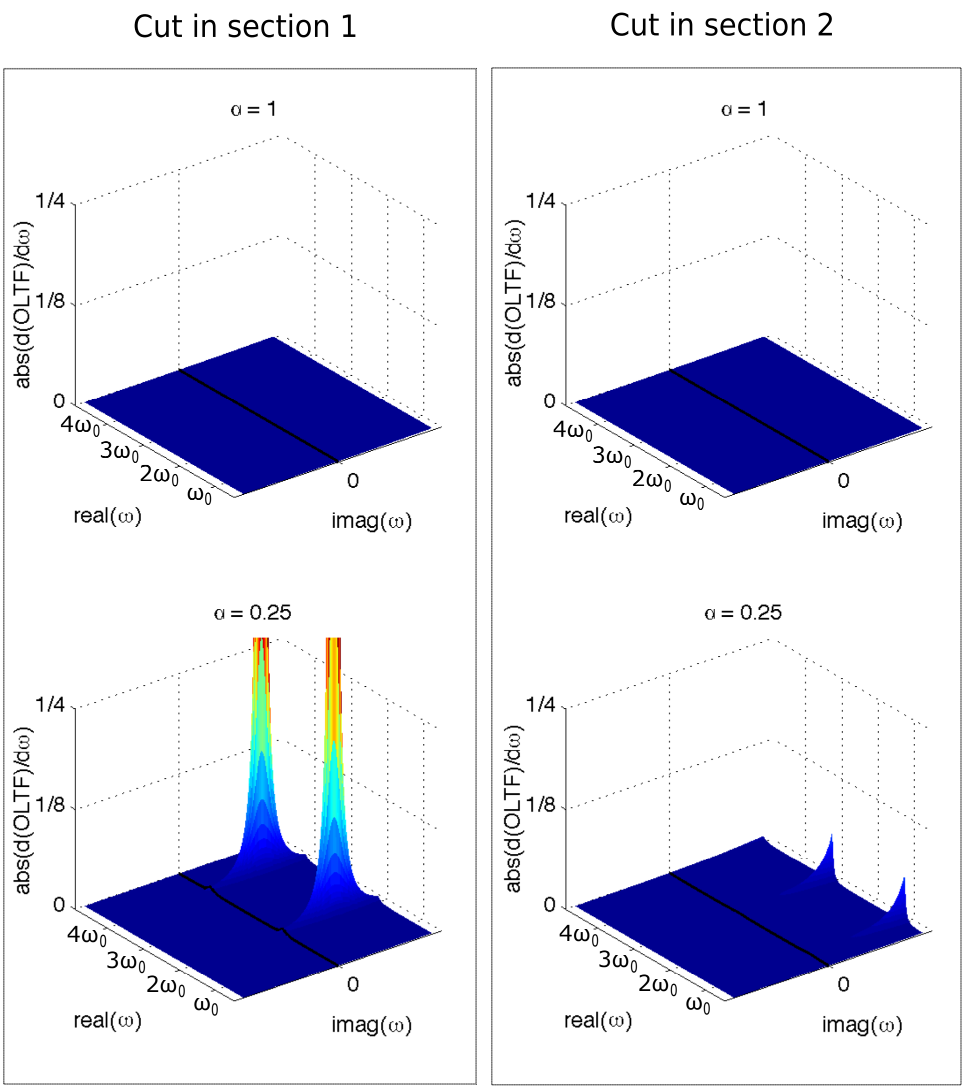

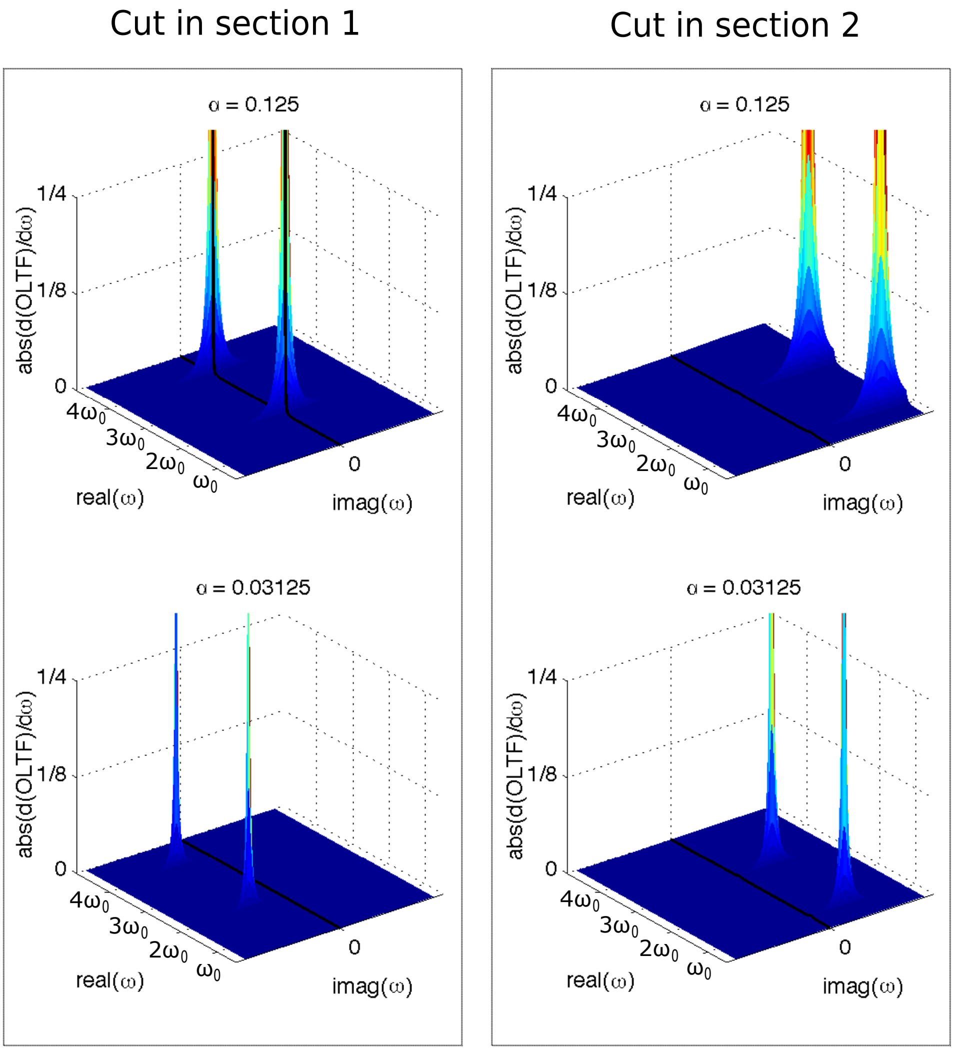

Figure 5.2: Magnitude of the derivative of the mapping function vs. the complex frequency of a duct - area change - duct system for different area ratios α. Left column: cut in section 1, right column: cut in section 2.

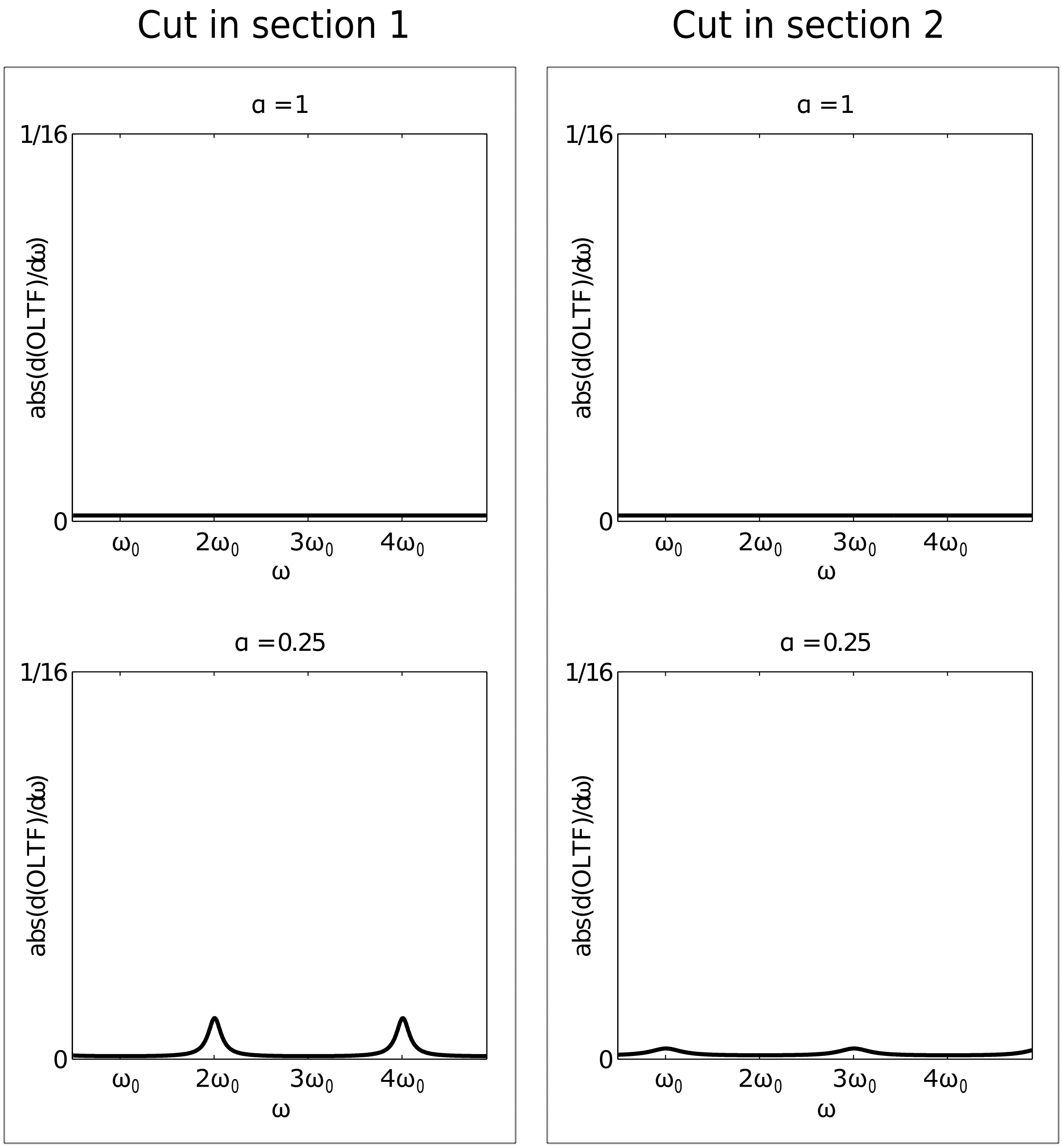
Cut in section 1
Cut in section 2
a =1
a =1
1/16
abs(d(OLTF)/dω)
0
ω0
2ω0
3ω0
4ω0
ω
a =0.25
a =0.25

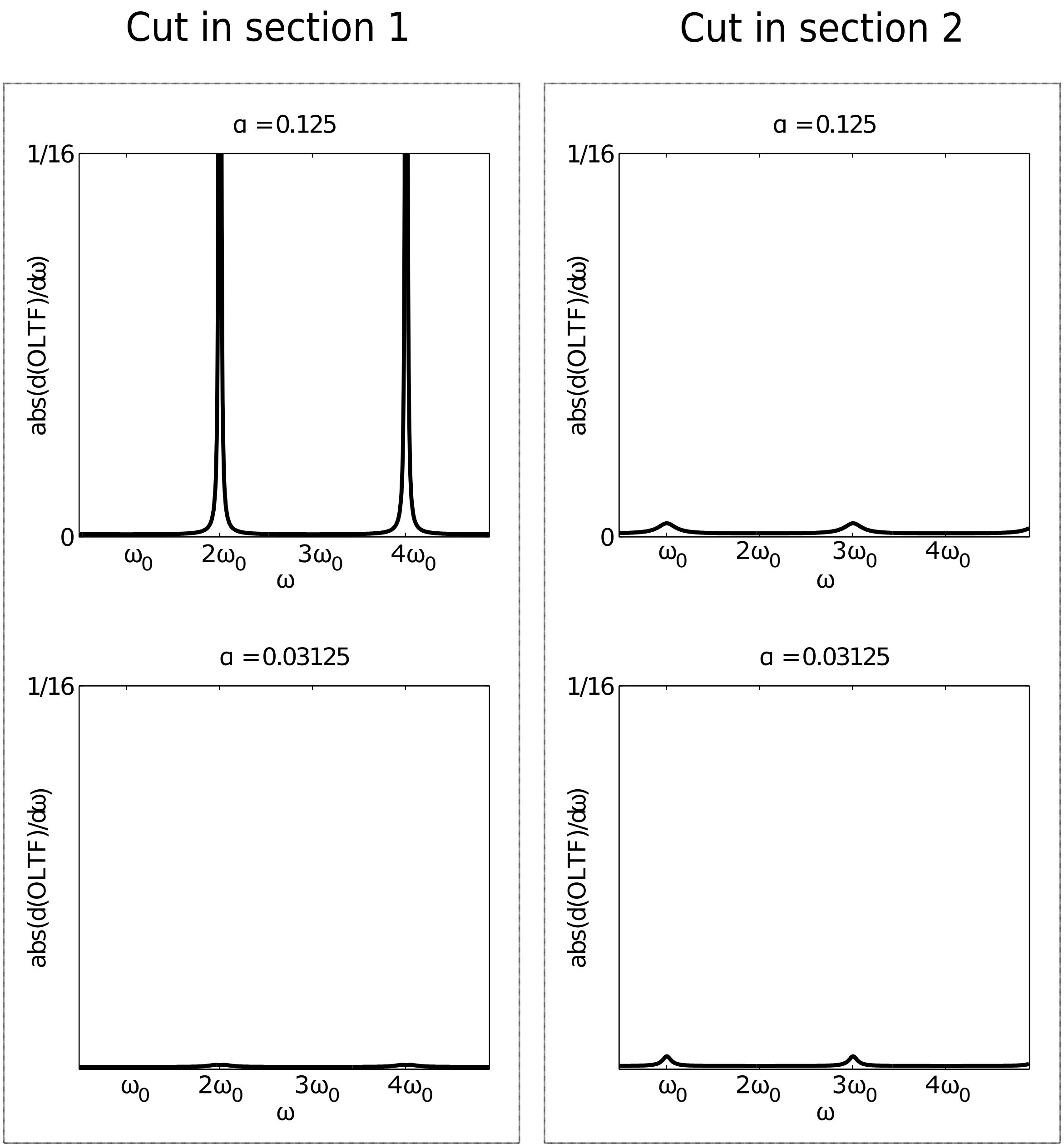

Figure 5.3: Magnitude of the derivative of the mapping function over the frequency ($\omega \in \mathbb{R}$) of a duct - area change - duct system for different area ratios α. Left column: cut in section 1, right column: cut in section 2. Corresponds to the black line in fig 5.2.

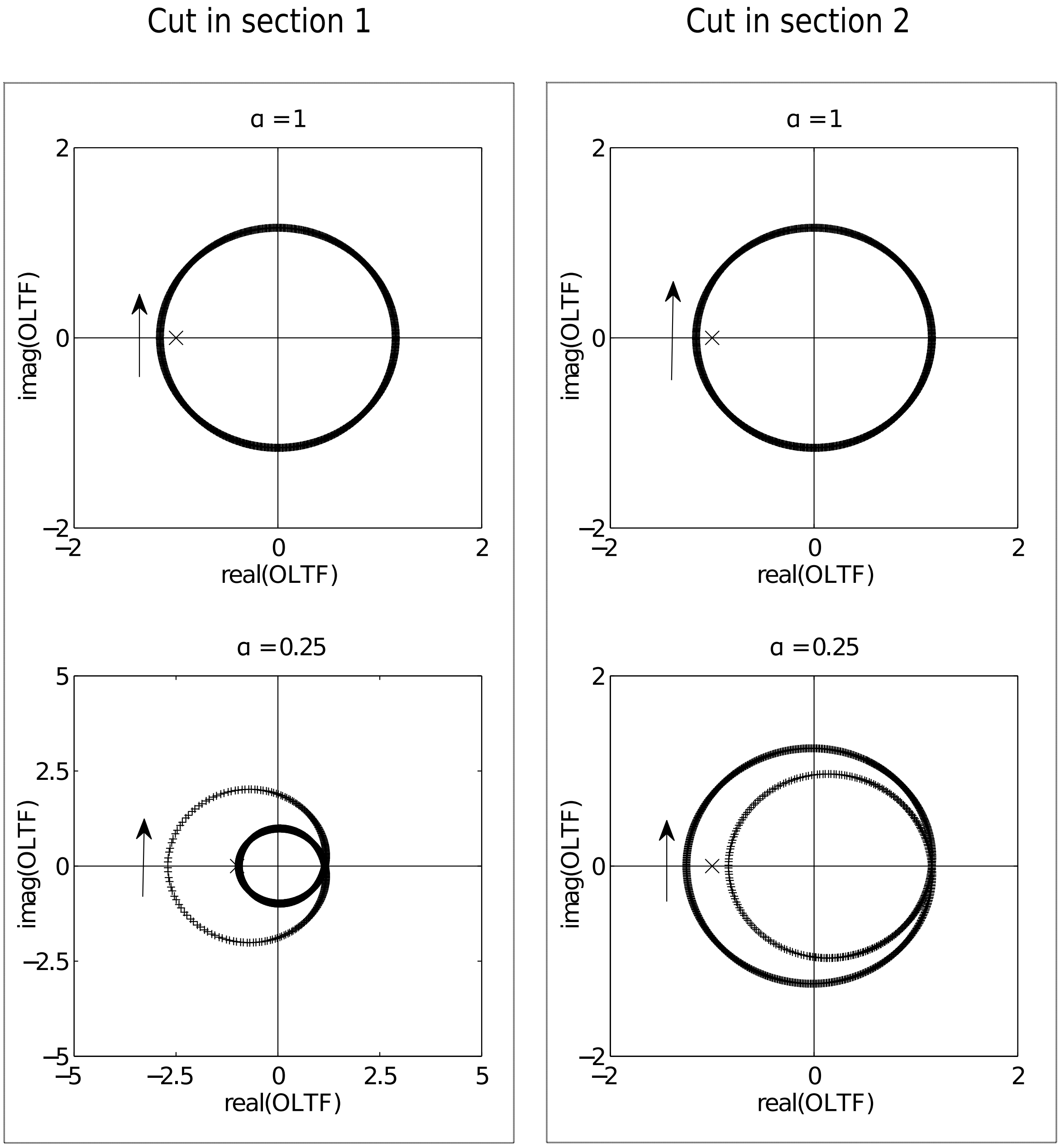
Cut in section 1
Cut in section 2
α =1
α =1
α =0.25
α =0.25
imag(OLTF)
real(OLTF)
2
0
−2
2.5
−2.5
5
−5

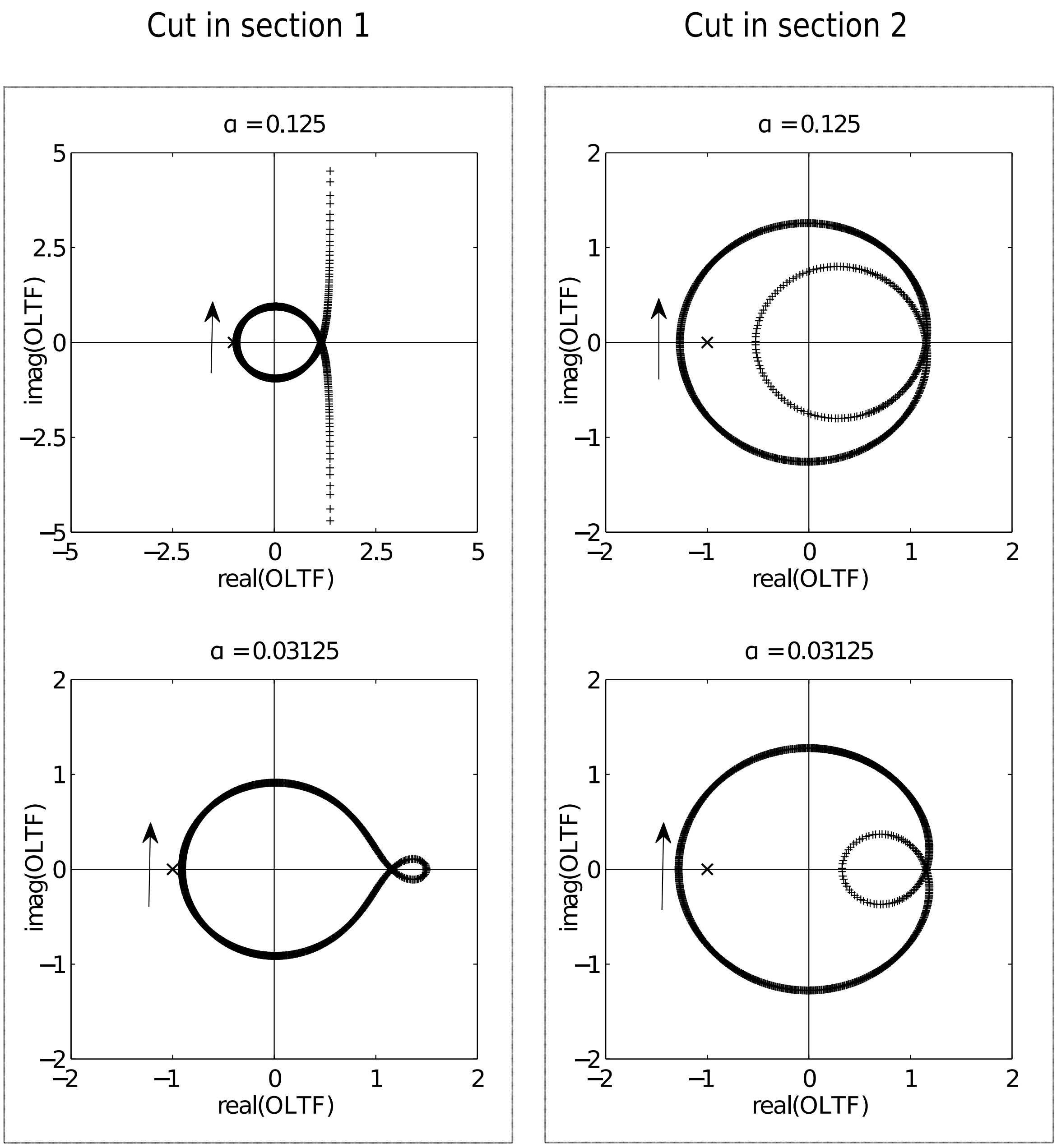

Figure 5.4: OLTF for a duct - area change - duct system for different area ratios. Left column: cut in section 1, right column: cut in section 2. Arrows indicate the sense of rotation of the curves with increasing frequency, the black "x" denotes the critical point.

5.4 Example 2: Acoustic Network with Bifurcation

Here, a system is constructed where a mode can develop in single parts of the system while not affecting other parts. The type of the mode determines, which parts of the system are affected. This case is formed by a duct of length $L = 0.5$ m with an open end. On the other side is a bifurcation, which connects the duct to two other ducts having half the cross sectional area A, both the same length $L = 0.35$ m and a closed end. The speed of sound is $c = 343$ m/s in the whole domain. The transfer matrix for the ideal bifurcation element can be expressed by the following equations,

$$p_i = p_j \tag{5.12}$$

$$p_i = p_k \tag{5.13}$$

$$S_i u_i = S_j u_j + S_k u_k. \tag{5.14}$$

Figure 5.5 shows the set-up of the network model. Two different locations for the cut for the Nyquist curve are chosen, one in the main branch of $L = 0.5$ m and one in one side branch of $L = 0.35$ m.

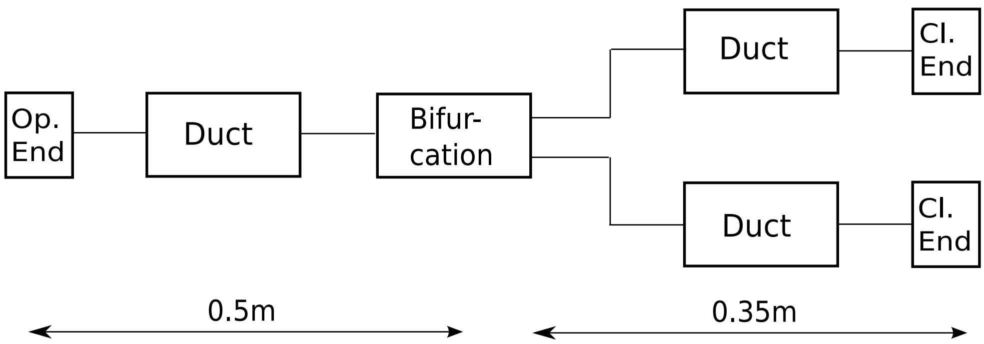

Figure 5.5: Sketch of the network model of the bifurcation.

The first eigenfrequency between the two 0.35 m branches is of special interest here and therefore denoted ω_0.
The eigenfrequencies of the two calculations are summarized in table 5.1. Two frequencies are not detected when the cut is applied in the main branch compared to the side branch: $\omega^* = \omega_0$ and $\omega^* = 3\omega_0$. These two frequencies correspond to the $\lambda/2$ and $3\lambda/2$ eigenmode of the 0.7 m duct. This implies that these frequencies belong to the mode between the two side branches.

ω^*/ω_0 for cut in side branch	0.35	1	1.35	2	2.82	3	3.94
ω^*/ω_0 for cut in main branch	0.35	-	1.35	2	2.82	-	3.94

Table 5.1: Eigenfrequencies ω^*/ω_0 determined with the Nyquist methods for two different locations of the cut

The two modes share the property that they have vanishing pressure fluctuation at the bifurcation point. In contrast, the $2\lambda/2$ mode has a pressure-maximum there and hence couples with the main branch. Therefore, it can be also detected in the main branch. A frequency of $\omega^* = 2\omega_0$, which would correspond to the expected frequencies, is detected by both configurations. Figure 5.6 illustrates this.

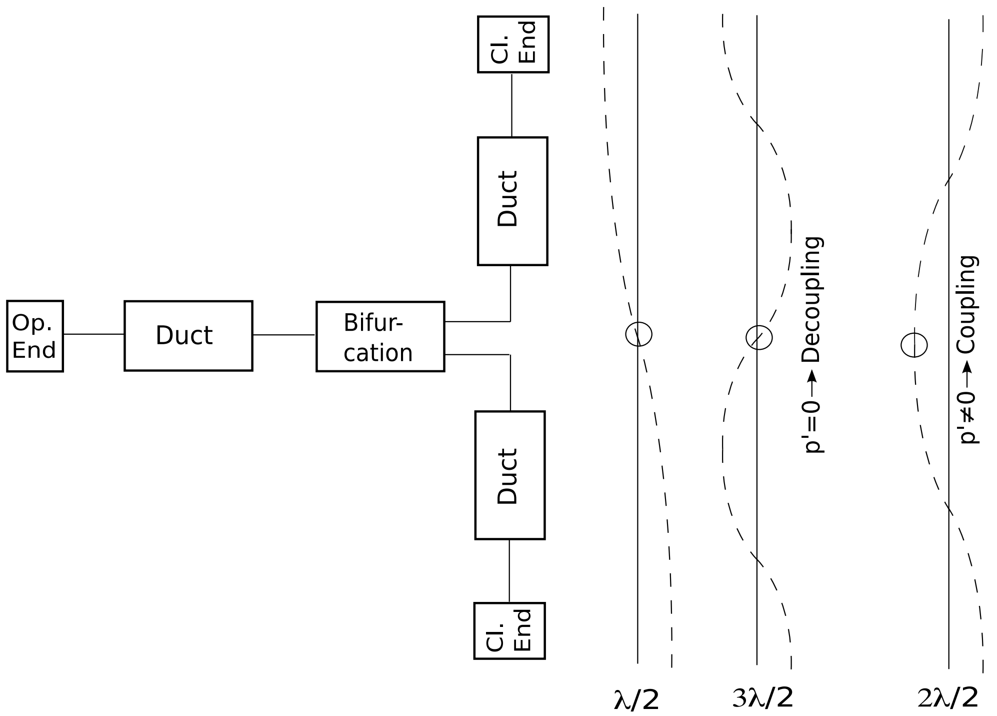

Figure 5.6: Sketch of the eigenmodes in the side branches.

As in the first example, the Nyquist method is only capable of predicting those modes that are localized in areas, where the cut is applied. In contrast to the first example, the decoupling here is so well pronounced, that the Nyquist curves do not even show any anomalies around the missed eigenfrequencies. Of course, this example is even more academic than the one before, but shows very well the effect of placing the cut at the wrong place.

5.5 Conclusions and Recommendations

The last two examples have shown the limitations of the CNN method. In has become obvious that the location of the cut is of crucial importance for this method. Therefore, before using Nyquist methods, one should carefully examine the system for the type and location of the eigenmodes and place the cut at a position where it intersects the modes. The example in 5.4 has shown that modes that develop in parts of the system, which are not affected by the cut, are not necessarily visible in the Nyquist curve.
In case the Nyquist curves exhibit singularities, one can take advantage of the knowledge of the frequency, where the singularity occurs in order to find the corresponding mode.
Indicators for singularities have been addressed in 5.2. In general, strongly branched systems, as well as systems exhibiting strong area changes or other decoupling elements, should be handled with care. Another conclusion which can be drawn from these examples is the fact that introducing non-reflecting terminations, either artificially, e.g. from the cut of the Nyquist method, or naturally (see 6.1), does not prevent systems from developing instabilities.
Hence, instabilities can occur even when non reflecting terminations are present and instabilities do not necessarily affect the entire system, but may be present only in locally limited parts.

6 Application

In the following chapter, the CNN method is applied to two test cases. The first test case is a laminar premix perforated plate burner, the second one a turbulent premix swirl burner.

6.1 Laminar Test Case: The Matrix Burner

6.1.1 Geometry and Thermo-Acoustic Properties

After Kopitz et al. [46], who applied the CNN method to a Rijke tube, a more challenging configuration for the validation of the CNN method is a laminar multi flame burner examined by group EM2C at Ecole Centrale Paris [60–62]. Results for the CNN method were generated at the CTR Summer Program 2008; there is a comprehensive description in the proceedings [36], which is the basis for this chapter. More consideration can be found in [34]. The geometry of the burner is sketched in Figure 6.1. The burner consists of a plenum

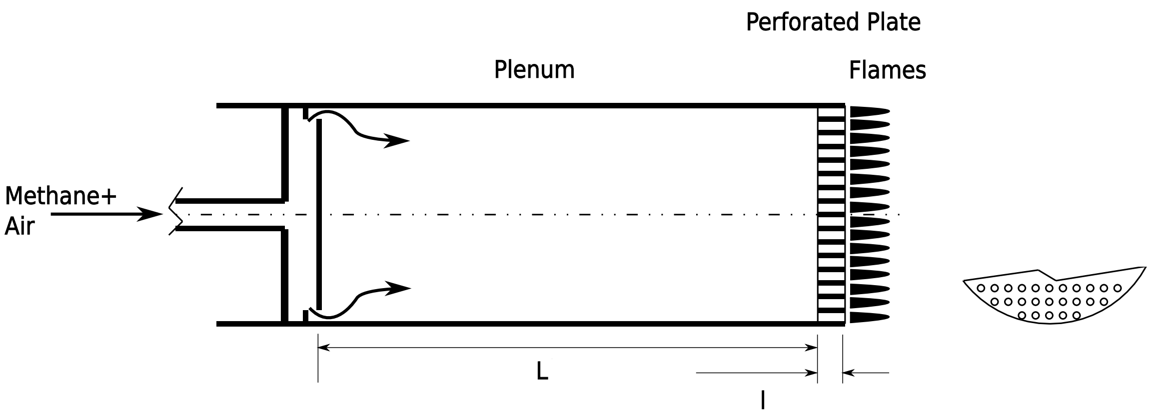

Figure 6.1: Scheme of the laminar premix burner from Ecole Central Paris.

of diameter $D = 0.2\,\mathrm{m}$ which is closed by a piston on the upstream end and whose length L is therefore variable ($L = 0.09...0.85\,\mathrm{m}$). The downstream end of the plenum is formed by a perforated plate of thickness l. Noiray et al. examined different plates, but for the application here, we restrict ourselves to a plate having 420 holes of 2 mm diameter, $l = 30\,\mathrm{mm}$ and, hence, an aperture ratio of 0.34. 420 small conical flames are formed and stabilized on the downstream side of the perforated plate, which is not further confined. The burner is operated using a methane-air mixture of equivalence ratio $\phi = 0.85$ and a mass flow of $\dot{m} = 5.4\,\mathrm{g/s}$. Depending on the length of the plenum, unstable eigenmodes of different frequencies develop for some parameter configurations, other configurations are stable. The eigenmodes correspond to the first quarter-wave-eigenmodes of the plenum. The stability map is shown in figure 6.2.

For the CNN approach, the geometry is divided into a CFD and a network

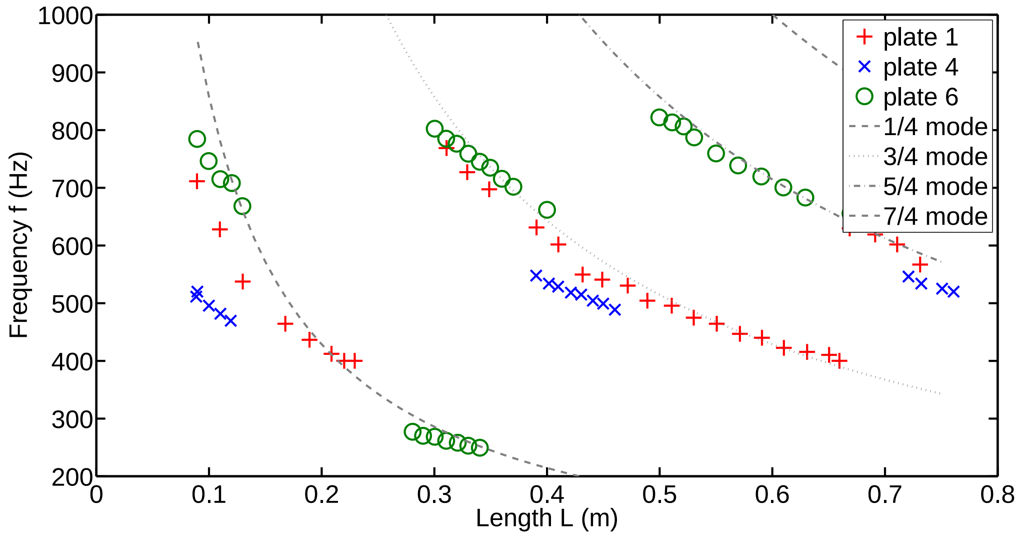

Figure 6.2: Stability map of the laminar premix burner experimentally determined by Noiray et al. [60], plot from [36]. The present configuration uses plate 4.

domain. The CFD domain comprises a part of the perforation and the flame, while the network domain contains the plenum and the inflow to the perforated plate. This set up permits the CFD to be used for the flame-acoustics interaction, while the flexible network model is used for the various lengths of the plenum. The separation into network and CFD domain is sketched in figure 6.3

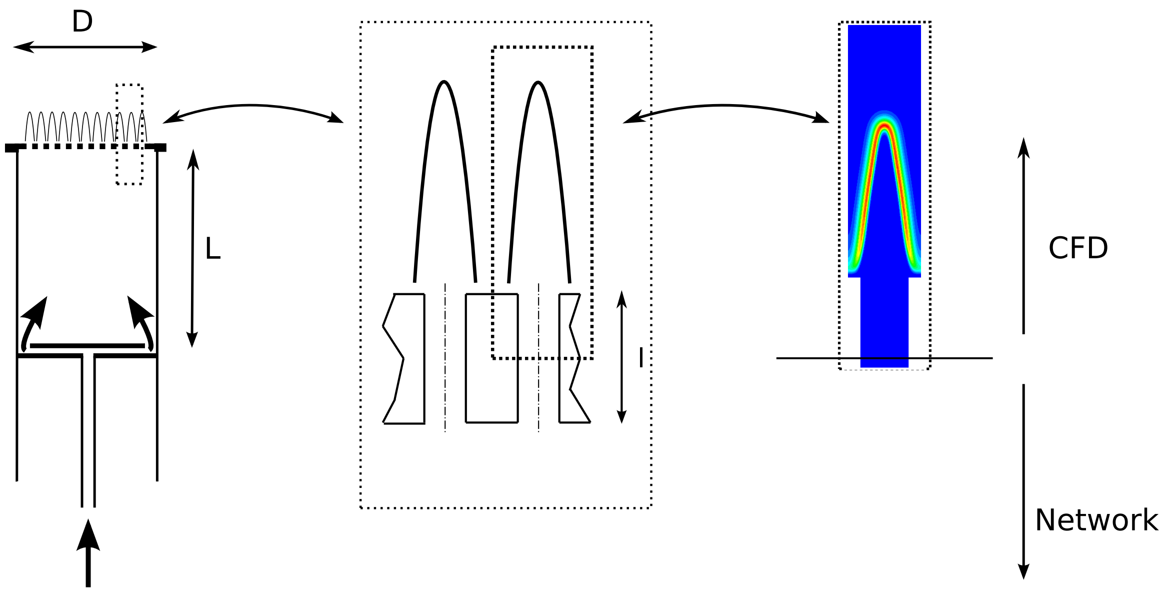

Figure 6.3: Decomposition of the burner into CFD and network domain.

6.1.2 Analysis with Network Model Based on Measured FTF

Prior to the application of the CNN method, the configuration is examined using a pure network model approach. Noiray et al. have presented considerations about the modelling in the work mentioned above, a summary can be found in [60]. The modelling used here can be found in detail in [36] and [34]. Here, a brief overview is given. Assuming a constant pressure and incorporating the effect of the area change at the end of the perforated plate, the flame can be modeled similarly to the equation for the flame in 2.7 using the following equation:

$$\begin{pmatrix} \rho_i c_i & \rho_i c_i & \rho_j c_j & \rho_j c_j \\ A_i & -A_i & A_j(1+nFTF) & -A_j(1+nFTF) \end{pmatrix} \begin{pmatrix} \mathfrak{f}_i \\ \mathfrak{g}_i \\ \mathfrak{f}_j \\ \mathfrak{g}_j \end{pmatrix} = 0. \tag{6.1}$$

The FTF measured by Noiray et al. [60,62] (see figure 6.4) is approximated with a model involving two time lags [50, 97],

$$FTF = (1+a)e^{(-i\omega\tau_1-\omega^2\sigma_1^2/2)} - ae^{(-i\omega\tau_2-\omega^2\sigma_2^2/2)}, \tag{6.2}$$

with $a = 0.906$, $\tau_1 = 0.912\,\text{ms}$, $\tau_2 = 1.22\,\text{ms}$, $\sigma_1 = 0.334\,\text{ms}$ and $\sigma_2 = 0.817\,\text{ms}$. Figure 6.5 shows the network model of the laminar premix burner. The out-

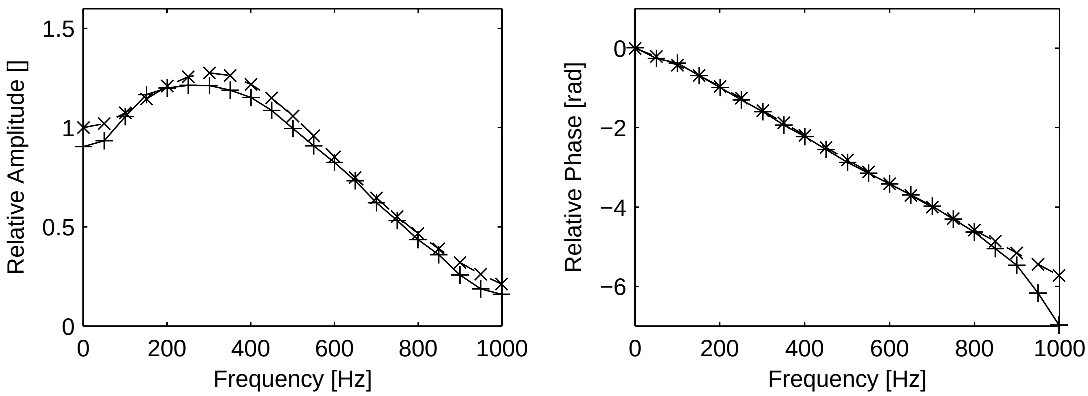

Figure 6.4: FTF of the laminar premix burner, left amplitude, right phase. Solid +: measurement ([60], Fig. 4.5, $\phi = 0.86$, $\dot{m} = 5.4\,\text{g/s}$). Dashed x: approximation using equation 6.2.

let boundary is non-reflecting, the area change involves acoustic losses. The length of the plenum can be easily varied by changing the length of the simple duct. The cut for the Nyquist curve is located within the perforated plate. A location inside the plenum yields similar results (not shown). Obviously, a location of the cut between flame and non-reflecting outlet would result in a zero response for all frequencies. For simplicity reasons, the eigenfrequencies ob-

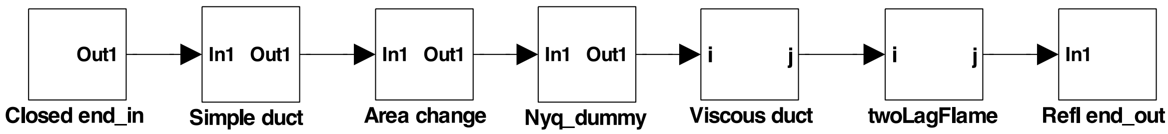

Figure 6.5: Network model of the laminar premix burner for TaX, based on Matlab Simulink.

tained here represent the minimum distance between curve and critical point. This criterion can easily be evaluated numerically. No polynomial fit or scaling correction is applied. Due to a considerable error in the prediction of stability, acoustic losses at the area change have been introduced and adapted, so the stability properties match the experiment ($\zeta = 54$). The plausibility of this value is discussed further in 6.1.3.3. Similar results can be obtained by changing the reflection coefficient at the inlet to values as low as $\hat{\mathscr{R}} \approx 0.2$. This value is too far from the estimated value to be considered the only source for the missing damping. If the damping is not adapted, the distance between critical point and Nyquist curve becomes very large. This leads to large insecurities in the prediction of the eigenfrequency. This problem is known in this case and will be discussed later. The results are plotted in figure 6.6.

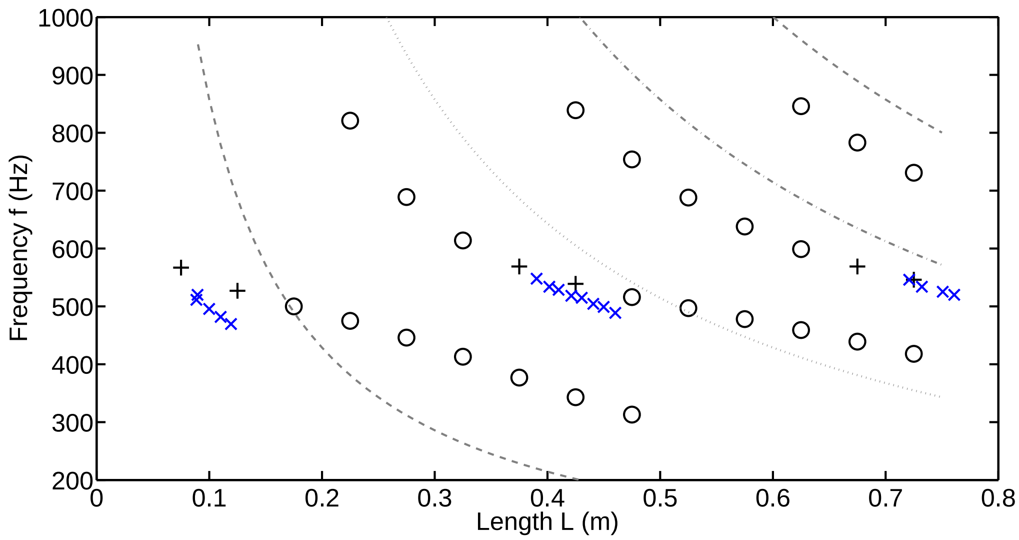

Figure 6.6: Stability map of the laminar premix burner using a network model with estimated parameters for the acoustic losses. Black +: predicted unstable, black o: predicted stable, blue x: experimentally unstable, grey lines: $\lambda/4$-modes.

In general, an application of the CNN method for this case seems to be feasible and no major problems are expected.

6.1.3 Analysis with CNN Approach

6.1.3.1 Mesh

One single flame is simulated in the CFD using symmetry boundary conditions, which corresponds to the assumption of an infinite array of flames. Despite its small physical size, the domain has around 470,000 cells due to the requirement to resolve flow and flame properly. The mesh is structured, which is not a necessary requirement for the solver, but permits a very controlled meshing process in this basic geometry. Due to the great amount of cells and the small physical size, the simulation is resolved on DNS level and a 1-step global mechanism for the reaction can be used without any artificial thickening. For the frequency range of interest, no significant numerical dissipation is expected due to the fine grid. Figure 6.7 shows the concept of the mesh. The

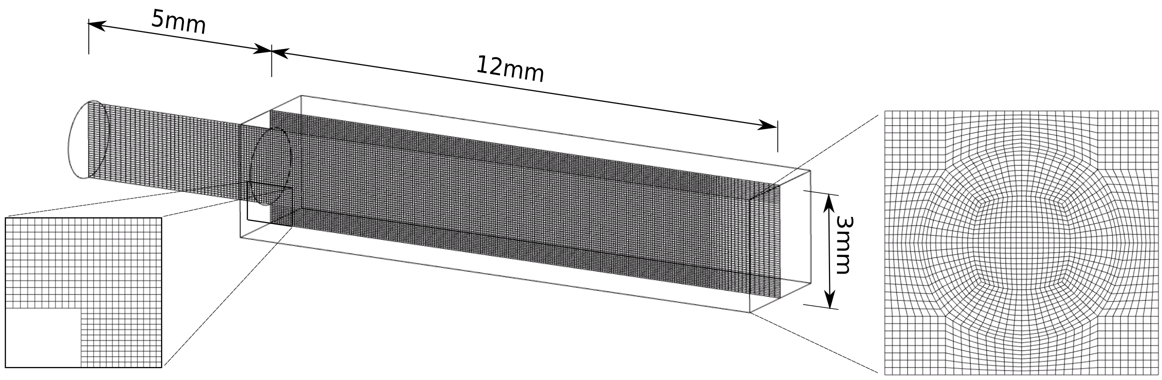

Figure 6.7: Mesh for the CFD simulation of the laminar premix burner.

downstream end of the domain is formed by a non-reflecting outlet boundary condition, which simulates the free field for the unconfined flames. It shall be mentioned here that this burner presents an example where an instability can develop even with a non-reflecting boundary on one side. Here, the non reflecting part is not introduced by the cut of the CNN method, but is physical due to the free field. Nevertheless, the instability is not prevented even by the missing feedback directly on one side of the flame. This confirms the discussion in 5.
Figure 6.8 shows an axial slice through the domain with a contour plot of the reaction rate indicating the position of the flame. The walls are set to

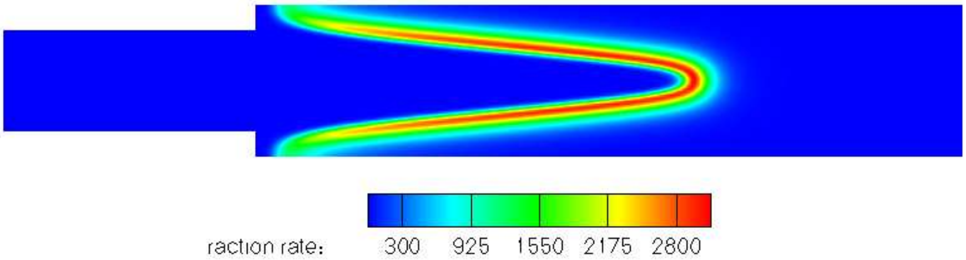

Figure 6.8: Axial slice of the CFD domain, contour plot showing the reaction rate. Plot similar to [34].

isothermal no-slip walls at 350K. Excitation is imposed at the upstream end, a non-reflecting velocity inlet boundary condition. A parabolic velocity profile is imposed for the mean flow. The excitation signal is a pseudo random binary noise, which has been low pass filtered. This signal is imposed in a block profile. After initialisation 1,200,000 iterations at a time step of $3.5 \cdot 10^{-8} s$ are calculated on 80 cores of HLRB II at LRZ computing centre, Munich. Postprocessing is done using a correlation based algorithm, see 2.8. See [36] for details about the configuration.

6.1.3.2 Acoustic Properties of the CFD Domain

The numerical configuration was checked for singularities ("resonant amplification") and no substantial problems are expected [36]. Using the data, especially the FTF available from the experiments of Noiray et al., a preliminary check of the expected part loop transfer function, i.e. the acoustic response of the CFD model (including the flame), was set up using the TaX network tool. Figure 6.9 shows the corresponding configuration.

The part loop transfer function obtained using this model is shown in figure 6.10 and does not exhibit properties that suggest strong singularities.

Figure 6.11 shows the results for the transfer function of the CFD domain. A good agreement with the expected behaviour (see figure 6.10) can be observed.

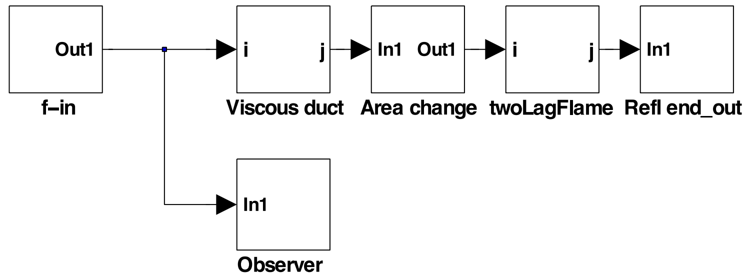

Figure 6.9: Network configuration for the preliminary check of the acoustic properties of the CFD domain of the laminar premix burner, using TaX, based on Matlab Simulink

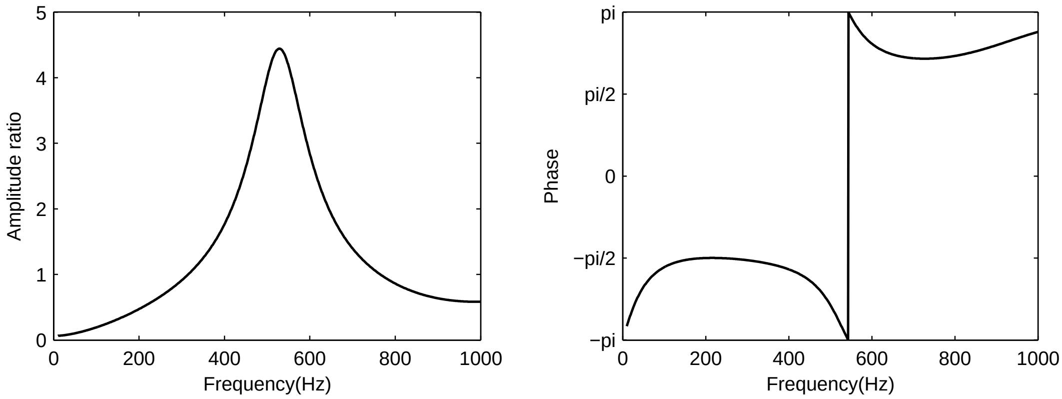

Figure 6.10: TaX network result for the expected part loop transfer function of the CFD model of the laminar premix burner.

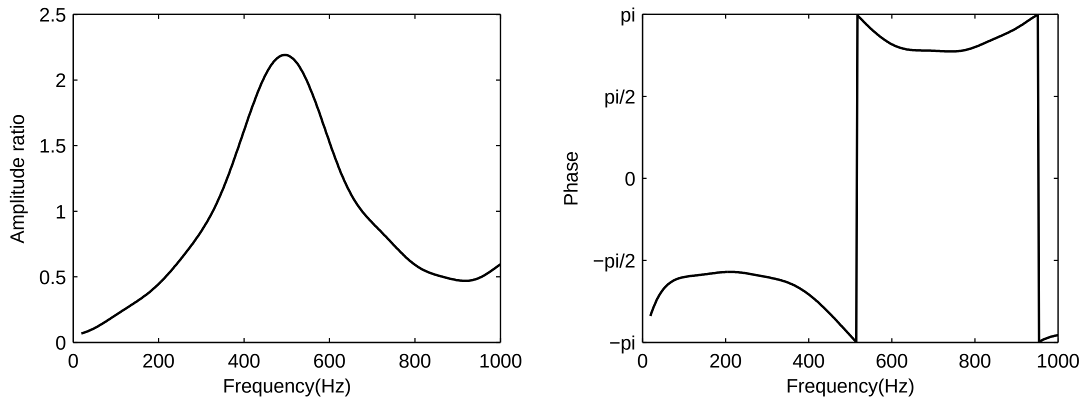

Figure 6.11: Part loop transfer function of the CFD domain of the laminar premix burner, right diagram: amplitude, left diagram: phase.

6.1.3.3 Network Domain

The network domain is formed by the piston (closed end, equation 2.106), the plenum (simple duct, equation 2.85), the inflow to the plate (area change, equation 2.95) and the perforation (duct with viscous effects, equation 2.104). Figure 6.12 shows the network model in TaX. The Nyquist Dummy is modified to incorporate the results from the CFD. Acoustic losses at the inflow of

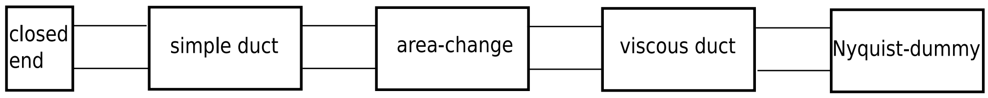

Figure 6.12: Network model of the network-part of the laminar premix burner.

the perforation have been determined using CFD. The domain was identical to the configuration described above, but the flow direction was reversed, no combustion was active and statistically independent excitation was imposed at both sides. Postprocessing yields an effective length of $l_{\mathrm{eff}} = 7.64 \cdot 10^{-}4\,\mathrm{m}$ and a loss coefficient of $\zeta = 6$.
Literature ([30], p.404) offers values of $\zeta \approx 10$ for long thick perforates. However, these values for perforates are given for Reynolds numbers of $Re > 10^5$, while in the present configuration $Re \approx 1000$. Additionally, the values have to be corrected, because they refer to the upstream velocity, and the model used here to the velocity in the perforate. Therefore, the value has to be corrected with the square of the velocity and, hence, with the aperture ratio $1/0.34^2$ The value is therefore $\zeta \approx 1$, which is much lower than the value obtained by postprocessing the CFD results. For low Reynolds numbers as it is the case here, values for porous layers may apply. According to [30], p.414, loss coefficients of $\mathcal{O}(\zeta) = 10$ can be estimated for $Re \approx 1000$ and grains with diameters of less than 10 mm. These also have to be corrected, and in the notation used here, again a value of $\zeta \approx 1$ is obtained.

6.1.3.4 Results

The combination of CFD result and network model permits both eigenfrequencies and stability to be determined. Additionally, by regarding the distance between Nyquist curve and critical point, the growth rate can be estimated. The stability map of the burner configuration using these parameters is plotted in figure 6.13. The model remarkably over-predicts the unstable ar-

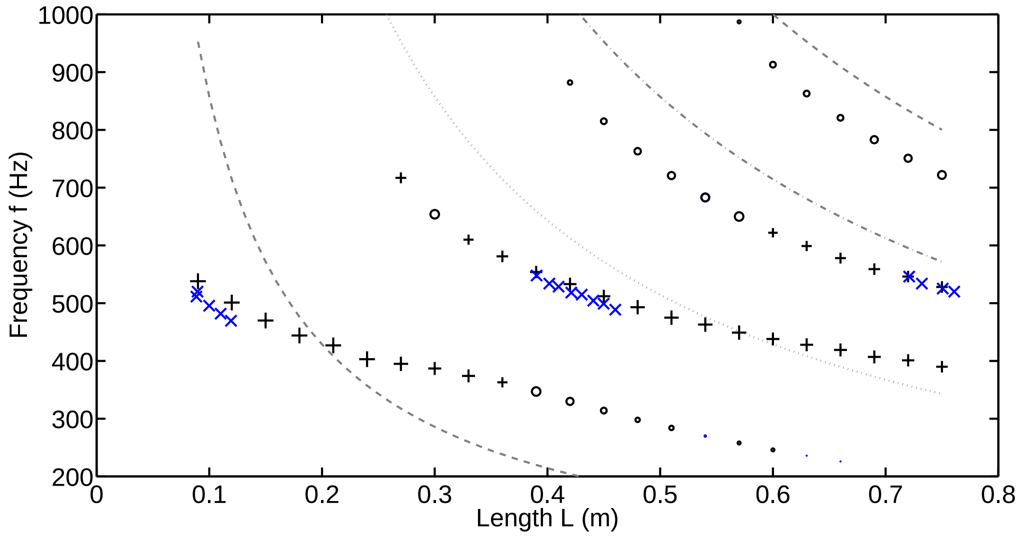

Figure 6.13: Stability map of the laminar premix burner using the estimated parameters for the acoustic losses, from [36]. Black +: predicted unstable, black o: predicted stable, blue x: experimentally unstable, grey lines: $\lambda/4$-modes.

eas. The flame transfer function obtained using the simulation [34, 36] does not exhibit remarkable differences compared to the one obtained experimentally by Noiray [60] which could explain this discrepancy. The frequencies are well predicted at the same time. Therefore, the overestimation of the instabilities is likely to be explained by the suboptimal modeling of the acoustic losses. Possible reasons for this are given in the discussion. Using adjusted acoustic losses at the area change ($\zeta = 42$) which are significantly higher than the estimated ones, the zones of instability are reproduced with good agreement (see figure 6.14). The value of $\zeta = 42$ is high compared to the value of 6 obtained numerically and the value for perforates or porous media according to [30]. Again, as for the analysis with Network model, a reflection coefficient of $\hat{\mathscr{R}} \approx 0.2$ would lead to the same stability properties as the increase of the losses at the perforation. In both cases, the losses have to be increased by half an order of magnitude.

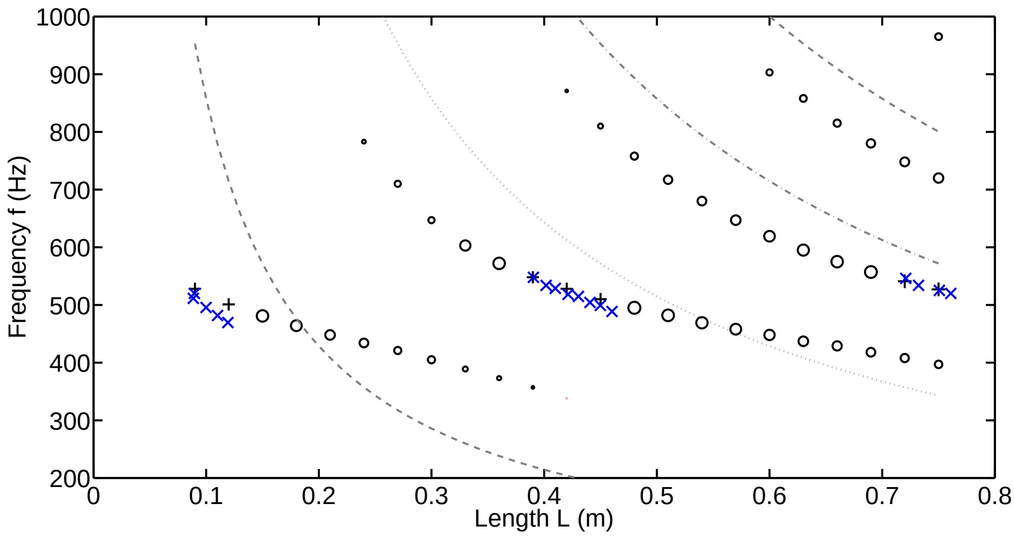

Figure 6.14: Stability map of the laminar premix burner using the adjusted parameters for the acoustic losses, from [36]. Blue +: predicted unstable, blue o: predicted stable, black x: experimentally unstable, grey lines: $\lambda/4$-modes.

6.1.4 Conclusion

The eigenfrequencies are well reproduced, while there is a considerable error in the estimation of the acoustic damping and therefore in the stability-instability distinction and in the growth rates. Several reasons may explain this observation:

- Simulating only one flame with symmetry conditions neglects losses of the outer flames, where part of the acoustic energy is lost to the side.
- In the simulation the mean velocity is imposed with a parabolic profile, which is physical. The acoustic excitation in the simulation does not exhibit any special profile, but a pure block profile. This is probably not correct, as there are considerable effects of the Stokes boundary layer in the duct. This might affect the shape of the wave front reaching the flame. There is no possibility implemented in the boundary conditions to account for a profile in the excitation signal.

- The low order models of the viscous duct and the losses at the area change may not be accurate. There may be a difference between a single hole and a perforated plate. The values in Idelchik [30] for perforated plates do not include cases with small Reynolds numbers.

- There might be losses at the piston which is considered perfectly reflecting here, but in reality includes the inflow devices. Analyses with network models show that the reflection coefficient would have to be as low as $\hat{\mathscr{R}} \approx 0.2$ to be responsible for the deviation in stability alone.

It was not possible to identify a clear reason for the erroneous results. A combination of losses mainly at the perforation and due to non-perfect reflection at the inlet is most likely the cause.
Nevertheless, there is no indication for the assumption that the errors are due to bad mapping in the Nyquist curve. The discrepancies in the damping are therefore part of the uncertainties present in the modeling and are not due to defects in the CNN approach itself or the Nyquist stability analysis.

6.2 Turbulent Test Case: The BRS Burner

The validation of the method presented in this work shall be done using a premix swirl burner. At the Lehrstuhl für Thermodynamik the "Beschaufelter RingSpalt" (BRS) burner (an axial vane swirler in a conduit of annular cross section) has been thoroughly investigated experimentally and numerically using RANS. The burner is designed for the investigation of the influence of swirl fluctuations on combustion and therefore has variable swirler positions. As the influences of the swirler position are not the focus of the present work, the swirler position is fixed for the cases studied here. The burner has thermo-acoustic stability properties which make it an interesting subject for the CNN method: It can be fitted with combustion chambers of two different lengths. For the short combustion chamber, the burner is stable. When the long combustion chamber is mounted, it exhibits instability for several operating points. This dependency on the length of the combustion chamber is

well suited for the application of the CNN method, since the flame and all elements upstream of the flame are not affected by the change of the length of the combustion chamber. Details about stability and geometry are given in the following sections.
The approach presented in this thesis should be able to capture the influence of geometrical modification which can be easily modeled by network elements. Therefore, two configurations are compared here which differ in the length of the combustion chamber. This permits the expensive LES of the upstream part of the burner and the flame to be used to evaluate the stability of two configurations. The partitioning is sketched in figure 6.15. Different LES Calculations are only required for different operating points, but not for the geometrical modification. Due to the good experiences obtained with the

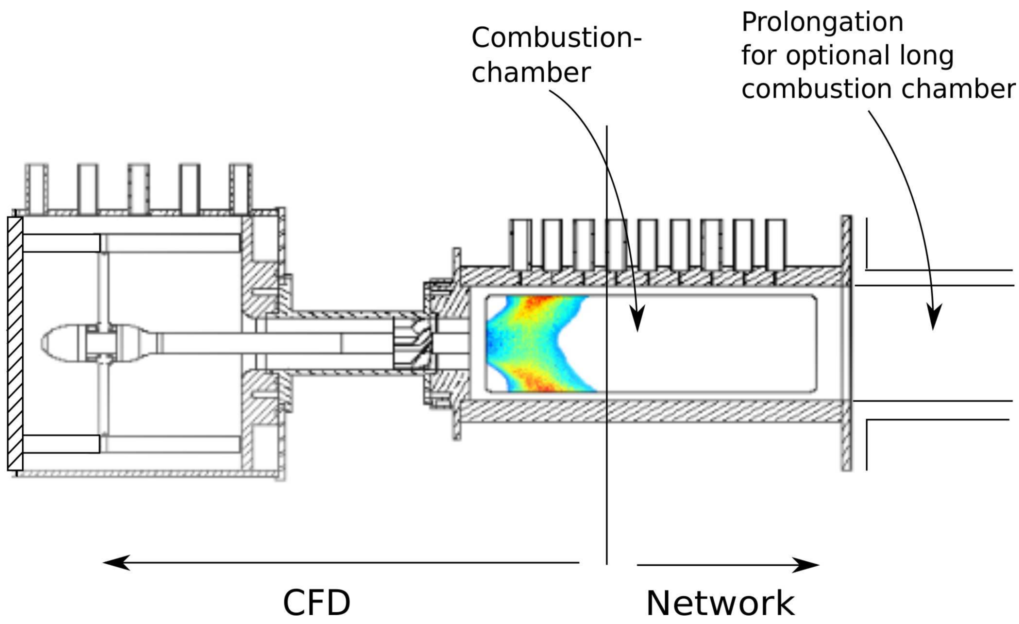

Figure 6.15: Partitioning of the BRS burner test rig into CFD and Network domain.

CNN method in the first example, the laminar perforated plate burner, the BRS burner example was directly examined using the CNN method.

6.2.1 Geometry

The burner consists of a plenum of 169.4 mm length and 200 mm diameter, an axial swirler of 30 mm length located within a duct of 180 mm length and a diameter of 40 mm containing a lance of 16 mm diameter. This is followed by the combustion chamber, which has a square cross section of 90 mm edge length and a length of 300 mm in the short configuration and 700 mm in the long configuration. Hence, there are area ratios of $\alpha = 29.9$ and $\alpha = 1/(7.7)$ at inlet and outlet of the swirler tube respectively.
Figure 6.16 shows the swirler module from two different angles. The entire configuration for the short combustion chamber is shown in figure 6.17.

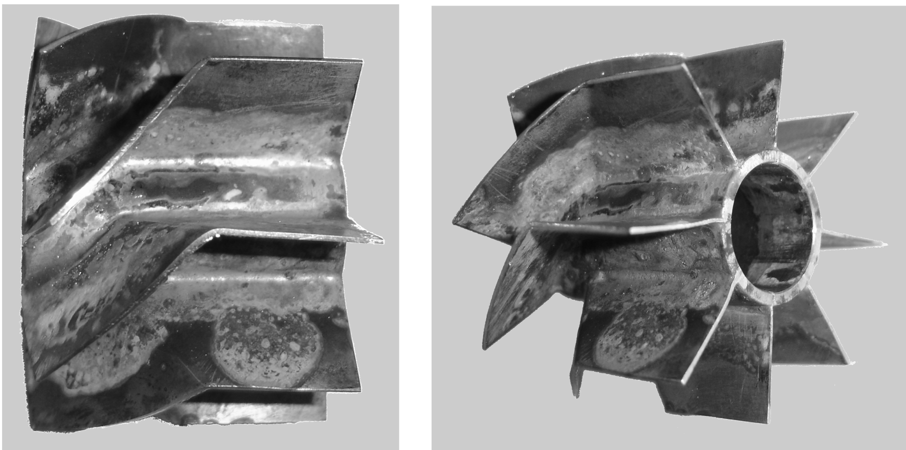

Figure 6.16: Swirler module of the BRS burner photographed from two different angles. Flow direction from right to left

The inflow to the plenum is realized through a sinter metal plate, which corresponds to a hard velocity inlet. The outlet at the end of the combustion chamber is covered by a plate having 6 holes of 20 mm diameter arranged in a circle. The acoustic properties of the plate have been measured in experiments.

6.2.2 Stability

The stability properties of the BRS burner have been evaluated in experiments by Komarek [42, 43] for 30 kW, 50 kW and 70 kW power and air ratios λ of 1.1,

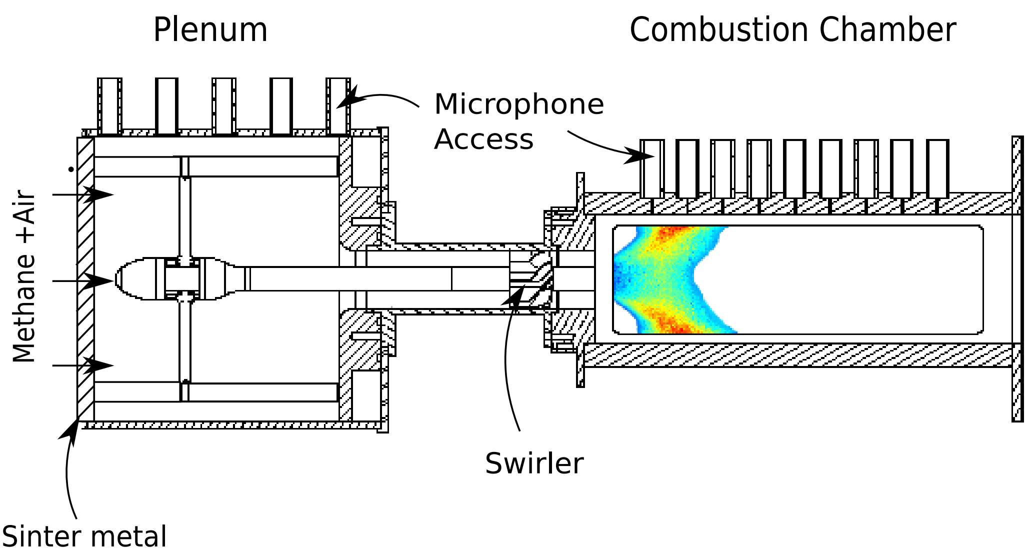

Figure 6.17: Sketch of the BRS burner test rig.

	$\lambda = 1.1$	$\lambda = 1.3$	$\lambda = 1.5$
$P = 70\,\mathrm{kW}$	unstable	stable	stable
$P = 50\,\mathrm{kW}$	unstable	unstable	stable
$P = 30\,\mathrm{kW}$	unstable	unstable	unstable

Table 6.1: Stability map for the long combustion chamber.

1.3 and 1.5 for both short and long combustion chamber. The stability maps for long and short combustion chamber are shown in tables 6.1 and 6.2.

The frequencies of the dominating unstable frequency are given in table 6.3. Growth rates are not available due to the difficulty to measure them properly. The following configurations are chosen for validation of the CNN method: $P = 70\,\mathrm{kW}$, $\lambda = 1.3$; $P = 70\,\mathrm{kW}$, $\lambda = 1.1$ and $P = 50\,\mathrm{kW}$, $\lambda = 1.3$. The reason for this choice is the good quality of experimental data for the two 70 kW cases.

	$\lambda = 1.1$	$\lambda = 1.3$	$\lambda = 1.5$
$P = 70\,\mathrm{kW}$	stable	stable	stable
$P = 50\,\mathrm{kW}$	stable	stable	stable
$P = 30\,\mathrm{kW}$	stable	stable	stable

Table 6.2: Stability map for the short combustion chamber.

	$\lambda = 1.1$	$\lambda = 1.3$	$\lambda = 1.5$
$P = 70\,\text{kW}$	145.775	stable	stable
$P = 50\,\text{kW}$	137.5	141.925	stable
$P = 30\,\text{kW}$	107.25	101.275	94.7

Table 6.3: Stability map for the long combustion chamber, frequency of the unstable modes in [Hz].

The 50 kW case has advantages because the CFD simulation can be initialized well from the $\lambda = 1.3$, $P = 70\,\text{kW}$ case. In two of the validation cases, the stability depends on the length of the combustion chamber.

6.2.3 Analysis with CNN Approach

6.2.3.1 Domain and Mesh

The entire Geometry of the BRS test rig has been described in section 6.2.1. The computational domain covers the plenum, the swirler and a 200 mm section of the combustion chamber. The length of 200 mm is a compromise between providing sufficient space for the flame and saving computational power. The meshes were generated using the commercial software "Gambit" by Ansys Inc., Canonsburg, PA, USA, and the CFD-Solver used is "AVBP" by Cerfacs, Toulouse, France. After test runs with different meshes, both full and quarter meshes in sample calculations, the following findings have influenced the choice of the final mesh:

- Quarter meshes exploiting periodicity exhibit two disadvantages:
  1. The turbulent full 3D flow field is reduced to a 90° periodic problem. In this way parts of the advantages of LES calculations are lost. Especially turbulent 3D effects are affected.
  2. Numerical issues have been observed on the edges of the periodicity which quickly can lead to divergence. Strong effects have been observed on the rotational axis itself and the corner point between periodicity, wall and outlet.

- Structured meshes exhibit the following disadvantages:
  1. The ordered structure of the grid cells helps non-physical high order modes to develop.
  2. Checkerboard patterns can develop easily in the pressure and velocity fields.
  3. The development of jet-like structures on the boundary conditions can be favored.
  4. Local mesh refinement is difficult to realize.

Therefore, the final mesh used for the LES calculations is a full 3D unstructured mesh. It is locally refined along the walls, the swirler and the flame. The smallest cells are governed by resolution requirements on the front edge of the swirler blade, which is 1 mm thick, and by resolution in the flame front. A thickening factor of the thickened flame model of less than 10 was required. Larger thickening factors caused an elongation of the flame along the walls of the combustion chamber, displacing the heat release zone. Smaller cells were not used in order to avoid too small time steps. The resulting mesh has $\approx 10 \cdot 10^6$ tetrahedral cells; using this mesh a time-step of $1.5 \cdot 10^{-7}$ s can be used in the hot case, keeping the CFL number smaller than 1. The mesh is shown in figures 6.18 and 6.19.
The numerical scheme cannot be chosen freely because of the implementation of the boundary conditions. A 1-step temporal scheme is required for the excitation and possible filters in the boundary condition. Further development on the boundary conditions would be necessary to overcome this limitation.
For acoustic calculations, often schemes of high order in space are used. Here, schemes of second order in space and first order in time are employed. Therefore, the properties of the mesh for acoustic waves have been evaluated using test cases. Both the finest and the coarsest parts of the mesh show less than 1% loss in the amplitude of the acoustic waves. The test was conducted using a 0.5 m domain with the corresponding mesh at cold conditions (293 K, 101,325 Pa). An excitation of the highest frequency of interest, 1000 Hz, was imposed at the inlet and the recorded amplitudes at the inlet and the non-reflecting outlet have been compared. The parameters have been chosen to

cover the worst case scenario which in this case is the lowest spacial resolution of an acoustic wave on the mesh.

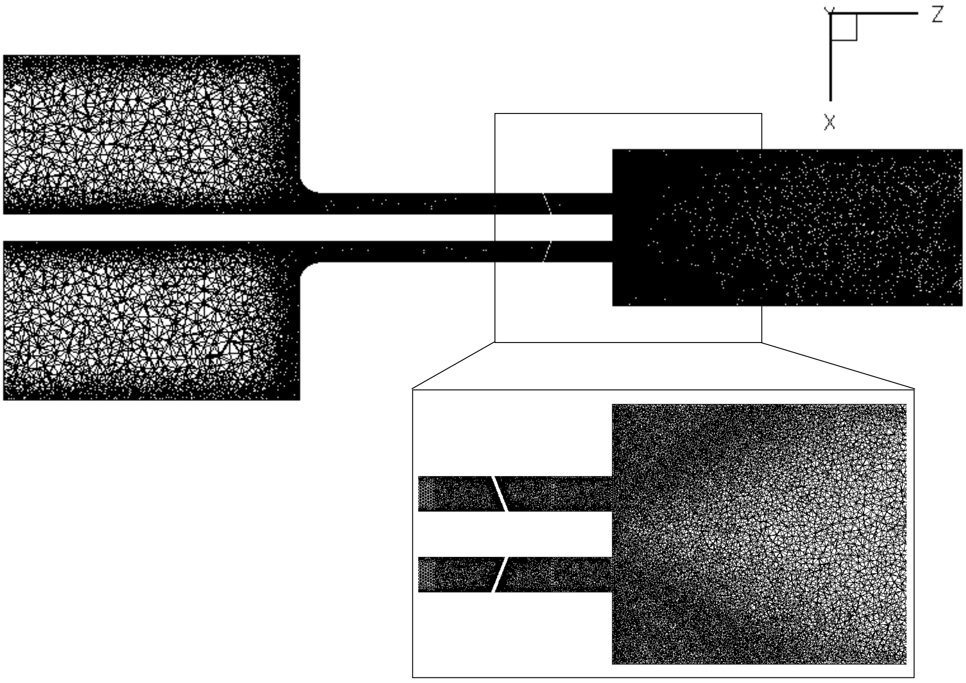

Figure 6.18: Axial cut through the mesh of the BRS burner with a detail of the mesh around the entrance to the combustion chamber showing the local refinement.

6.2.3.2 Boundary Conditions

The application of the CNN approach for the determination of thermoacoustic stability requires careful choice of the boundary conditions. An overview over all boundary conditions applied can be seen in figure 6.20. The single patches are described below.

Outlet Boundary Condition The simulation suffers from a high order mode which develops over the course of $\approx 8 \cdot 10^5$ time steps (at $1.5 \cdot 10^{-7}$s) in the combustion chamber. The mode develops on the diagonal of the cross section of the combustion chamber at a frequency which suggests an acoustic origin. Such mode has not been observed in the experiments.

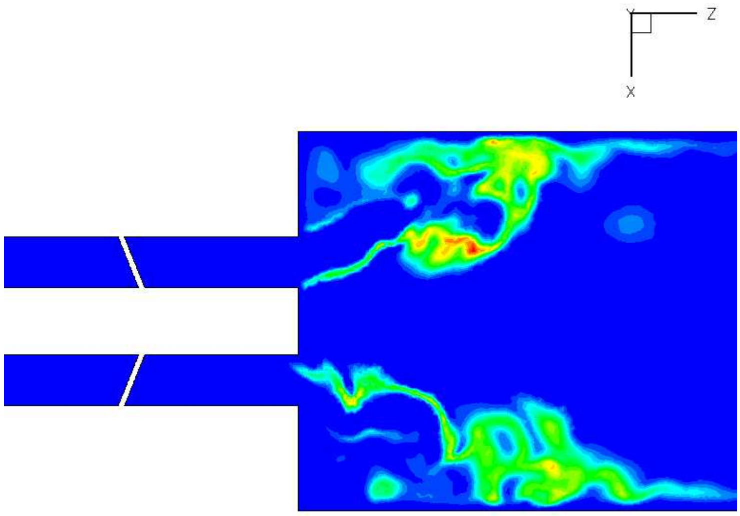

Figure 6.19: Location of the flame by contours of the reaction-rate in the area of the detail of the mesh visible in figure 6.18.

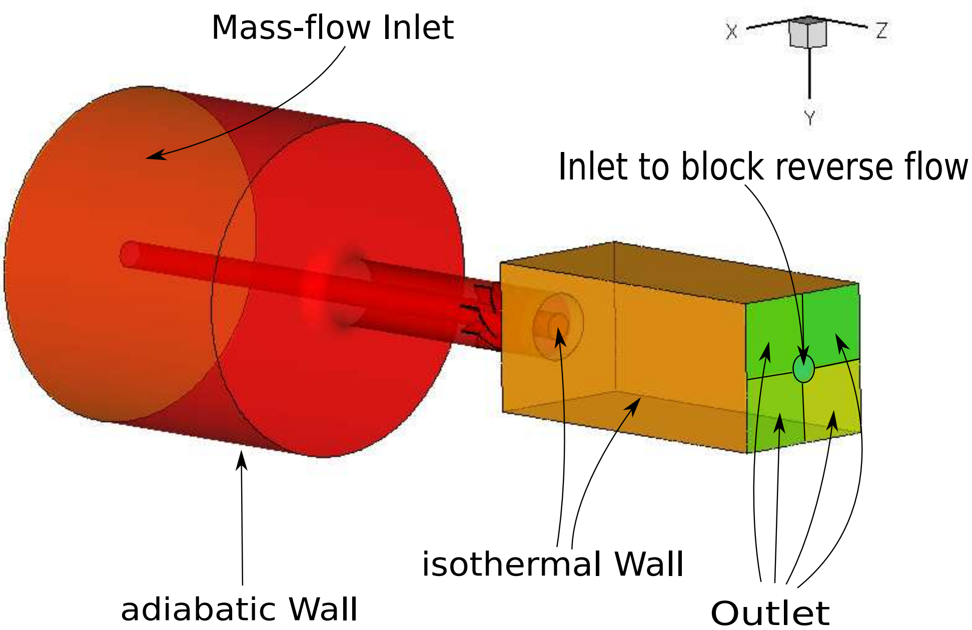

Figure 6.20: Overview of the boundary patches used for the numerical simulation of the BRS burner.

The non-reflecting boundary conditions described in section 4.2, which are used here, are only non-reflecting for the planar contributions of the acoustic signal. Non-planar contributions as they occur with the diagonal mode are partly reflected. Therefore, in order to suppress the mode the outlet has been divided into four zones, so each zone can react locally on the diagonal mode. In combination with a low coupling parameter, this suppresses the occurrence of the high order modes long enough to obtain an undisturbed time series for post-processing. Each of the four zones has its own set of three monitor planes forming a small characteristics based filter (see figure 6.21). The planes are defined only in the quadrant which corresponds to the boundary condition. Post-processing shows that the signals obtained at the four outlet patches indeed are not identical. This is due to flow field asymmetries and small asymmetries in the acoustics. The division of the outlet into four zones should eliminate parts of the effect caused by these asymmetries. The excitation is imposed synchronously at all outlets. The center part of the outlet is formed by a small velocity inlet which imposes a zero velocity and prevents fluid from flowing back into the domain. This inlet is non-reflecting and excitation is imposed in phase with the outlets. The monitor-planes for this inlet are located at the same distance as the ones for the outlets but cover the entire cross subsection (see figure 6.21). It is assumed that asymmetries do not have an influence on the small center zone. Hence, although the outlet is divided into five zones, acoustically it acts as one non-reflecting patch imposing planar waves.

Inlet boundary Condition The inlet boundary condition is a characteristic mass-flux boundary condition. In the test rig, the inlet is formed by a sinter-metal plate. This plate is expected to be nearly fully reflecting. Therefore, a high coupling parameter is assigned to the inlet, providing a minimum of 99% reflection over the frequency band of interest (50 – 1000 Hz). The velocity is imposed using a flat profile with a linear decay to the walls on the 5 mm next to the walls. This ensures the correct mass flow along with the no-slip walls.

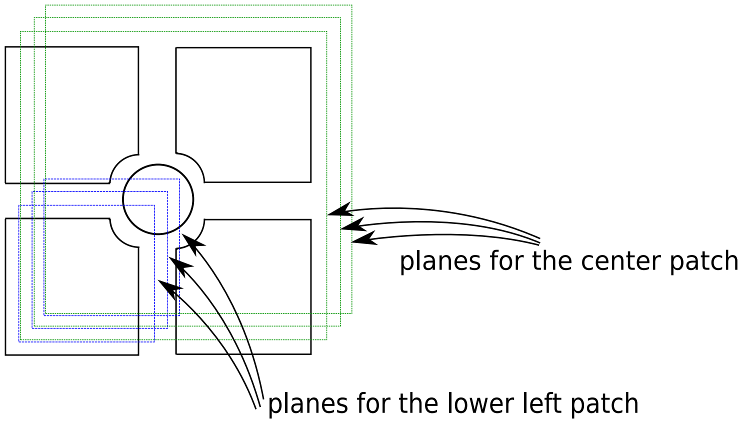

Figure 6.21: Location of the monitor planes for the center patch (zero velocity inlet) and one outlet boundary patch (lower left).

Wall boundary conditions The walls are divided into three patches: the combustion chamber including some millimeters of the swirler-duct and the tip subsection of the lance are modeled using a standard no-slip isothermal wall. The temperature is set to 600 K which is an estimated value [42]. No temperature measurement was performed on the walls during the experiments, but there was visual access to the interior of the combustion chamber. Since no glowing of the metal inside the combustion chamber was observed during the experiments, the temperature has been set to a level below the glow temperature.
The isothermal wall has an important impact on the shape of the flame. Figure 6.19 shows that the flame is burning more intensely on the inner shear layer, next to the lance. The outer shear layer shows little chemical reaction. This corresponds to observations made in the experiments and is caused by quenching mechanisms next to the relatively cold wall. If an adiabatic wall is used here, both shear layers react with comparable intensity, which is not physical. Komarek and Tay have done extensive studies on this topic [43, 104].
The rest of the walls are all located in cold areas of the burner and therefore an adiabatic no-slip wall is used.

6.2.3.3 Numerical Parameters

AVBP offers different temporal and spacial discretization schemes. According to the user manual different combinations of these schemes are possible, but

not random combinations. The implementation of the boundary condition and the excitation are most stable on a single-step, explicit temporal scheme. Therefore, the single step Lax Wendroff scheme has been chosen. This scheme offers second order precision in time and space. As mentioned above, the grid is fine enough to not cause dissipation on acoustic waves in the range of interest. No substantial curtailment in the precision of the flow field is expected from the quite low order of the numerical scheme, as long as the resolution of the grid is reasonably fine. The time step is $1.5 \cdot 10^{-7}$s and is kept fixed to facilitate the acoustic excitation and the post-processing. Data for the post-processing are extracted every 10 iterations at 17 monitor planes. 15 of these are located close to the outlet, as described above in the corresponding section, one is located at the inlet and another one close to the swirler. The Wale LES subgrid scale model is used, which is described in section 2.4.2. A viscosity mask that increases linearly towards the outlet is applied at the last 50 mm of the walls of the combustion chamber. The outlet patch itself also has a viscosity mask of 0.2. No influence on the acoustic field is visible and the acoustic data are extracted far enough away from the outlet patch. A thickened flame model with a fixed thickening factor of 5 is used for the simulation of the combustion. The parameters have been adjusted vs a 1-Step Arrhenius formulation in a 1-D simulation. The most relevant input files are printed in the appendix. Computation is performed on the HLRB II supercomputer of the Leibniz Rechenzentrum (LRZ) in Garching which is Nr. 44 in the Top 500 supercomputer list of November 2008[1]. For a typical productive run, 128-256 CPUs are used. The code yields about 400,000 iterations in 48h on 256 CPUs.
Mean LES results for all configurations are summarized in section 8.1. In general it can be stated that the time averaged LES flow fields and flame shapes agree well with the experimental data.

6.2.3.4 Acoustic Excitation Signal for the LES Calculation

The acoustic excitation is essential to obtain the flame transfer function $F(\omega)$ or in our case the part loop transfer function (PLTF). The signal used has to fulfill certain requirements in order to permit good results. The first requirement

[1] www.top500.org

is a limited frequency content, so that the signal can be transmitted without substantial dissipation on the grid. The WHI post-processor implemented for system identification uses correlation analysis to obtain the transfer function. This implies that a continuous spectrum, i.e. noise, can be used as excitation. Conventional FFT would suffer from the low energy content in each frequency in this case. Due to the correlation approach, the WHI is less sensitive to this limitation but rather needs signals with strong correlation properties. Experiments on different signals show that a high level of significant changes in the signal, i.e. rapid changes of the signal amplitude, facilitates the correlation and yields better auto-correlation results. Therefore, a pseudo random binary signal (pbrs) is chosen for the excitation. The signal is low pass filtered, which is necessary for the following two reasons. First, the grid can only transmit signals up to a certain frequency. Second, a self excited high order mode in the simulation, which occurs at frequencies of $f \approx 5000$ Hz, has to be avoided. Therefore, the signal should not contain those frequencies. The signal used has vanishing frequency content above 2500 Hz. In order to preserve the shape of the signal during the filtering process, the maximum frequency of the binary changes is limited and the signal is filtered afterwards. The beginning part of a typical excitation signal is shown in figure 6.22. A longer series can be seen in figure 6.24. In conclusion, the signal is a compromise between fre-

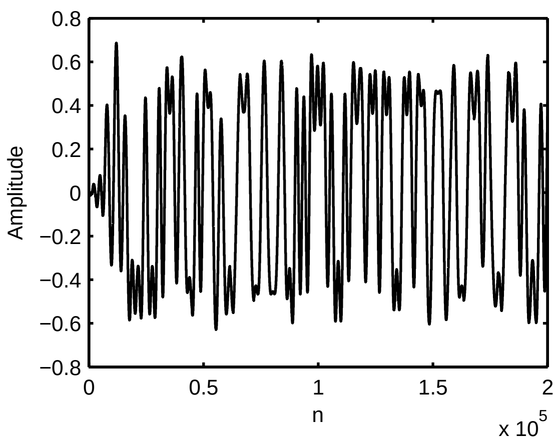

Figure 6.22: Typical shape of a filtered pbrs, the first time steps have been set to 0 before filtering to avoid filter artifacts.

quency content and a pronounced auto-correlation. The spectrum and auto-correlation matrix of the signal in figure 6.22 are shown in figure 6.23.

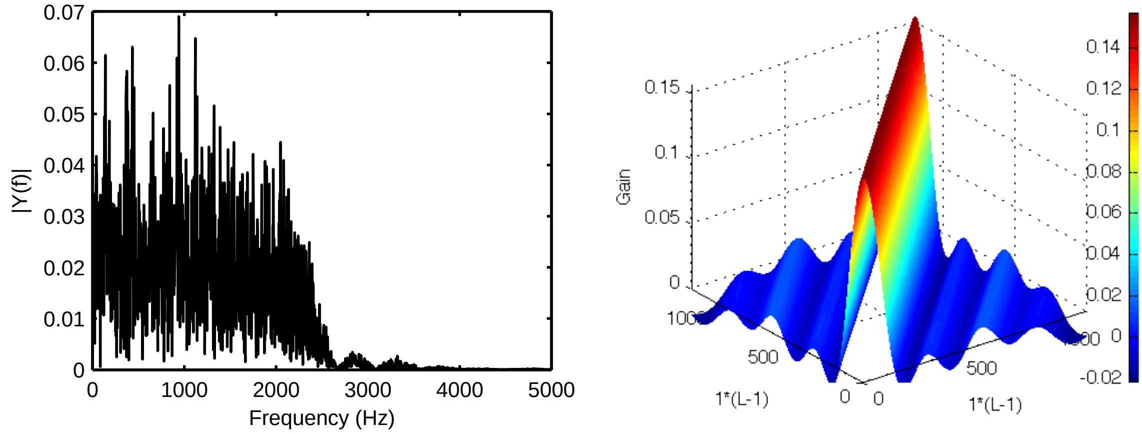

Figure 6.23: Single sided amplitude spectrum (left) and auto-correlation matrix (right) of the filtered pbrs in figure 6.22.

6.2.3.5 Acoustic Results from the LES Calculation

The aim of the LES calculation is the determination of the part loop transfer function, i.e. the acoustic behavior of the LES domain. Here, this goal is achieved using correlation based system identification (see section 2.8) with a time series of at least 800,000 iterations of $1.5 \cdot 10^{-7}$s. Figure 6.24 shows a typical time series of ingoing and outgoing waves. Different WHI parameters have been evaluated but no configuration was found that yields reasonable results for the LES data. The results of the WHI postprocessing of typical LES results depend strongly on the length of the unit impulse response vector and for the amplitude barley exhibit any trend. Solely the phase shows a typical evolution around a linear decay. A typical WHI postprocessing result of such a time series is depicted in figure 6.25. These PLTFs are combined with a network model for the missing part of the combustion chamber and the impedance of the plate at the outlet of the combustion chamber. The impedances of this plate have been measured by Komarek [42] for different operating points, see figure 6.26. In the network model, the values of $P = 50\,\mathrm{kW}$, $\lambda = 1.3$ can be adapted assuming a Strouhal similarity. Figure 6.27 shows a typical Nyquist curve obtained in this way. The curve not does neither predict the unstable behavior

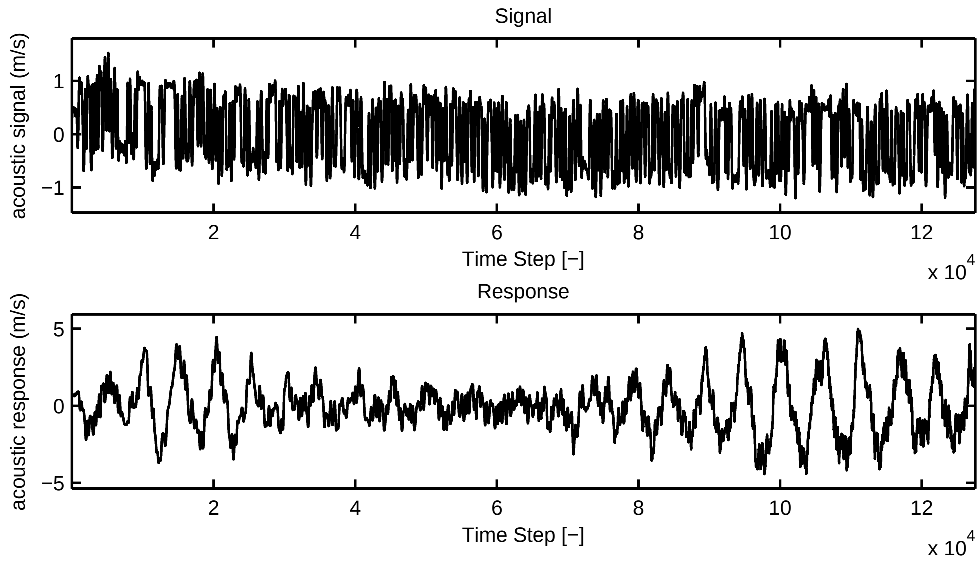

Figure 6.24: Time series of acoustic excitation (top) and response (down) for the LES simulation of the turbulent premix burner at $P = 70\,\mathrm{kW}$, $\lambda = 1.3$

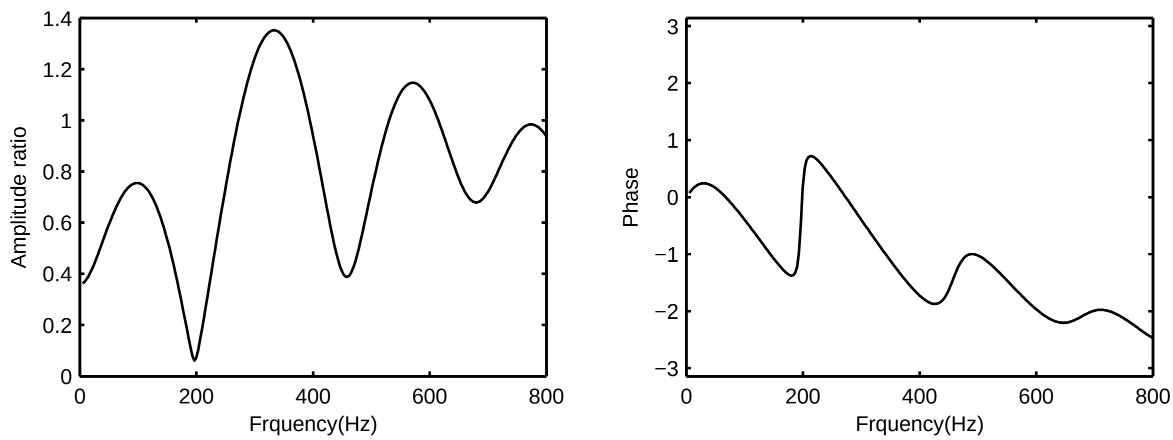

Figure 6.25: Part loop transfer function of the turbulent premix burner for $P = 50\,\mathrm{kW}$, $\lambda = 1.3$, obtained from the LES data using WHI post-processing. Left: amplitude ratio, right: phase.

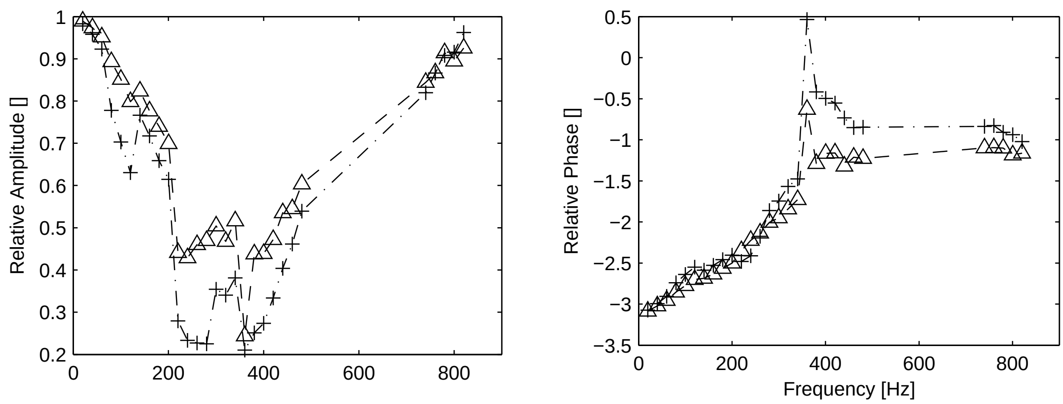

Figure 6.26: Reflection coefficient of the outlet of the BRS burner, left amplitude, right phase. dash-dot + : $p = 70\,\mathrm{kW}$, $\lambda = 1.3$; dashed Δ : $p = 70\,\mathrm{kW}$, $\lambda = 1.1$.

nor does it show a significant approximation of the critical point for frequencies of $f \approx 150\,\mathrm{Hz}$ where instability was observed in the experiment. Hence,

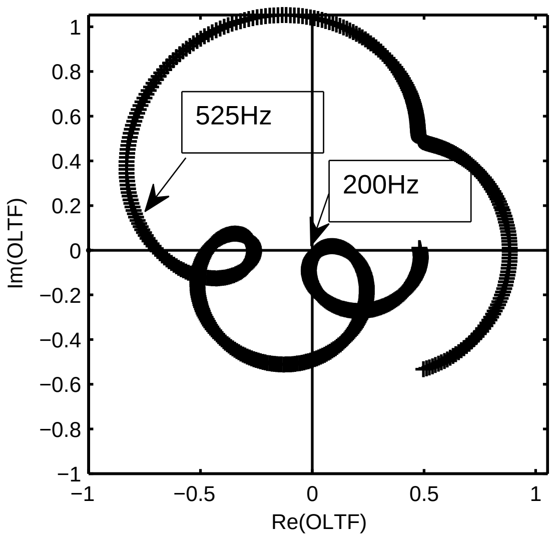

Figure 6.27: Nyquist curve of the turbulent premix burner for $P = 50\,\mathrm{kW}$, $\lambda = 1.3$ obtained from the LES data using WHI postprocessing for the long combustion chamber.

the application of the CNN method to the BRS burner fails.

6.2.4 Analysis of the Problems of the CNN Method

The problems that occurred when the CNN method was applied to the BRS burner require a deeper analysis of this case. This analysis is conducted in this section.

6.2.4.1 Estimated Acoustic Properties of the LES Domain

Similarly to the laminar test case for the perforated plate burner of ECP, the acoustic properties of the LES Domain will be estimated from a network setup. FTF's have been determined by Komarek [42] for the power levels and equivalence ratios mentioned above (see figure 6.28). Mind that due to experimental limitations, the values are only reliable below 500 Hz. At higher frequencies, they rather show the trend. Huber has numerically determined the transfer

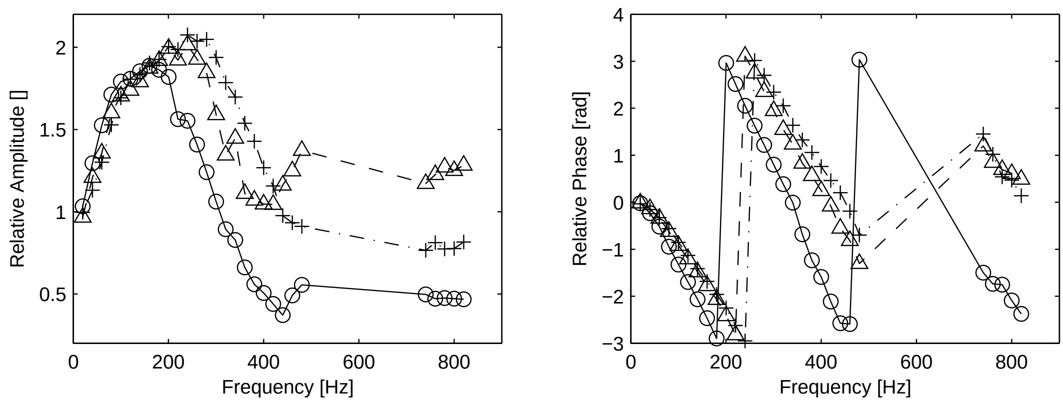

Figure 6.28: FTF of the BRS burner, left amplitude, right phase. dash-dot + : $p = 70\,\text{kW}$, $\lambda = 1.3$; solid o : $p = 50\,\text{kW}$, $\lambda = 1.3$; dashed Δ : $p = 70\,\text{kW}$, $\lambda = 1.1$.

function of the BRS swirl generator, see [27] for more details. All other elements can be modeled using the equations given in section 2.7. The variables used for the single elements are extracted from the mean solution field (see section 8.1) of the simulation at the locations sketched in figure 6.29. Tables 6.4, 6.5 and 6.6 summarize the values.

A network model for $P = 50\,\text{kW}$, $\lambda = 1.3$ will be treated here in detail, all other

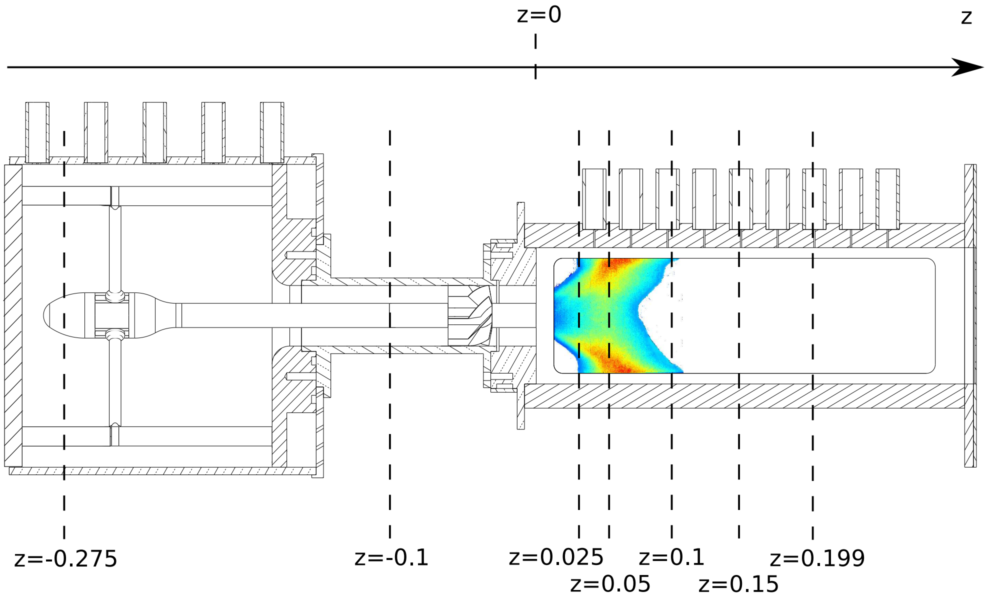

Figure 6.29: Location of the extraction points for the values for the network model (not to scale).

[m]	$z=-0.275$	$z=-0.1$	$z=0.025$	z=0.05	z=0.1	z=0.15	z=0.199
ρ [kg/m^3]	1.152	1.144	0.306	0.227	0.200	0.214	0.227
c [m/s]	349.6	350.1	701.8	801.1	862.1	835.5	818.1
w [m/s]	0.763	22.2	5.02	12.4	18.0	17.4	16.3

Table 6.4: Mean values at indicated positions for $P = 70\,\mathrm{kW}$, $\lambda = 1.1$.

[m]	$z=-0.275$	$z=-0.1$	$z=0.025$	$z=0.05$	$z=0.1$	$z=0.15$	$z=0.199$
ρ [kg/m^3]	1.179	1.173	0.345	0.271	0.224	0.230	0.244
c [m/s]	350.6	350.5	662.8	745.2	821.1	810.4	793.1
w [m/s]	0.880	26.1	6.01	11.4	19.0	19.4	18.4

Table 6.5: Mean values at indicated positions for $P = 70\,\mathrm{kW}$, $\lambda = 1.3$.

[m]	$z=-0.275$	$z=-0.1$	$z=0.025$	$z=0.05$	$z=0.1$	$z=0.15$	$z=0.199$
ρ [kg/m^3]	1.171	1.167	0.341	0.267	0.226	0.239	0.253
c [m/s]	250.2	350.1	670.0	750.0	817.4	797.1	778.8
w [m/s]	0.635	18.9	4.06	8.44	13.8	13.6	12.8

Table 6.6: Mean values at indicated positions for $P = 50\,\mathrm{kW}$, $\lambda = 1.3$.

configurations can be set up similarly and yield corresponding results. The network model for the estimation of the acoustic properties of the BRS burner is sketched in figure 6.35.

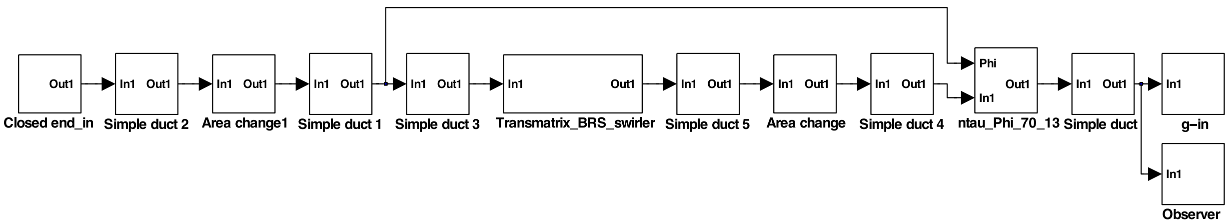

Figure 6.30: TaX network configuration for the estimation of the acoustic behavior of the LES domain of the turbulent premix burner

The result of the evaluation depends significantly on the loss coefficients at the two area changes. Since there is no data available for them, they represent an important uncertainty. Loss coefficients of $\zeta_1 = 1.358$ and $\zeta_2 = 96$ estimated with the pressure data from the mean flow calculation have been chosen. These values are within the range given in the literature [30], when the different reference velocities are taken into account. Part loop transfer functions for the three configurations are shown in figures 6.31, 6.32 and 6.33. The loss coefficients refer to the downstream velocity of the area change.

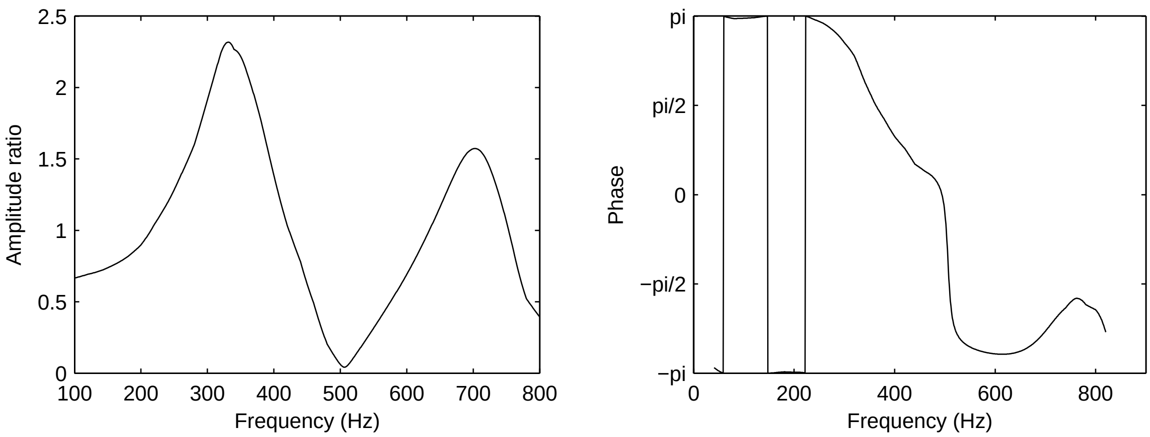

Figure 6.31: Part loop transfer function of the turbulent premix burner for $P = 70\,\mathrm{kW}$, $\lambda = 1.1$, estimated with TaX. Left: amplitude ratio, right: phase.

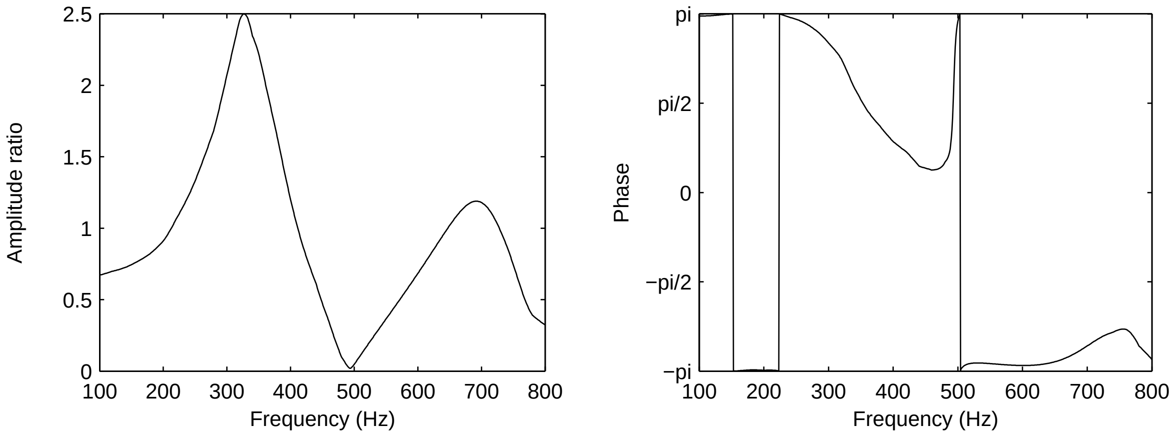

Figure 6.32: Part loop transfer function of the turbulent premix burner for $P = 70\,\mathrm{kW}$, $\lambda = 1.3$, estimated with TaX. Left: amplitude ratio, right: phase.

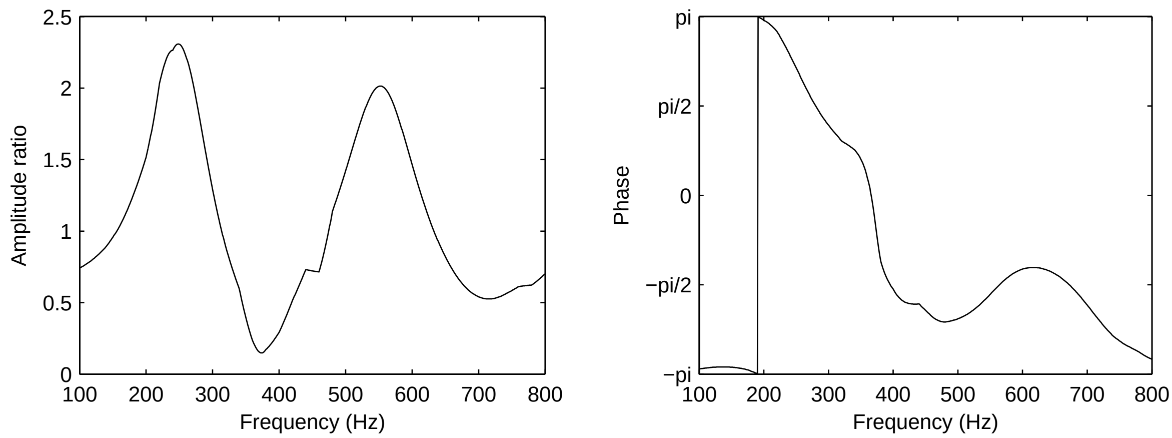

Figure 6.33: Part loop transfer function of the turbulent premix burner for $P = 50\,\mathrm{kW}$, $\lambda = 1.3$, estimated with TaX. Left: amplitude ratio, right: phase.

The pure acoustic properties of the domain can be seen in figure 6.34, where in contrast to the figures above, the flame model is removed. All other components are identical. The peaks in the amplitude vanish and the phase exhibits a nearly linear decay. The linear decay corresponds to a time delay for a wave traveling from the outlet to the burner mouth and back.

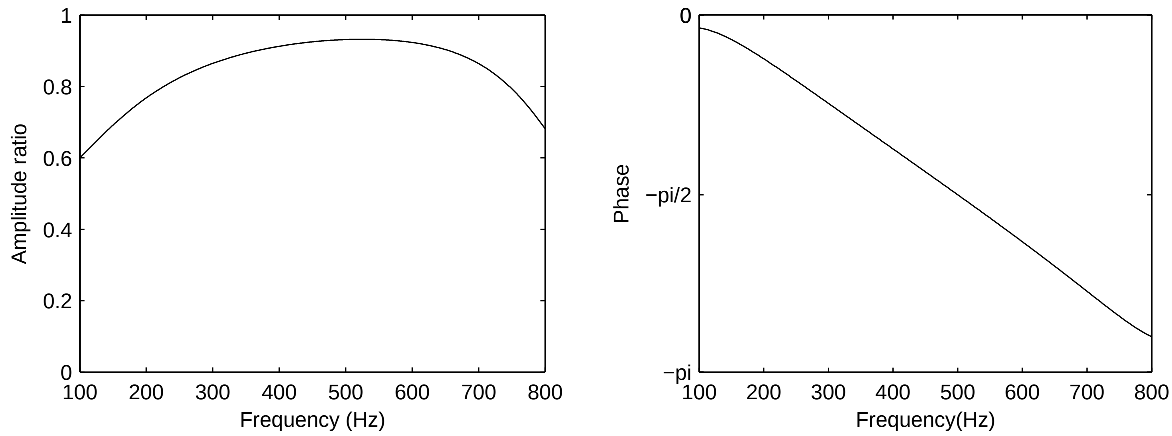

Figure 6.34: Part loop transfer function of the turbulent premix burner for the mass flow rate of $P = 50\,\mathrm{kW}$, $\lambda = 1.3$ without flame, estimated with TaX. Left: amplitude ratio, right: phase.

6.2.4.2 Analysis of the Acoustic Response of the LES

Comparing the expected PLTF with the one obtained in the LES exhibits some interesting facts: The PLTF, obtained using LES (figure 6.25) differs substancially from the estimated PLTF (figure 6.33). Especially around $f = 200\,\mathrm{Hz}$ in the LES hardy any correlation between signal and response is present, the PLTF approaches zero. This is not the case in the estimated PLTF. The phase of the PLTF of the LES shows a decay which is more similar to the estimated value without flame model (figure 6.34) than with the expected behavior.
In the temporal evolution of the response signal of the LES calculation (figure 6.24), a low frequency perturbation can be seen, which is growing and decaying. The frequencies of these oscillations are summarized in table 6.7 for the different power and equivalence ratios which were examined . The table shows also that there is a proportionality between mass flow rate and frequency.

case	$P = 50\,\text{kW}, \lambda = 1.3$	$P = 70\,\text{kW}, \lambda = 1.3$	$P = 70\,\text{kW}, \lambda = 1.1$
f [Hz]	130	165	160
$\rho \cdot u$ [kg/s/m^2]	2.25	3.08	2.82
$f,/(\rho, \cdot u)$ [kg/s^2/m^2]	56	55	57

Table 6.7: Frequency of maximum amplitude in the acoustic response, mass flow rate before the flame in the LES Calculation of the turbulent premix burner and proportionality between frequency and mass flow rate for the three operation points.

These frequencies do not coincide with the maximum of the PLTF obtained using WHI postprocessing (figure 6.25). This implies that the flame dynamics are not dominated by the acoustic excitation. The fact that the phase corresponds to the estimated phase without flame model supports this assumption. The flame could be self excited within the LES domain.
The fact that there is a proportionality between mass flow rate and frequency (see table 6.7) suggests that inertial effects are involved in the generation of the instability in the LES. Additionally, the frequency of $f \approx 150\,\text{Hz}$ in the simulation is of the order of magnitude that would be expected for typical convective phenomena (density is not considered here),

$$f \approx \frac{\bar{u}}{l_{char}} = \frac{18.9\,\text{m/s}}{0.1\,\text{m}} = 189\,\text{Hz}, \tag{6.3}$$

where $\bar{u}$ is the mean axial velocity in the swirler for $P = 50\,\text{kW}$, $\lambda = 1.3$ and l_{char} corresponds approximately to the distance between swirler and flame. Keller, according to [76], obtains a similar frequency estimation when considering an oscillating rotating fluid bulk in between swirler and burner mouth. Hence, the main instability mechanism in this burner in the simulation could be of non-acoustic origin, but convection or inertia driven. Taking into account the experimentally observed frequencies of the instabilities, table 6.3, this consideration proves to be partly reasonable also for the experiment:

$$P \uparrow \rightarrow \bar{u} \uparrow \rightarrow f \uparrow . \tag{6.4}$$

The experiment therefore might exhibit the same phenomenon as the LES and exhibit an instability driven by convection.

The assumption of a non-acoustic origin of the instability is supported by a numerical examination of the BRS using Comsol. A model of the hot burner having the long chamber including realistic temperature and density fields but no flame exhibited eigenfrequencies in the range of 500 Hz, which is far away from the observed ones. There was also an eigenfrequency in the range of 50 Hz, but this is likely to be a numeric artifact. [110]
The fact that the length of the combustion chamber determines stability still does not fit this assumption, but a tuning or detuning of the system by the length of the chamber might be the reason.
The amplitude of the FTF which was experimentally determined (see figure 6.28) still exhibits its maximum around the frequencies of the instabilities. But, monochromatic, i.e., single frequency siren excitation, signals are used when FTFs are determined experimentally. These signals have stronger energy content in the single frequency and are applied over a long time. Therefore, they may favor the triggering of hydrodynamic effects.
In contrast, the time series obtained in the LES is rather short and polychromatic. Therefore, establishing a causal link as would be required for the WHI is nearly impossible. Possibly, a triggering of the hydrodynamic mechanism with the acoustic mechanism would occur for longer excitation or monochromatic excitation. On the other hand, a series of calculations using monochromatic excitation would exceed the computational resources which are available and make the approach impracticable.

6.2.4.3 Analysis with Network Model

The BRS is examined using a conventional network model in combination with a diagnostic dummy. The aim of this analysis is to determine if the position of the diagnostic dummy, i.e. the cut, plays a role in the problems that have occurred when the CNN method was applied to the BRS burner. However, in the CNN method, the location of the cut is determined by the interface between LES and Network domain. In the present configuration the advantages of the CNN method can only be utilized, when the interface is located downstream of the flame, as it has been done. In this way, it is possible to use

the network model for the two different lengths of the combustion chamber. At the same time, the complex interactions between swirl, combustion and acoustics in the flame can be modelled in the LES domain.
Nevertheless, it is of interest if other configurations would have obtained better results. The complete network model of the BRS burner is similar to the model for the estimation of the acoustic properties. Only the impedance, i.e. the reflection coefficient of the plate at the outlet (figure 6.26) of the combustion chamber, has to be added. The corresponding TaX network model is shown in figure 6.30. The following different locations for the Nyquist dummy

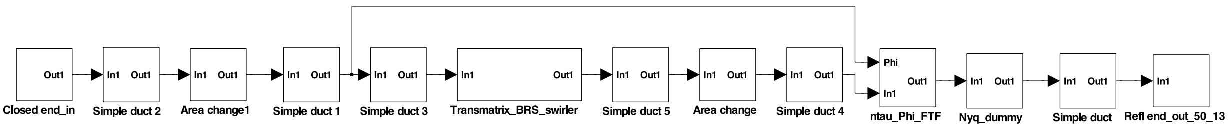

Figure 6.35: TaX network configuration for the estimation of the acoustic behavior of the turbulent premix burner

have been evaluated:

- downstream of the flame (as in the CNN method),
- in the plenum,
- between swirler and burner mouth (the connection between flame element and velocity fluctuation in the swirler duct is changed and velocity information is extracted right downstream of the diagnostic dummy)

The corresponding Nyquist plots for both 300 mm and 700 mm combustion-chamber length are shown in figures 6.36, 6.37 and 6.38. The following items can be observed:

- For the cut located downstream of the flame (figure 6.36), an interpretation is hardly possible. Approximations to the critical point can be observed for $f \approx 270$ Hz in case of the short combustion chamber and for $f \approx 490$ Hz in the case of the long combustion chamber. In the frequency range of 150 Hz the Nyquist curve never circles the critical point in a way that the critical point is located to the right of the Nyquist curve. Hence,

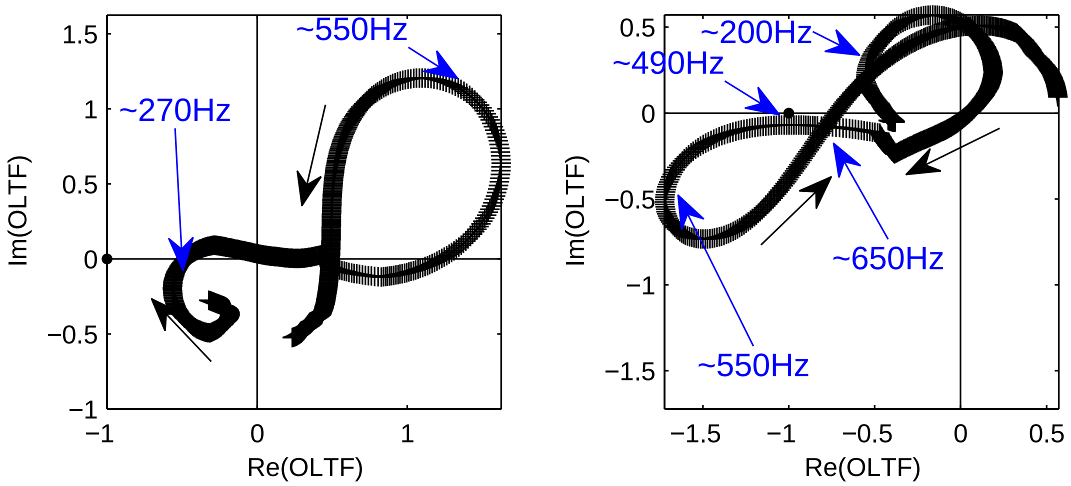

Figure 6.36: Nyquist plot of the turbulent premix burner for short (left) and long (right) combustion chamber for a location of the Nyquist Dummy downstram of the flame. Black arrows indicate the sense of rotation, blue arrows depict certain frequencies.

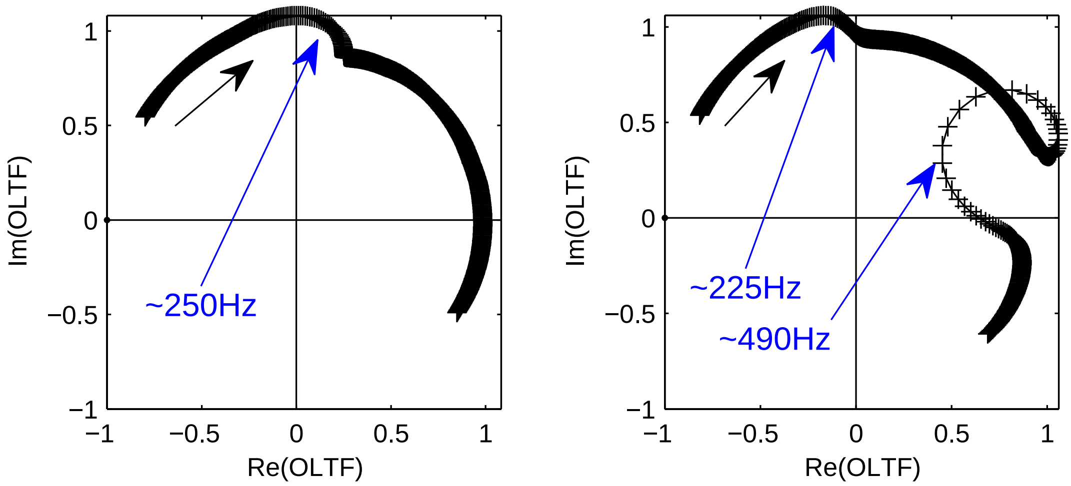

Figure 6.37: Nyquist plot of the turbulent premix burner for short (left) and long (right) combustion chamber for a location of the Nyquist Dummy in the plenum. Black arrows indicate the sense of rotation.

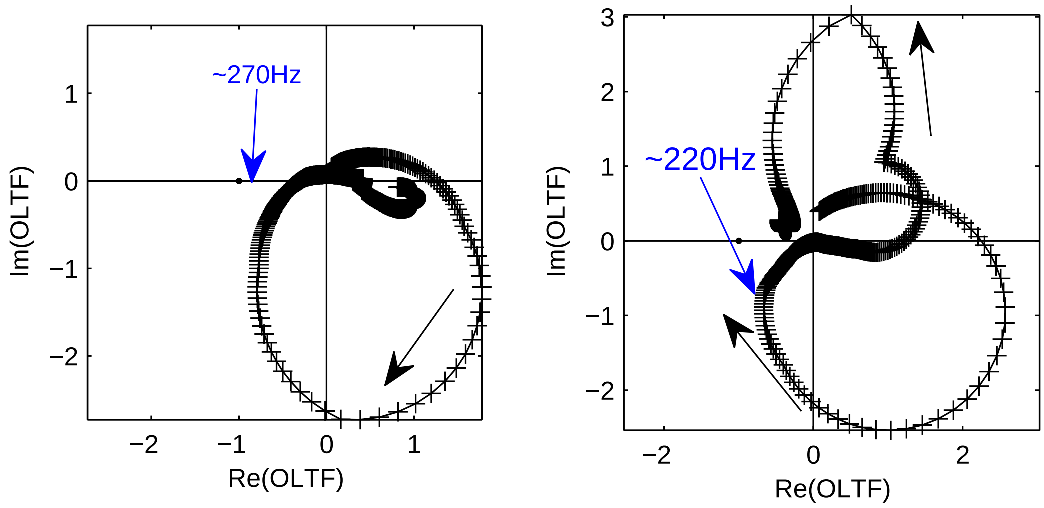

Figure 6.38: Nyquist plot of the turbulent premix burner for short (left) and long (right) combustion chamber for a location of the Nyquist Dummy between swirler and burner mouth. Black arrows indicate the sense of rotation.

no indications for the instability, which is present in the experiment, can be seen.

- If the cut is located in the plenum (figure 6.37), the short configuration does not exhibit indicators for instability. The long configuration shows an unconventional loop having an inverted sense of rotation for $f \approx 490$ Hz. The curve has the basic shape of half a circle. This circle corresponds to the acoustic eigenfrequency of the plenum. Due to the pronounced area changes between plenum and swirler, a strong reflection is present at the area change. Therefore, the acoustics of the plenum dominate the Nyquist curve.

- If the cut is placed between swirler and burner mouth, the most significant approximations to the critical point are at $f \approx 270$ Hz for the short and $f \approx 270$ Hz for the long configuration. Both of them are stable.

The location of the cut does significantly change the Nyquist curve. However, none of the three positions resulted in meaningful Nyquist curves for stability evaluation.

6.2.5 Conclusion

The results for the BRS burner do not deliver the data necessary for a stability examination using the CNN method.
The evolution of the phase compared to the preliminary examination of the pure combustion chamber (figure 6.34) implies that a correlation between the effect of the flame and the acoustic excitation barely exists. Hence, the instability mechanism for this case is likely not captured using the CNN method. The result of the LES calculation does not deliver the information necessary for this method. A possible reason for this is that the instability is not purely acoustically driven. Additionally, the feedback line of the instability seems to be located upstream of the flame, where it is not captured by the cut.
Therefore, the CNN method is not able to capture the effect and predict the instability. However, for a definite explanation further experiments would be required. A different setup for the LES is neither likely to solve the problem nor is it expedient here, since the main argument for the application of the CNN approach was the possibility to account for different lengths of the combustion chamber. This is only possible with the present setup. Therefore, the CNN method fails for this example.

7 Summary and Discussion

The CNN approach for the determination of thermo-acoustic stability using LES simulations and network models has been evaluated in this work theoretically and practically. The theoretical part has demonstrated the potential and the limitations of this method and Nyquist methods in general to acoustic and thermo-acoustic problems.
Two test cases have been calculated:

- A laminar premix burner with a plenum of variable length.
- A turbulent premix burner operated at different operating points and two combustion chambers of different lengths.

Both cases exhibit instabilities at certain parameters. Although both cases seem to be suitable for the application of the CNN method, the application is only successful in the first case. In this first case, the eigenfrequencies are well predicted, only the growth rates are insecure due to unknown acoustic losses.
In the second case, the application of the CNN method to the problem fails. The reason for this failure are evaluated and it can be concluded that the most likely cause is a convective and not acoustic origin of the instability.
Due to the difficulties which occurred, the theoretical background of the application of Nyquist methods to thermo-acoustic cases have been pointed out. The assumption that Nyquist models could be used without any restrictions for thermo-acoustic cases is not thoroughly valid:

- The location of the cut plays an essential role.
- Badly placed cuts generate Nyquist curves, which cannot be interpreted in a reliable manner.

- A position between burner mouth and flame is favorable, because thermo-acoustic modes are likely to be localized here.

In pure network models, the location of the cut, i.e. diagnostic dummy, can mostly be changed quickly to meet these requirements. Reasons for the requirements of the location of the cut and the consequences for the Nyquist curve have been found in the theory of conformal mapping which is the mathematical origin of the Nyquist criterion.
The CNN method has the same restrictions as general Nyquist methods. Additionally, the position of the cut is imposed by the interface between CFD and network domain. The favorable position between burner mouth and flame is not applicable here, both will mostly be part of the CFD domain.
In the course of this work boundary conditions for acoustic applications in LES have been developed as well as acoustic data extraction tools for LES. Both have already been applied successfully in different applications [16, 51, 103]
For future applications, better signal processing tools for data post-processing should be developed, since WHI methods have exhibited limitations for noisy applications.
To summarize, it can be stated, that the field of application of CNN method is more limited than originally expected [46]. It is sensitive to the location of the cut and at the same time the cut often cannot be placed in the optimum position. Therefore, it is not suitable for a quick and unprepared evaluation. The application is limited to cases where the location of the mode is favorable, i.e. the mode is located where the system is cut.

Bibliography

[1] C. Angelberger and T. Poinsot. LES model for premixed combustion. Technical Report TR/CFD/98/14, CERFACS, 1998.

[2] Various Authors. *The AVBP Handbook*. Cerfacs, 42. Av. G. Coriolis, Toulouse, France, 2006.

[3] P. Baade. Selbsterregte Schwingungen in Gasbrennern. *Kälte, Klima, Ingenieur*, 6:167–176, 1974.

[4] A. Betz. *Konforme Abbildung*. Springer-Verlag, 1964.

[5] D. Bohn and E. Deuker. An acoustical model to predict combustion driven oscillations. In *20th International Congress on Combustion Engines (CIMAC)*, pages 1–13, 1993.

[6] T. Chung. *Computational Fluid Dynamics*. Cambridge University Press, 2002.

[7] O. Colin, F. Ducros, D. Veynante, and T. Poinsot. A thickened flame model for Large Eddy Simulations of turbulent premixed combustion. *Physics of Fluids*, 12(7):1843–1863, 2000.

[8] T. Colonius and H. Ran. A super-grid-scale model for simulating compressible flow on unbounded domains. *Journal of Computational Physics*, 182:191–212, 2002.

[9] L. Crocco. Aspects of combustion stability in liquid propellant rocket motors. *Journal of the American Rocket-Society*, pages 163–178, 1951.

[10] F. Culick. Stability of high-frequency pressure oscillations in rocket combustion chambers. *AIAA Journal*, 1(5):1097–1104, May 1963.

[11] E. Deuker. *Ein Beitrag zur Vorausberechnung des akustischen Stabilitätsverhaltens von Gasturbinen-Brennkammern mittels theoretischer und experimenteller Analyse von Brennkammerschwingungen.* PhD thesis, RWTH Aachen, 1994.

[12] L. Durand. *Developement, Implementation and Validation of LES Models for Inhomogenously Premixed Turbulent Combustion.* PhD thesis, Technische Universität München, Lehrstuhl für Thermodynamik, 2007.

[13] K. Ehrenfried. *Strömungsakustik, Skript zur Vorlesung.* Mensch & Buch Verlag, Berlin, 2004.

[14] B. Engquist and A. Majda. Absorbing boundary conditions for the numerical simulation of waves. *Mathematics of Computation*, 31(139):629–651, 1977.

[15] A. Fischer, C. Hirsch, and T. Sattelmayer. Comparison of multi-microphone transfer matrix measurements with acoustic network models of swirl burners. *Journal of Sound and Vibration*, 298:73–83, 2006.

[16] S. Föller, R. Kaess, and W. Polifke. Reconstruction of acoustic transfer matrices from Large-Eddy-Simulations of complex turbulent flows. Number AIAA-2008-3046 in 14th AIAA/CEAS Aeroacoustics Conference (29th AIAA Aeroacoustics Conference), Vancouver, Canada, May 5 – 7 2008. AIAA/CEAS, AIAA.

[17] K. Fung, , H. Ju, and B. Tallapragada. Impedance and its time-domain extensions. *AIAA Journal*, 38(1):30–38, 2000.

[18] K. Fung and J. Hongbin. Time-domain impedance boundary conditions for computational acoustics and aeroacoustics. *International Journal of Computational Fluid Dynamics*, 18:503–511, 2004.

[19] K. Fung and H. Ju. Time-domain impedance boundary conditions for computational acoustics and aeroacoustics. *International Journal of Computational Fluid Dynamics*, 18(6):503–511, 2004.

[20] H. Geering. *Regelungstechnik*. Springer-Verlag, 2004.

[21] A. Gentemann. *Identifikation von akustischen Transfermatrizen und Flammenfrequenzgängen mittels Strömungssimulation*. PhD thesis, Technische Universität München, Lehrstuhl für Thermodynamik, 2006.

[22] A. Gentemann, A. Fischer, S. Evesque, and W. Polifke. Acoustic transfer matrix reconstruction and analysis for ducts with sudden change of area. Number AIAA-2003-3142 in 9th AIAA/CEAS Aeroacoustics Conference and Exhibit, page 11, Hilton Head, SC, USA, May 12-14 2003. AIAA. GenteFischEvesq03.

[23] A. Giauque, T. Poinsot, W. Polifke, and F. Nicoud. Validation of a flame transfer function reconstruction method for complex turbulent configurations. 14th AIAA/CEAS Aeroacoustics Conference, Vancouver, Canada, 2008.

[24] C. C. Hantschk and D. Vortmeyer. Numerical simulation of self-excited thermoacoustic instabilities in a Rijke Tube. *J. of Sound and Vibration*, 277(3):511–522, 1999.

[25] H. Helmholtz von. Über den Einfluss der Reibung in der Luft auf die Schallbewegung. *Verhandlungen des Naturhistorisch-Medizinischen Vereins zu Heidelberg*, 3:16–20, 1863.

[26] F. Hu. Absorbing boundary conditions. *International Journal of Computational Fluid Dynamics*, 18 (6):513–522, 2004.

[27] A. Huber. *Impact of fuel supply impedance and fuel staging on gas turbine combustion stability*. PhD thesis, Technische Universität München, Lehrstuhl für Thermodynamik, 2009.

[28] A. Huber and W. Polifke. Impact of fuel supply impedance on combustion stability of gas turbines. In *Proceedings of ASME Turbo Expo 2008: Power for Land, Sea an Air GT 2008*. ASME, June 2008.

[29] A. Huber, P. Romann, and W. Polifke. Filter-based time-domain impedance boundary conditions for CFD applications. In *Proceedings*

of ASME Turbo Expo 2008 Power for Land, Sea and Air, June 9-13, 2008, Berlin, Germany, number GT2008-51195, 2008.

[30] I. E. Idelchik. *Handbook of Hydraulic Resistance.* Springer-Verlag, 1986.

[31] O. Jacobs. *Introduction to Control Theory.* Oxford University Press, 1993.

[32] R. Kaess. A time domain impedance boundary condition for AVBP. Technical report, Technische Universität München, Lehrstuhl für Thermodynamik, 2008.

[33] R. Kaess, A. Huber, and W. Polifke. A time-domain impedance boundary condition for compressible turbulent flow. Number No. AIAA-2008-2921 in 14th AIAA/CEAS Aeroacoustics Conference (29th AIAA Aeroacoustics Conference). AIAA, May 5 – 7 2008.

[34] R. Kaess, T. Poinsot, and W. Polifke. Determination of the stability map of a premix burner based on flame transfer functions computed with transient cfd. Proceedings of the European Combustion Meeting 2009 (submitted), 2009.

[35] R. Kaess and W. Polifke. A non reflecting boundary condition using wave masking and characteristics based filtering. In *2nd GACM Colloquim on Computational Mechanics.* GACM, 2nd GACM Colloquim on Computational Mechanics, 10.-12. October, Munich, Germany, 2007.

[36] R. Kaess, W. Polifke, T. Poinsot, N. Noiray, D. Durox, T. Schuller, and S. Candel. CFD-based mapping of the thermo-acoustic stability of a laminar premix burner. In *Proceedings of the Summer Program 2008.* Center for Turbulence Research, July 2008.

[37] J. Keller. Thermoacoustic oscillations in combustion chambers of gas turbines. *AIAA Journal*, 33(12):2280–2287, December 1995.

[38] G. Kirchhoff. Ueber den Einfluss der Wärmeleitung in einem Gase auf die Schallbewegung. *Annalen der Physik und Chemie*, 134(6):177–193, 1868.

[39] A. Kolmogorov. A refinement of previous hypothesis concerning the local structure of turbulence in a viscous incompressible fluid at high reynolds number. 1962. Academy of sciences of the USSR, Moscow.

[40] A. Kolmogorov. Dissipation of energy in the locally isotropic turbulence. *Proceedings: Mathematical and Physical Sciences, Turbulence and Stochastic Process: Kolmogorov's Ideas 50 Years On*, 434(1890):15–17, July 1991. Reprint of the translation of the article published in in Dokl. Akad. Nauk. SSSR 1941.

[41] A. Kolmogorov. The local structure of turbulence in incompressible viscous fluid for very large reynolds numbers. *Proceedings: Mathematical and Physical Sciences, Turbulence and Stochastic Process: Kolmogorov's Ideas 50 Years On*, 434(1890):9–13, July 1991. Reprint of the translation of the article published in in Dokl. Akad. Nauk. SSSR 1941.

[42] T. Komarek. Private Communication, 2008.

[43] T. Komarek, L. Tay Wo Chong, M. Zellhuber, A. Huber, and W. Polifke. Modeling the effect of heat loss on flame stabilization in shear layers. In *Int. Conference om Jets Wakes ad Separated Flows, ICJWSF*, 2008.

[44] J. Kopitz. *Kombinierte Anwendung von Strömungssimulation, Netzwerkmodellierung und Regelungstechnik zur Vorhersage thermoakustischer Instabilitäten*. PhD thesis, Technische Universität München, Lehrstuhl für Thermodynamik, 2007.

[45] J. Kopitz, E. Bröcker, and W. Polifke. Characteristics-based filter for identification of planar acoustic waves in numerical simulation of turbulent compressible flow. 12th Int. Congress on Sound and Vibration, page 8, Lisbon, July 11-14 2005.

[46] J. Kopitz and W. Polifke. CFD-based application of the Nyquist criterion to thermo-acoustic instabilities. *J. Comp. Phys*, 227:6754–6778, 2008.

[47] K. Kostrzewa, B. Noll, M. Aigner, J. Lepers, W. Krebs, B. Prade, and M. Huth. Validation of advanced computational methods for determining flame transfer functions in gas turbine combustion systems. In *Pro-*

ceedings of GT 2007 ASME Turbo Expo 2007: Power for Land, Sea an Air. ASME, May 2007.

[48] K. Kostrzewa, A. Widenhorn, B. Noll, M. Aigner, W. Krebs, M. Huth, and P. Kaufmann. Impact of boundary conditions on the reconstructed flame transfer function for gas turbune combustion systems. In *Proceedings of ASME Turbo Expo 2008: Power for Land, Sea an Air GT 2008.* ASME, June 2008.

[49] U. Krüger, J. Hüren, S. Hoffmann, W. Krebs, P. Flohr, and D. Bohn. Prediction and measurement of thermoacoustic improvements in gas turbines with annular combustion systems. In *Proceedings of the ASME RURBO EXPO 2000.* ASME, May 2000.

[50] C. J. Lawn and W. Polifke. A model for the thermoacoustic response of a premixed swirl burner, Part II: The flame response. *Combust. Sci. and Tech.*, 176:1359–1390, 2004.

[51] R. Leandro. Private communication, 2009.

[52] T. Lieuwen and B. Zinn. Theoretical investigation of combustion instability mechanisms in lean premixed gas turbines. Number AIAA 98-0641 in 36th Aerospace Sciences Meeting and Exhibit, page 15, Reno, NV, January 12-15 1998. AIAA. vorhanden.

[53] K. Lundberg. Is there a better disproof of the barkhausen stability criterion? http://web.mit.edu/klund/www/weblatex/node4.html, 11 2002.

[54] K. McManus, T. Poinsot, and S. Candel. A review of active control of combustion instabilities. *Progress in Energy and Combustion Science*, 19(1):1–29, 1993.

[55] T. Melling. The acoustic impedance of perforates at medium and high sound pressure levels. *Journal of Sound and Vibration*, 29(1):1–65, 1973.

[56] L. Merz. *Grundkurs der Regelungstechnik.* R. Oldenbourg Verlag, München, Wien, 1981.

[57] K. Meyberg and P. Vachenauer. *Höhere Mathematik 2.* Springer-Verlag, 1999.

[58] G. Moore. Cramming more components onto integrated circuits. *Electronics Magazine*, 38(8), April 1965.

[59] F. Nicoud and F. Ducros. Subgrid-scale stress modelling based on the square of the velocity gradient tensor. *Flow, Turbulence and Combustion*, 1999.

[60] N. Noiray. *Analyse linéaire et non-linéaire des instabilités de combustion, application aux systèmes à injection multipoints et stratégies de contrôle.* PhD thesis, Ecole Centrale des Arts et Manufactures, 2008.

[61] N. Noiray, D. Durox, T. Schuller, and S. Candel. Passive control of combustion instabilities involving premixed flames anchored on perforated plates. In *Proceedings of the Combustion Institute 31*, page 1283–1290, 2007.

[62] N. Noiray, D. Durox, T. Schuller, and S. Candel. A novel strategy for passive control of combustion instabilities through modification of flame dynamics. In *Proceedings of ASMA Turbo Expo 2008: Power for Land, Sea and Air, GT2008, June 9-13, Berlin, Germany*, 2008.

[63] B. Noll. *Numerische Stömungsmechanik.* Springer Verlag, 1993.

[64] P. O'Rourke and F. Bracco. Two scaling transformations for the numerical computation of multidimensional unsteady laminar flames. *Journal of Computational Physics*, 33:185–203, 1979.

[65] Y. Özyörük and L. Long. A time-domain implementation of surface acoustic impedance condition with and without flow. *Journal of Computational Acoustics*, 5(3):277–296, 1997.

[66] C. Pankiewitz. *Hybrides Berechnungsverfahren für thermoakustische Instabilitäten von Mehrbrennersystemen.* PhD thesis, Technische Universität München, Lehrstuhl für Thermodynamik, 2004.

[67] C. O. Paschereit, B. Schuermans, W. Polifke, and O. Mattson. Measurement of transfer matrices and source terms of premixed flames. Number 99-GT-133 in Inrt. Gas Turbine & Aeroengine Congr. & Exh., Indianapolis, Indiana, 1999. ASME.

[68] J. Pieringer. *Simulation selbsterregter Verbrennungschwingungen in Raketenschubkammern im Zeitbereich.* PhD thesis, Technische Universität München, Lehrstuhl für Thermodynamik, 2008.

[69] J. Piquet. *Turbulent Flows.* Springer Verlag, 1999.

[70] T. Poinsot and S. Lele. Boundary conditions for direct simulation of compressible viscous flows. *Journal of Computational Physics,* 101:104–129, 1992.

[71] T. Poinsot, A. Trouve, D. Veynante, S. Candel, and E. Esposito. Vortex-driven acoustically coupled combustion instabilities. *Journal of Fluid Mechanics,* 177:265–292, 1987.

[72] T. Poinsot and D. Veynante. *Theoretical and Numerical Combustion.* Edwards, US, 2001.

[73] W. Polifke. *Combustion Instabilities.* Von Karman Institute. in: Advances in Aeroacoustics and Applications, Brussels, BE, 2004. Polif04b.

[74] W. Polifke. Entwicklung und Validierung eines hybriden Ansatzes zur Prüfung der thermo-akustischen Stabiltät von Verbrennungssystemen. Deutsche Forschungsgemeinschaft, Neuantrag, 2004.

[75] W. Polifke. Entwicklung und Validierung eines hybriden Ansatzes zur Prüfung der thermo-akustischen Stabiltät von Verbrennungssystemen. Deutsche Forschungsgemeinschaft, Fortsetzungsantrag, 2006.

[76] W. Polifke. Private Communication, 2008.

[77] W. Polifke. Abschlussbericht des Projektes Po/710-3: Entwicklung und Validierung eines hybriden Ansatzes zur Prüfung der thermo-akustischen Stabilität von Verbrennungssystemen. Technical report, Technische Universität München, Lehrstuhl für Thermodynamik, 2009.

[78] W. Polifke, C. O. Paschereit, and K. Döbbeling. Constructive and destructive interference of acoustic and entropy waves in a premixed combustor with a choked exit. *Int. J. of Acoustics and Vibration,* 6(3):1–38, 2001.

[79] W. Polifke, C. O. Paschereit, and T. Sattelmayer. A universally applicable stability criterion for complex thermo-acoustic systems, August 1997.

[80] W. Polifke, A. Poncet, C. O. Paschereit, and K. Döbbeling. Reconstruction of acoustic transfer matrices by instationary computational fluid dynamics. *Journal of Sound and Vibration*, 245(3):483–510, 2001.

[81] W. Polifke and C. Wall. Non-reflecting boundary conditions for acoustic transfer matrix estimation with LES. *C. Turb. Research, Annual Research Briefs*, pages 345–356, 2002.

[82] W. Polifke, C. Wall, and P. Moin. Partially reflecting and non-reflecting boundary conditions for simulation of compressible viscous flow. *Journal of Computational Physics*, 213:437–449, 2006.

[83] R. Prosser and J Schlüter. Towards improved boundary conditions for the DNS and LES of turbulent subsonic flows. In *Center for Turbulence Research, Proceedings of the Summer Programm 2004*, 2004.

[84] L. Råde and B. Westergren. *Mathematische Formeln.* Springer, 1997.

[85] 3. Baron Rayleigh. The explanation of certain acoustical phenomena. *Nature*, 18:319–321, 1878.

[86] L. Richardson. *Weather Prediction by Numerical Process.* Cambridge at the University Press, 1922.

[87] C. Richter, F. Thiele, L. Xiaodong, and M. Zhuang. Comparsion of time-domain impedance boundary conditions for lined duct flows. *AIAA Journal*, 45(6):1333–1345, 2007.

[88] P. Rijke. Notiz über eine neue Art, die in einer an beiden Enden offenen Röhre enthaltene Luft in Schwingungen zu versetzen. *Annalen der Physik*, 183:339–343, 1859.

[89] S. Roux, G. Lartigue, T. Poinsot, U. Meier, and C. Bérat. Studies of mean and unsteady flow in a swirled combustor using experiments, acoustic analysis and Large Eddy Simulations. *Combustion and Flame*, 141:40–54, 2005.

[90] D. Rudy and J. Strikwerda. A nonreflecting outflow boundary condition for subsonic Navier-Stokes calculations. *Journal of Computational Physics*, 36:55–70, 1980.

[91] P. Sagaut. *Large Eddy Simulation for Incompressible Flows.* Springer Verlag, 2001.

[92] M. Sanjosé, T. Lederlin, L. Gicquel, B. Cuenot, H. Pitsch, N. García-Rosa, R. Lecourt, and T. Poinsot. LES of two-phase reacting flows. In *Proceedings of the Summer Program 2008*, 2008.

[93] T. Sattelmayer and W. Polifke. Assessments of methods for the computation of the linear stability of combustors. *Combust. Sci. and Tech.*, 175:453 – 476, 2003.

[94] T. Sattelmayer and W. Polifke. A novel method for the computation of the linear stability of combustors. *Combust. Sci. and Tech.*, 175:477–497, 2003.

[95] T. Schoenfeld and M. Rudgyard. Steady and unsteady flows simulations using the hybrid flow solver AVBP. *AIAA Journal*, 37(11):1378–1385, 1999.

[96] B. Schuermans. Private communication, 2007.

[97] B. Schuermans, V. Bellucci, F. Guethe, F. Meili, P. Flohr, and C. O. Paschereit. A detailed analysis of thermoacoustic interaction mechanisms in a turbulent premixed flame. In *ASME Turbo Expo 2004, Vienna, Austria, June 14-17*, 2004.

[98] B. Schuermans, W. Polifke, and C. O. Paschereit. Modeling transfer matrices of premixed flames and comparison with experimental results. Number 99-GT-132 in Int. Gas Turbine & Aeroengine Congress & Exhibition, page 10, Indianapolis, Indiana, USA, 1999. ASME.

[99] L. Selle, G. Lartigue, T. Poinsot, R. Koch, K.-U. Schildmacher, W. Krebs, B. Prade, P. Kaufmann, and D. Veynante. Compressible Large-Eddy Simulation of turbulent combustion in complex geometry on unstructured meshes. *Combustion and Flame*, 137(4):489–505, 2004.

[100] J. Smagorinsky. General circulation experiments with the primitive equations. *Monthly Weather Review*, pages 99–164, March 1963.

[101] G. Staffelbach, L. Gicquel, G. Boudier, and T. Poinsot. Large Eddy Simulation of self excited azimuthal modes in annular combustors. *Proc. of the Combustion Institute, Pittsburgh - USA*, 32(In press), 2009.

[102] D. M. Sullivan. Frequency-dependent FDTD methods using z transforms. *IEEE Transactions on Antennas an Propagation*, 40(10):1223–1230, October 1992.

[103] L. Tay Wo Chong. Private communication, 2009.

[104] L. Tay Wo Chong, T. Komarek, M. Zellhuber, J. Lenz, C. Hirsch, and W. Polifke. Influence of strain and heat loss on the flame stabilization in a non-adiabatic combustor. In *Proceedings of the European Combustion Meeting 2009*, 2009.

[105] K. Thompson. Time dependent boundary conditions for hyperbolic systems. *Journal of Computational Physics*, 68 1:1–24, 1987.

[106] H. Tijdeman. On the progagation of sound waves in cylindrical tubes. *Journal of Sound and Vibration*, 39(1):1–33, 1975.

[107] S. Turns. *An Introduction to Combustion*. McGraw-Hill Higher Education, 2000.

[108] C. Wagner, T. Huttl, and P. Sagaut, editors. *Large Eddy Simulations for Acoustics*. Cambridge University Press, 2007.

[109] C. Wall. *Numerical Methods for Large Eddy Simulation of Acoustic Combustion Instabilities*. PhD thesis, Stanford University, 2005.

[110] E. Wanke. Private communication, 2009.

[111] J. Warnatz, U. Maas, and R.W. Dibble. *Verbrennung*. Springer, 2001.

[112] F. Williams. *Combustion Theory*. The Benjamin/Cummings Publishing Company, Inc., 1985.

[113] M. Zhu, A. Dowling, and K. Bray. Integration of CFD and low-order models for combustion oscillations in aeroengines. ISABE-2001-1088, page 12, 2001.

[114] M. Zhu, A. P. Dowling, and K. N. C. Bray. Self-excited oscillations in combustors with spray atomiser. Number 2000-GT-108 in Proc. ASME Turbo Expo 2000, page 10, Munich, Germany, May 8-11 2000. ASME.

8 Appendices

8.1 Appendix A: BRS LES Mean Results

The highly instationary nature of LES requires a large amount of time steps to compare simulation and experiment. Experimental results have been obtained in terms of mean flow and mean reaction fields. In order to compare simulation and experiment in a meaningful way, a mean solution over 200,000 iterations has been calculated. The averaged flow field of this is well enough converged to permit a comparison.

8.1.1 Flow Field

Experimental data of the flow field of the burner has been provided by my colleague Thomas Komarek. This data includes Particle Induced Velocimetry (PIV) measurements of the hot burner. A mean flow field of 1000 PIV data sets and the mean LES flow field are compared in figure 8.1 for $P = 70\,\mathrm{kW}$ and $\lambda = 1.3$, figure 8.2 for $P = 50\,\mathrm{kW}$ and $\lambda = 1.3$ and figure 8.3 for $P = 70\,\mathrm{kW}$ and $\lambda = 1.1$.

In general, the flow field is well reproduced in the LES. It can be seen from these figures that the main difference is a shorter and stronger center recirculation zone in the LES case. The velocity profiles for axial distances of 30, 50, 70 and 90 mm from the burner mouth are shown in figure 8.4 for $P = 70\,\mathrm{kW}$, $\lambda = 1.3$, in figure 8.5 for $P = 50\,\mathrm{kW}$, $\lambda = 1.3$ and in figure 8.6 for $P = 70\,\mathrm{kW}$, $\lambda = 1.7$. Here, a good agreement of the location and amplitude of the maximum axial velocity is visible, while, as mentioned before, the recirculation zone is stronger and shorter in the LES case. The differences between LES and experiment are within the range that other authors have experienced with

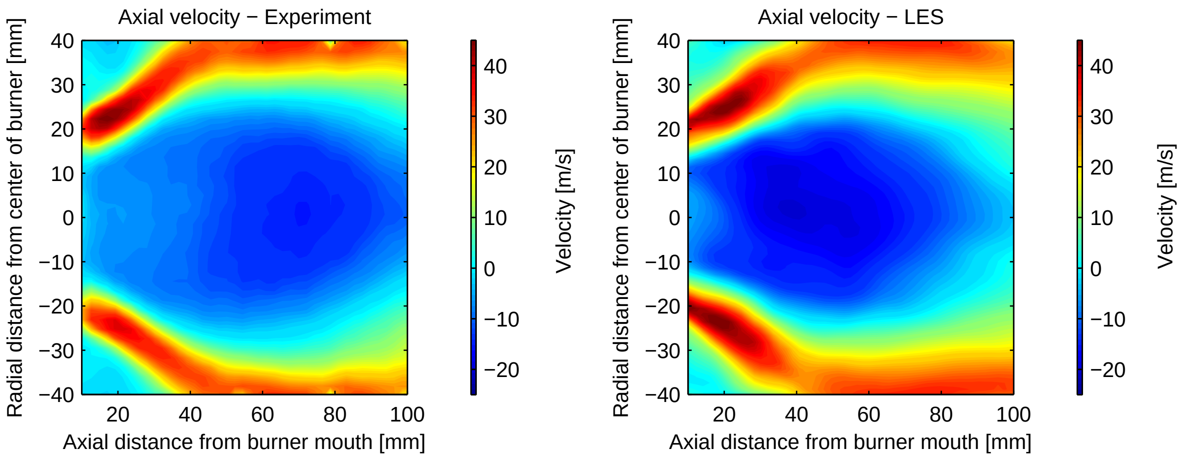

Figure 8.1: Mean axial flow field of the experiment (left) and the LES (right) using the same color scale for the axial velocity. The flow field is taken from a center plane, $P = 70\,\text{kW}$, $\lambda = 1.3$.

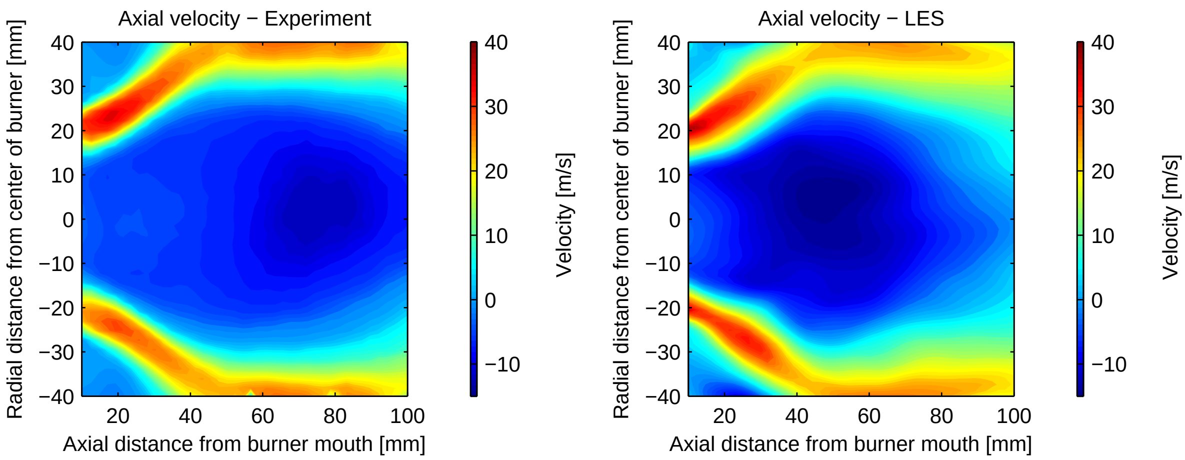

Figure 8.2: Mean axial flow field of the experiment (left) and the LES (right) using the same color scale for the axial velocity. The flow field is taken from a center plane, $P = 50\,\text{kW}$, $\lambda = 1.3$.

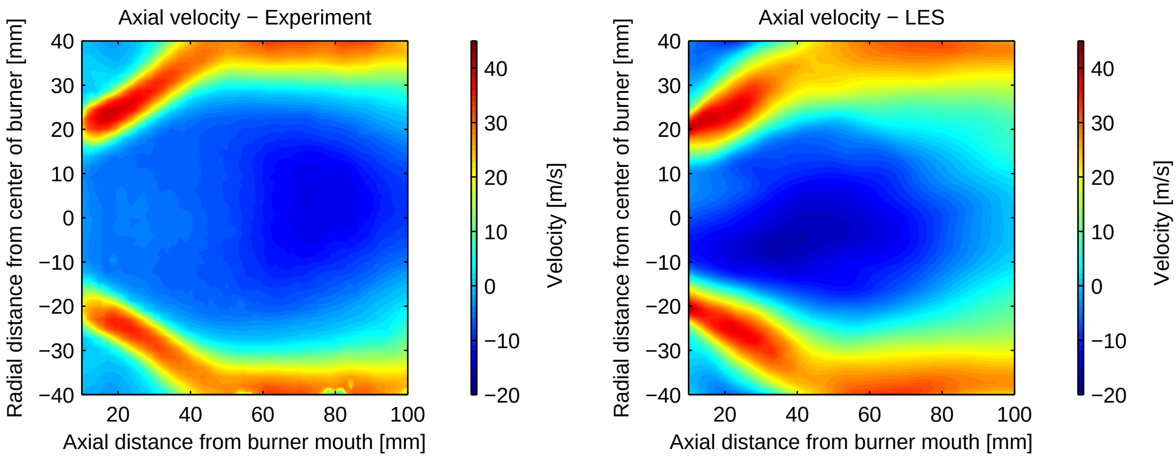

Figure 8.3: Mean axial flow field of the experiment (left) and the LES (right) using the same color scale for the axial velocity. The flow field is taken from a center plane, $P = 70\,\text{kW}$, $\lambda = 1.1$.

AVBP [89, 92, 99].

8.1.2 Reaction Zone

In contrast to flow data, reaction rates and zones are difficult to obtain from experiments. For the BRS burner OH* chemiluminescence has been used in the experiments. In the numerical simulation, the heat release rate can be directly determined. In contrast to PIV measurements, where particles are tracked in a light sheet, chemiluminescence methods yield data, which is integrated over the depth along the line of sight. In order to permit a valid comparison between experiment and simulation, the data from the simulation has been integrated over the depth of the domain [43, 104]. Figures 8.7 and 8.8 show the reaction zones for experiment and LES. Since the values are of different origin, no color scale is given, the color varies linearly between 0 and the maximum value. The general shape of the flame proves to be well reproduced. The cold walls in the combustion chamber in combination with the thickened flame combustion model indeed prevent the outer shear layer from burning. Only little heat release can be observed there. Especially in the RANS context, combustion models often fail in reproducing this correctly [43, 104]. Differences between experiment and LES can be observed in the center part, where the

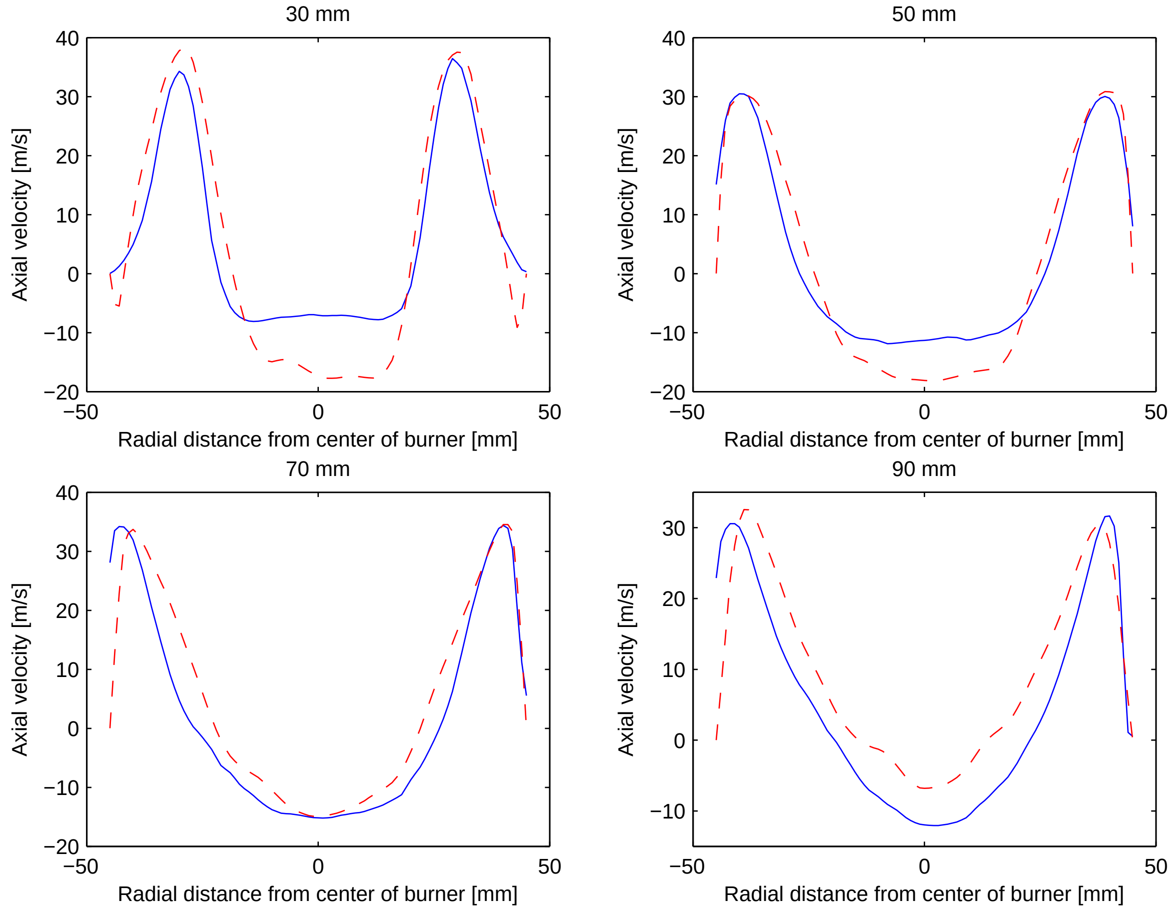

Figure 8.4: Radial flow field profile at an axial distance of 30, 50 (top left and right), 70 and 90 mm (bottom left and right) from the burner mouth. LES (red, dashed) and experimental (blue, solid) data for the flow field taken from a center plane, $P = 70\,\text{kW}$, $\lambda = 1.3$.

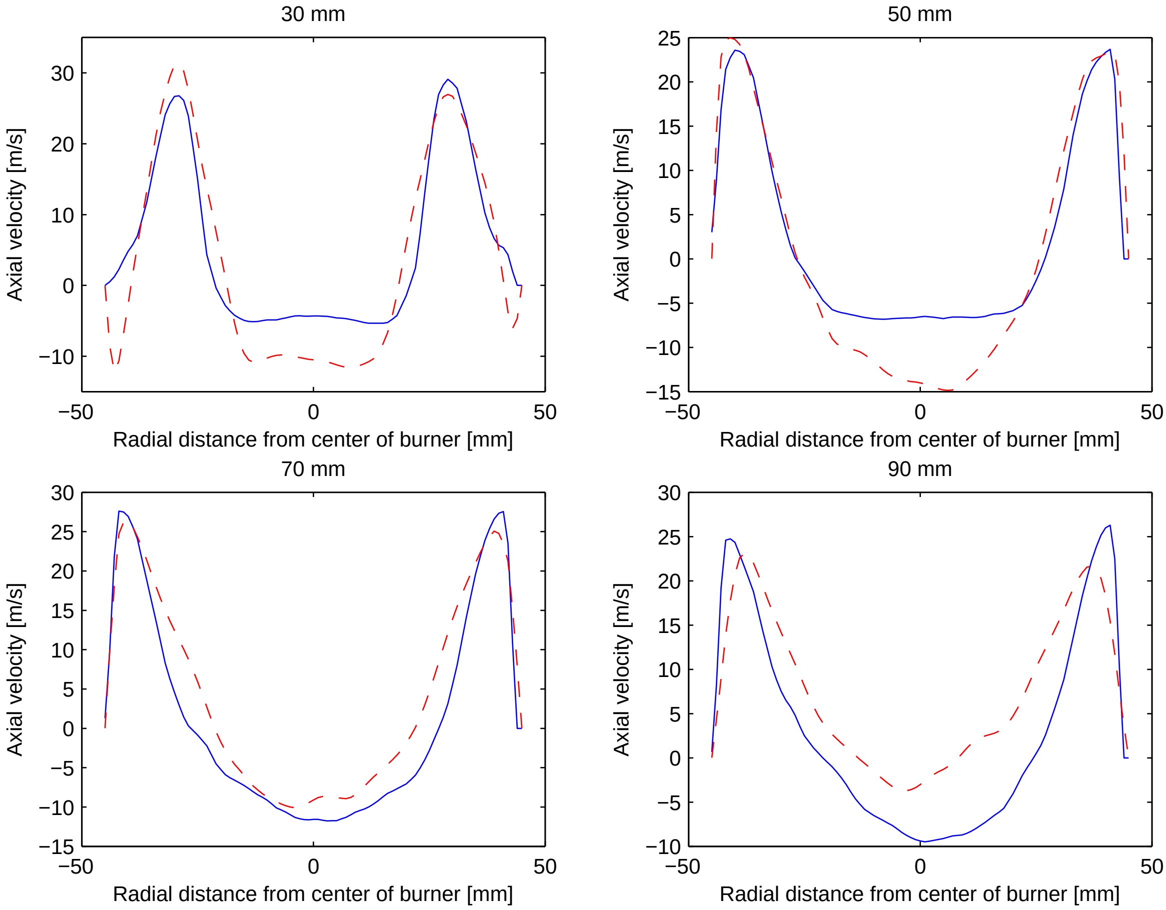

Figure 8.5: Radial flow field profile at an axial distance of 30, 50 (top left and right), 70 and 90 mm (bottom left and right) from the burner mouth. LES (red, dashed) and experimental (blue, solid) data for the flow field taken from a center plane, $P = 50\,\mathrm{kW}$, $\lambda = 1.3$.

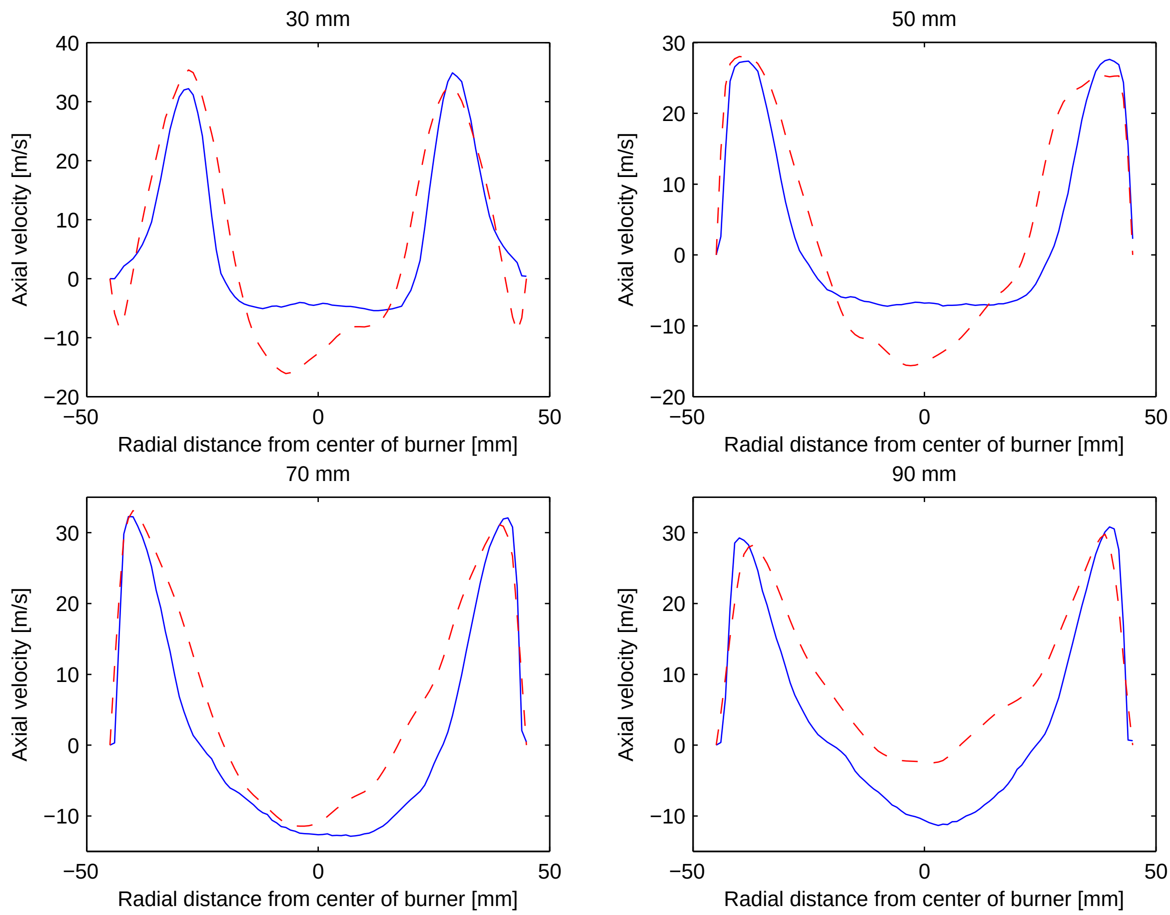

Figure 8.6: Radial flow field profile at an axial distance of 30, 50 (top left and right), 70 and 90 mm (bottom left and right) from the burner mouth. LES (red, dashed) and experimental (blue, solid) data for the flow field taken from a center plane, $P = 70\,\mathrm{kW}$, $\lambda = 1.1$.

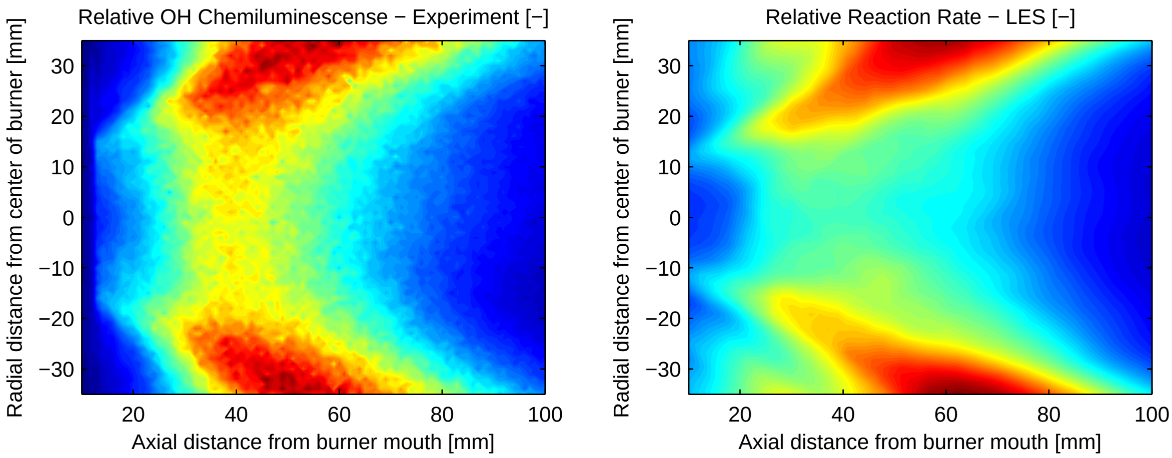

Figure 8.7: Mean reaction zone of the experiment (left) and the LES (right). OH* chemiluminescence is used for the experiment, the LES results shows the heat release rate. Color map is identical for both images. $P = 70\,\text{kW}$, $\lambda = 1.3$.

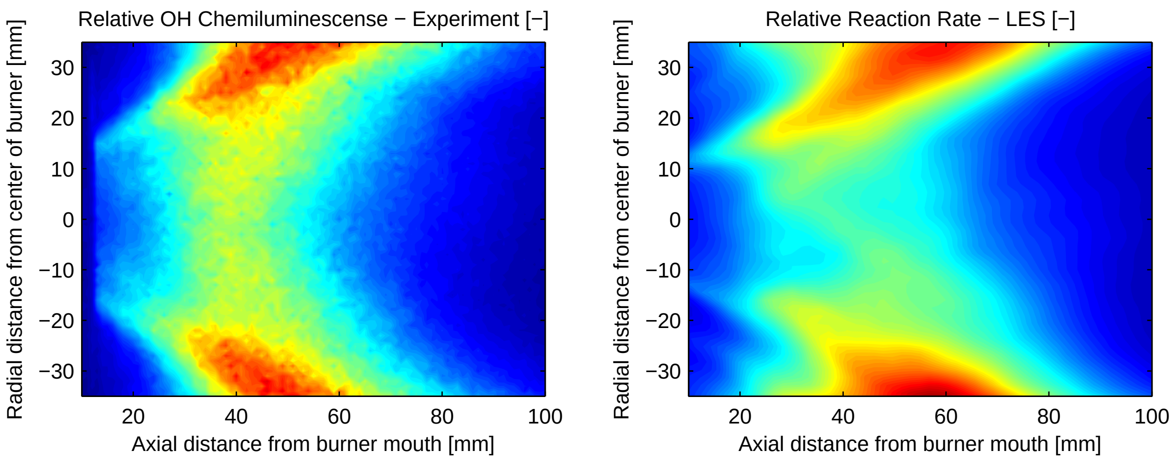

Figure 8.8: Mean reaction zone of the experiment (left) and the LES (right). OH* chemiluminescence is used for the experiment, the LES results shows the heat release rate. Color map is identical for both images. $P = 50\,\text{kW}$, $\lambda = 1.3$.

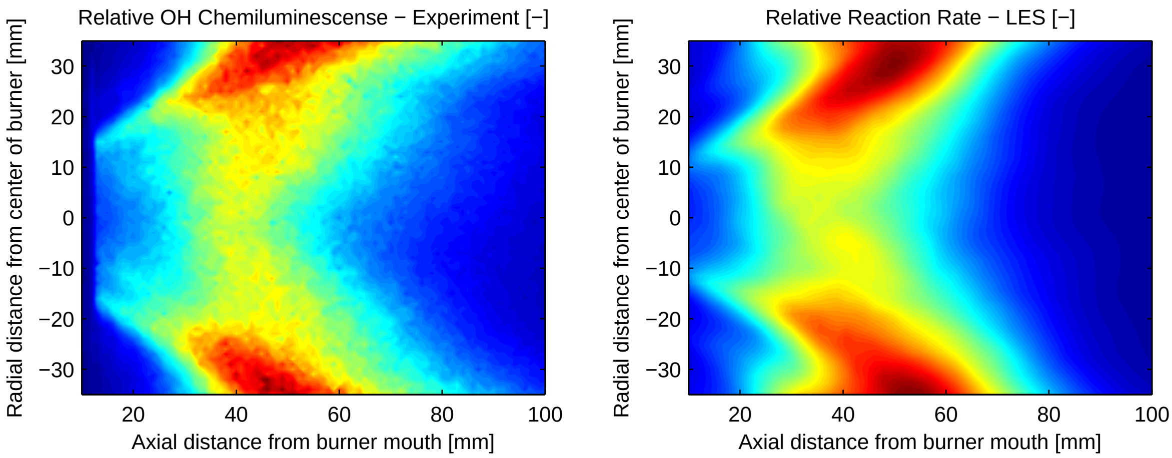

Figure 8.9: Mean reaction zone of the experiment (left) and the LES (right). OH* chemiluminescence is used for the experiment, the LES results shows the heat release rate. Color map is identical for both images. $P = 70\,\mathrm{kW}$, $\lambda = 1.1$.

LES shows less activity, and close to the walls, where the LES reaction zone thickens up slightly and also shows a slight offset to downstream. The less pronounced reaction in the center part may cause longer flames. This would increase the acceleration of the gas towards the center line in the downstream part and, hence, be reason for the stronger recirculation zone. The stronger reaction at the sides may also be responsible for the slightly broader velocity peaks of the LES in figures 8.4 , 8.5 and 8.6. The thickened reaction zone may be due to the combustion model. The axial distribution of the heat release for both experiment and LES can be seen in figures 8.10, 8.11 and 8.12. The results prove that the axial distribution of the reaction zone is well reproduced and the peak of the chemical activity is at the right position in the LES. This is essential for a correct time delay in the acoustic response.

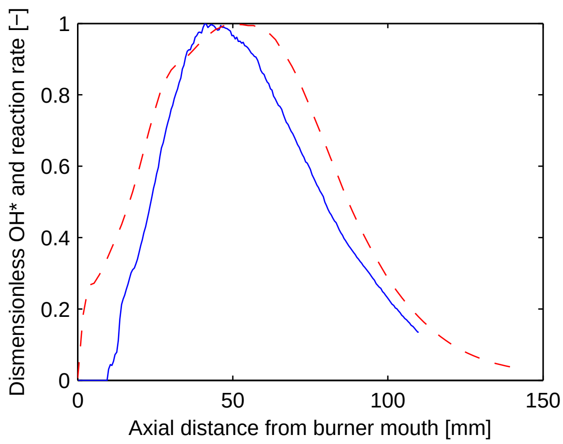

Figure 8.10: Axial distribution of the heat release zone, normalized by maximum value. Heat release for LES (red, dashed) and OH* chemiluminescence for the experiment (blue, solid). $P = 70\,\mathrm{kW}$, $\lambda = 1.3$.

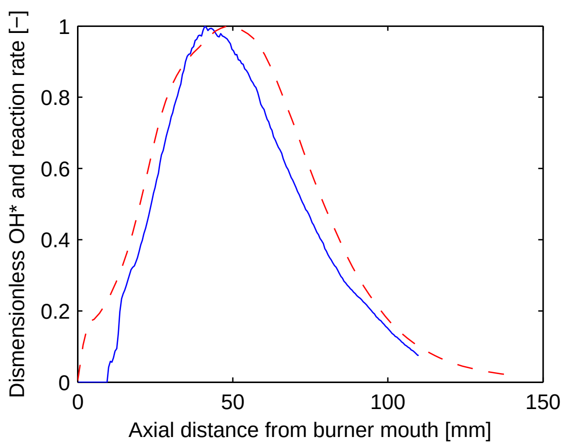

Figure 8.11: Axial distribution of the heat release zone, normalized by maximum value. Heat release for LES (red, dashed) and OH* chemiluminescence for the experiment (blue, solid). $P = 50\,\mathrm{kW}$, $\lambda = 1.3$.

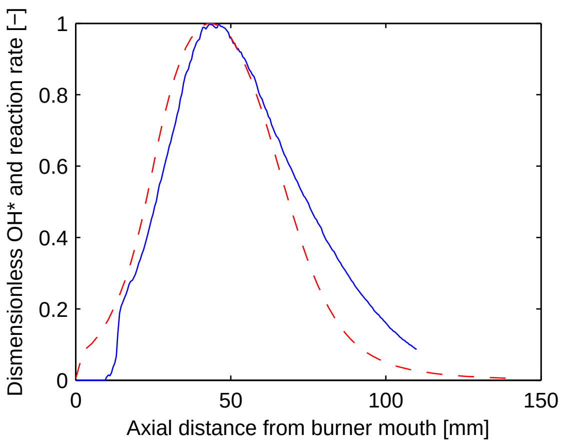

Figure 8.12: Axial distribution of the heat release zone, normalized by maximum value. Heat release for LES (red, dashed) and OH* chemiluminescence for the experiment (blue, solid). $P = 70\,\mathrm{kW}$, $\lambda = 1.1$.

8.2 Appendix B: BRS LES Input Files

8.2.1 run.dat

```
'../MESH/mesh_sec_out'                  ! Mesh file
'../MESH/mesh_sec_out.asciiBound'       ! Ascii Boundary file
'../MESH/mesh_sec_out.asciiBound_tpf'   ! Ascii_tpf Boundary file
'../MESH/mesh_sec_out.solutBound'       ! Boundary solution file
'./SOLUT_TIME/BRS_full_unstr_50_13_5spec_av_0100000.h5'
'./SOLUT_TIME/BRS_full_unstr_50_13_5spec_av'
'./TEMP_TIME/'                  ! temporal evolution directory

1.0        ! Reference length  | scales coordinates X by X/reflen

100000   ! Number of iterations

100        ! Number of elements per group (typically of order 100)
1          ! Preprocessor: skip (0), use (1) & write (2) & stop (3)

1          ! Interactive details of convergence (1) or not (0)
10         ! Prints convergence every x iterations
1          ! Stores solution in separate files (1) or not (0)
10000    ! Stores solution every x iterations

1          ! Euler (0) or Navier-Stokes (1) calculation
0          ! Store additional info (1) All (2) Sensors or (0) not
3          ! Chemistry
2          ! LES
0          ! TPF
31         ! Artificial viscosity
2          ! Steady state (0) or unsteady (1) calculation
1.5e-7
1 0 0 0 0 ! Scheme specification
1          ! Number of Runge-Kutta stages
```

```
1.0d0 1.0d0 1.0d0      ! Runge-Kutta coefficients
0.7d0       ! CFL parameter for complete update
0.05d0      ! 4th order artificial viscosity coeff.
0.1d0       ! 2nd order artificial viscosity coeff.
0.10d0      ! Fr viscous time-step
```

8.2.2 .asciiBound

Syntax for the TDIBC-patches (1-5 here):

- parameters 1-1 as usual
- Identifier number (<1) links patch to bndy_param.dat and plane definition
- flag for reference value averaging:
  - 0: moving average as defined in record_planes.dat and cut-planes.choices
  - 1: used fixed pressure as reference, defined in paramter line 10
  - 2: used fixed velocity as reference, defined in paramter line 11
  - 3: used fixed pressure and velocity as reference, defined in paramter lines 10 and 11
- lines 6-9 as 4-7 (for inlet, for outlet only one line) in usual Boundary Conditions
- reference pressure
- reference velocity

```
  Grid processing by hip version 1.16.5 'Hirondelle'.
  9 boundary patches.
---------------------------------------------
  Patch: 1
  outlet_block
  INLET_RELAX_WAVEID
  1
  1
  1
  -6
  0
```

```
  100000
  100000
  100000
  100000
  101300
  0
---------------------------------------------
  Patch: 2
  outlet-x-y
  OUTLET_RELAX_WAVEID
  1
  1
  1
  -2
  0
  30000
  101300
  0
---------------------------------------------
  Patch: 3
  outlet+x-y
  OUTLET_RELAX_WAVEID
  1
  1
  1
  -3
  0
  30000
  101300
  0
---------------------------------------------
  Patch: 4
  outlet+x+y
  OUTLET_RELAX_WAVEID
```

```
  1
  1
  1
  -4
  0
  30000
  101300
  0
---------------------------------------------
  Patch: 5
  outlet-x+y
  OUTLET_RELAX_WAVEID
  1
  1
  1
  -5
  0
  30000
  101300
  0
---------------------------------------------
  Patch: 6
  velocity-inlet-11
  INLET_RELAX_RHOUVW_T_Y
  1
  1
  1
  88000
  88000
  88000
  88000
---------------------------------------------
  Patch: 7
  wall_chamber
```

```
  WALL_NOSLIP_ISOT
  1
---------------------------------------------
  Patch: 8
  wall_lance
  WALL_NOSLIP_ISOT
  1
---------------------------------------------
  Patch: 9
  wall_rest
  WALL_NOSLIP_ADIAB
```

	$\lambda = 1.3$	$\lambda = 1.1$
s_l	2.723651E-01	3.513237E-01
δ_0	5.391695E-04	4.616703E-04

Table 8.1: Parameters for the combustion model

8.2.3 input_chem.dat

```
5.0d0                  ! fthick -  flamme thickening

0                      ! No clipping (0), clipping (1)
1.0d-3                 ! Stability criterion for chemical reactions

2.723651E-01                ! sl - laminar flame speed
5.391695E-04               ! delta0 - laminar flame thickness
0.0095d0                 ! constant of the efficiency function
10.0d-3                 ! Integral length scale

1.013d5                  ! Reference pressure for reaction rate
0.5d0                  ! Coefficient for activation temperature
293.d0                 ! Cold gas temperature for omega0
1.960737E+03                 ! Hot gas temperature
4.0                    ! mass stoechiometric ratio
2.69d-06               ! omega0
1                      ! reference reaction for the dynamic thickening
```

s_l and δ_0 for different air ratios are given in table 8.1.

8.2.4 bndy_param.dat

The bndy_param.dat is the control file for the time domain impedance boundary condition (TDIBC), This bndy_param.dat does not include excitation, this would not be printable, since it includes several million numbers. Syntax:

- First line: Numer of TDIBCs
- a block of seven lines for each TDIBC
  - Identifier Nymber (< 0) links the TDIBC to the patch in the .asciiBound
  - number m of items in line 5 of the block
  - number n of items in line 6 of the block
  - number o of items in line 7 of the block
  - coefficients b_1 b_2 ... b_m for TDIBC
  - coefficients a_0 a_1 ... a_{n-1} for TDIBC
  - signal s_1 s_2 ... s_{o-1} imposed as excitation (m/s at inlet, Pa at outlet)

```
5
-6
2
2
2
0.0 0.0
0.0 0.0
0.0 0.0
-2
2
2
2
0.0 0.0
0.0 0.0
0.0 0.0
```

```
-3
2
2
2
0.0 0.0
0.0 0.0
0.0 0.0
-4
2
2
2
0.0 0.0
0.0 0.0
0.0 0.0
-5
2
2
2
0.0 0.0
0.0 0.0
0.0 0.0
```

8.2.5 cutplanes.choices

This file controls the tool (cutplanes) which performes the calculation of the monitor planes and generates the file record_planes.dat, which is needed by AVBP

```
'./mesh_sec_out.coor'           ! Coor file
'./mesh_sec_out.conn'           ! Conn file
-0.1                         ! Averaging time
17                           ! Number of monitor planes
-1                          ! Identifier of 1st plane
0.0 0.0 -0.3494                ! Point for distance calculation
```

```
0.0 0.0 -0.3493                 ! Point for plane definition for 1st plane
0.0 0.0 -1.0                  ! normal for plane definition for 1st plane
0 0                          ! additional limits code (0 0: entire plane)
-2                           ! Identifier of 2nd plane
0.0 0.0 0.2                 ! Point for distance calculation for 2nd plane
0.0 0.0 0.195                 ! Point for plane definition for 2nd plane
0.0 0.0 1.0                  ! normal for plane definition for 2nd plane
2 4                          ! restriction to a 2=polygon with 4=4 vertices
0.0 0.0 0.0                  ! 1st vertex (counter clockwise)
-0.05 0.0 0.0                ! 2nd vertex (counter clockwise)
-0.05 -0.05 0.0              ! 3rd vertex (counter clockwise)
0.0 -0.05 0.0                ! 4th vertex (counter clockwise)
-2                           ! Identifier of 3rd plane
0.0 0.0 0.2                 ! Point for distance calculation for 3rd plane
0.0 0.0 0.185
0.0 0.0 1.0
2 4
0.0 0.0 0.0
-0.05 0.0 0.0
-0.05 -0.05 0.0
0.0 -0.05 0.0
-2                           ! Identifier of 4th plane
0.0 0.0 0.2
0.0 0.0 0.175
0.0 0.0 1.0
2 4
0.0 0.0 0.0
-0.05 0.0 0.0
-0.05 -0.05 0.0
0.0 -0.05 0.0
-3                           ! Identifier of 5th plane
0.0 0.0 0.2
0.0 0.0 0.195
0.0 0.0 1.0
```

```
2 4
0.0 0.0 0.0
0.0 -0.05 0.0
0.05 -0.05 0.0
0.05 0.0 0.0
-3                        ! Identifier of 6th plane
0.0 0.0 0.2
0.0 0.0 0.185
0.0 0.0 1.0
2 4
0.0 0.0 0.0
0.0 -0.05 0.0
0.05 -0.05 0.0
0.05 0.0 0.0
-3                        ! Identifier of 7th plane
0.0 0.0 0.2
0.0 0.0 0.175
0.0 0.0 1.0
2 4
0.0 0.0 0.0
0.0 -0.05 0.0
0.05 -0.05 0.0
0.05 0.0 0.0
-4                        ! Identifier of 8th plane
0.0 0.0 0.2
0.0 0.0 0.195
0.0 0.0 1.0
2 4
0.0 0.0 0.0
0.05 0.0 0.0
0.05 0.05 0.0
0.0 0.05 0.0
-4                        ! Identifier of 9th plane
0.0 0.0 0.2
```

```
0.0 0.0 0.185
0.0 0.0 1.0
2 4
0.0 0.0 0.0
0.05 0.0 0.0
0.05 0.05 0.0
0.0 0.05 0.0
-4                        ! Identifier of 10th plane
0.0 0.0 0.2
0.0 0.0 0.175
0.0 0.0 1.0
2 4
0.0 0.0 0.0
0.05 0.0 0.0
0.05 0.05 0.0
0.0 0.05 0.0
-5                        ! Identifier of 11th plane
0.0 0.0 0.2
0.0 0.0 0.195
0.0 0.0 1.0
2 4
0.0 0.0 0.0
0.0 0.05 0.0
-0.05 0.05 0.0
-0.05 0.0 0.0
-5                        ! Identifier of 12th plane
0.0 0.0 0.2
0.0 0.0 0.185
0.0 0.0 1.0
2 4
0.0 0.0 0.0
0.0 0.05 0.0
-0.05 0.05 0.0
-0.05 0.0 0.0
```

```
-5                        ! Identifier of 13th plane
0.0 0.0 0.2
0.0 0.0 0.175
0.0 0.0 1.0
2 4
0.0 0.0 0.0
0.0 0.05 0.0
-0.05 0.05 0.0
-0.05 0.0 0.0
-6                        ! Identifier of 14th plane
0.0 0.0 0.2
0.0 0.0 0.195
0.0 0.0 1.0
0 0
-6                        ! Identifier of 15th plane
0.0 0.0 0.2
0.0 0.0 0.185
0.0 0.0 1.0
0 0
-6                        ! Identifier of 16th plane
0.0 0.0 0.2
0.0 0.0 0.175
0.0 0.0 1.0
0 0
-10                       ! Identifier of 17th plane
0.0 0.0 0.0
0.0 0.0 -0.01
0.0 0.0 1.0
0 0
```